

Track reconstruction for InGrid Chips for a Time Projection Chamber

DISSERTATION

*zur Erlangung des Grades eines Doktors
der Naturwissenschaften*

vorgelegt von

M.Sc. Amir Noori Shirazi

eingereicht bei der Naturwissenschaftlich-Technischen Fakultät
der Universität Siegen
Siegen 2018

Referent Koreferent	Prof. Dr. rer. nat. Ivor Fleck Univ.-Doz. Di Dr. Rudolf Frühwirth	Universität Siegen Institut Für Hochenergi- physik (HEPHY)
Weitere Prüfer Prüfer Prüfer	Prof. Dr. rer. nat. Klaus Desch Prof. Dr. rer. nat. Thomas Mannel	Universität Bonn Universität Siegen
Datum der Dis- putation:	09. Juli 2018	

Gedruckt auf alterungsbeständigem holz- und säurefreiem Papier.

Abstract

The International Linear Collider (ILC) is one of the best candidates for the future of the high energy physics to explore many unknown phenomena such as dark matter and the physics beyond the Standard Model. The ILC has two detectors. The International Large Detector (ILD) is one of these detectors and a Time Projection Chamber (TPC) is a tracker detector foreseen for the ILD. The main goal of the TPC is to measure the momentum of tracks and the energy loss of charged particles in order to reach high precision physics observables. Many different technologies are considered for this purpose.

GridPix, i.e. a combination of a micropattern gaseous detector and pixelized readout, one of the candidate readouts for the ILD TPC, is under investigation in this thesis. The result of this combination is that there are many hits along a track causing a better spatial resolution compared with other readout systems. This property is essential to measure the momentum more precisely. In addition, the huge amount of the hits along a track improves the energy loss measurement. However, the pattern recognition (track finding) for the GridPix is very challenging due to a large number of hits and diffusion effects in the TPC in addition to the noise in the readout system.

A novel algorithm for the track finding has been developed to solve this difficulty. This algorithm first tries to find a segment of a track in a small area, called tracklet, based on the Hough Transform and using a bivariate normal distribution to improve collecting relevant hits of a tracklet. After finding all tracklets in all regions, the relevant tracklets are merged in order to have the full track. A successful performance of this algorithm for both simulated and experimental data shows that it is promising for the future.

Zusammenfassung

Der International Linear Collider (ILC) ist einer der besten Kandidaten für die Zukunft der Hochenergiephysik, um viele unbekannte Phänomene wie Dunkle Materie und die Physik jenseits des Standardmodells zu erforschen. Der ILC hat zwei Detektoren. Der International Large Detector (ILD) ist einer dieser Detektoren, für den eine Time Projection Chamber (TPC) als Spurdetektor vorgesehen ist. Das Hauptziel einer TPC ist es, gleichzeitig den Impuls und den Energieverlust geladener Teilchen anhand ihrer Spuren zu messen, um hochpräzise physikalische Observablen zu erhalten. Zu diesem Zweck werden viele verschiedene Technologien in Betracht gezogen.

GridPix, d.h. die Kombination eines Mikrostruktur-Gasdetektors und eines Pixel-Auslesesystems, ist ein Kandidat für die Auslesetechnologie der TPC und wird in dieser Arbeit untersucht. Das Ergebnis dieser Kombination ist, dass es viele Treffer entlang einer Spur gibt, die zusammen eine bessere räumliche Auflösung im Vergleich zu anderen Auslesesystemen bewirken. Diese Eigenschaft ist für eine präzisere Messung des Impulses wesentlich. Darüber hinaus verbessert die große Anzahl an Treffern entlang einer Spur die Messung des Energieverlusts. Die Mustererkennung (Spurbestimmung) für GridPix ist allerdings sehr schwierig aufgrund der großen Zahl an Treffern und Diffusionseffekten in der TPC zusätzlich zum elektronischen Rauschen im Auslesesystem.

Es wurde ein neuer Algorithmus zur Spurbestimmung entwickelt, um diese Schwierigkeiten aufzulösen. Der Algorithmus versucht zuerst, auf der Grundlage der Hough-Transformation ein Spursegment (Tracklet) zu finden, wobei zur besseren Identifikation für das Tracklet relevanter Treffer eine bivariate Normalverteilung verwendet wird. Nachdem alle Tracklets in allen Regionen gefunden wurden, werden die relevanten Tracklets zur vollständigen Spur zusammengefügt. Die erfolgreiche Anwendung dieses Algorithmus sowohl auf simulierte als auch auf experimentelle Daten zeigt, dass er für die Zukunft vielversprechend ist.

Acknowledgements

Firstly, I would like to express my sincere gratitude to my supervisor Prof. Dr. Ivor Fleck for all his support. When I started my Ph.D. I had little practical experience with detectors. But he trusted and supported me to learn and led me to success. Even I remember that he received an email from our colleagues offering him to change my topic, which was the dead-end for me in my project on that time, but he again trusted and let me continue and fortunately I was successful. I always think about that at that time he could do that or asked me to finish my thesis soon while he supported me until the end. I am proud that I was his student and happy that I did my Ph.D. with him.

Besides my supervisor, I would like to have a special gratitude to two great gentlemen whom I have met in my career life: Dr. Claus Kleinwort and Univ.-Doz. Di Dr. Rudolf Frühwirth. During my thesis, times to times Dr. Claus Kleinwort supported me very kindly and of course, without his help, I could not finish my code successfully. He thought me many things that were essential for my thesis. In addition, I had this great chance to meet Univ.-Doz. Di Dr. Rudolf Frühwirth at Institute of High Energy Physics (HEPHY), Vienna and I learned the basics of the pattern recognition from him. It was one of the wonderful experiences that I had during my Ph.D.

Furthermore, I would like to thank my Ph.D. committee members, Prof. Dr. Ivor Fleck, Prof. Dr. Klaus Desch, Univ.-Doz. Di Dr. Rudolf Frühwirth and Prof. Dr. Thomas Mannel for their time and their attention to my thesis.

In addition, I had this chance to work with many great people and I am thankful for all their help. Prof. Dr. Klaus Desch, Dr. Jochen Kaminski, Dr. Michael Lupberger from the University of Bonn, Dr. Qader Dorosti, Dr. Marcus Niechciol from the University of Siegen and Oliver Schäfer from DESY were those people that supported me during my thesis.

Moreover, I would like to be thankful to my friends and colleagues for their help and suggestions: Dr. Jan Timmermans, Dr. Peter Kluit, Dr. Ulrich Werthenbach, Dr. Hendrik Czirr, Sebastian Sonntag, Dr. Uwe Fröhlich, Sara Ghasemi, Dr. Bakul Gaur, Christian Dehn, Farnoush Shahriaran and my colleagues at DESY group.

At the end, I would like to express my profound gratitudes to my family. They always encouraged me and they were my only reason for working hard and for beating the odds, especially during the difficult times which I faced with in the past few years. I dedicate this thesis to them.

Contents

Acknowledgements	v
1 Introduction	1
2 Foundation	3
2.1 The Standard Model	3
2.2 The International Linear Collider	4
2.3 Physics at the ILC	5
2.3.1 Higgs physics	6
2.3.2 Top physics	7
2.4 The International Large Detector	8
2.5 The Time Projection Chamber	8
2.5.1 Interaction of charged particles with matter	10
2.5.2 Ionization yield	13
2.5.3 Drift and Diffusion	14
2.5.4 Gas amplification	17
Gas Electron Multipliers	17
Micromegas	17
2.5.5 Momentum resolution	18
2.6 Software framework	21
2.6.1 LCIO	21
2.6.2 GEAR	22
2.6.3 MarlinTPC	22
2.7 The Timepix chip	23
2.8 The InGrid chip	25
3 Track reconstruction	27
3.1 Introduction	27
3.2 Track finding (Pattern recognition)	27
3.3 Track fitting	29
3.4 Analysis	31
3.4.1 Hit matching	31
3.4.2 Parameter matching	32
4 Track finding for InGrid chips	35
4.1 Introduction	35
4.2 Hough Transform	35
4.3 Bivariate normal distribution (BND)	39
4.3.1 Covariance matrix in the X-Y plane	42
4.3.2 Covariance matrix in the S-Z plane	42
4.4 Ellipse equation and semi-major and semi-minor axes	43
4.5 Tracklet Parameters	46
4.5.1 The X-Y plane parameters	46

4.5.2	The S-Z plane parameters	48
4.6	The merging process	52
4.7	Recollection inliers	56
4.8	Processors in MarlinTPC	58
5	Simulation and optimization	61
5.1	Introduction	61
5.2	Simulation chain in MarlinTPC	61
5.3	Optimization of InGridBNDHoughTransformProcessor	63
5.3.1	Optimization in the X-Y plane	64
5.3.2	Optimization in the S-Z plane	76
6	Test beam experiment with 160 InGrid chips	87
6.1	Test beam 2015	87
6.1.1	The large prototype TPC (LP TPC) at DESY	87
6.1.2	Module arrangement	89
6.1.3	Conditions and run parameters	89
6.1.4	Pipeline of data analysis	92
6.1.5	Data analysis	99
	Momentum resolution	99
	Transverse and longitudinal spatial resolution	103
7	Summary	113
A	Covariance matrix for Karimäki fit	117
B	The plots for the optimization	119
C	Examples of the track reconstruction	123
	Bibliography	129

List of Figures

2.1	The standard Model and the elementary particles	3
2.2	Schematic of the International Linear Collider	5
2.3	Feynman diagram of Higgs-strahlung process	6
2.4	Simulation of the Higgs recoil mass based on the momentum of $\mu^+\mu^-$ production	7
2.5	Schematic of the International Large Detector	9
2.6	Schematic of a TPC	10
2.7	The energy deposition of a muon as a function of $\beta\gamma$	12
2.8	The spectrum of the energy loss against the momentum in the ALICE TPC	13
2.9	Simulation and measurement results of the transverse diffusion and the drift velocity against the electric field measured in T2K gas	16
2.10	Scanning Electron Microscope (SEM) image of a GEM	18
2.11	The sagitta of a circle with radius r and the arc length L	19
2.12	Parameters of a helix	22
2.13	Schematic of the principle of how the Marlin works	23
2.14	Diagram of a pixel for Timepix chip	24
2.15	Different modes of the operating Timepix chip	24
2.16	Schematic illustration of using InGrid technology in a detector	25
2.17	96 InGrid chips arranged on 12 Octoboards	26
4.1	Bubble Chamber and Hough transform	36
4.2	Hough transform based on a straight line	36
4.3	Hough transform based on a Hesse normal form	37
4.4	The pca point in the X-Y plane	38
4.5	Bivariate normal distribution	40
4.6	Iso-countor of the bivariate normal distribution fit	41
4.7	The rotated ellipse	44
4.8	The ellipse corresponding to $1/e$ of the peak of BND fit	46
4.9	The arc length, a hit position, and the pca position	49
4.10	The general flowchart of the track finding for an Octoboard.	51
4.11	The merging process of tracklets	53
4.12	Examples of the χ^2/ndf distribution	56
4.13	A missed tracklet after the finding and fitting processes	57
4.14	The track after recollection inliers	58
5.1	The chain of all processors used for simulation of InGrid	62
5.2	Two tracks simulation for the X-Y plane optimization	65
5.3	Track efficiency and purity for two tracks with 2 mm distance in the Y direction and 30 mm drift length	66
5.4	Track efficiency and purity for two tracks with 2 mm distance in the Y direction and 500 mm drift length	67

5.5	Track efficiency and purity for two tracks with 5 mm distance in the Y direction and 30 mm drift length	68
5.6	Track efficiency and purity for two tracks with 5 mm distance in the Y direction and 500 mm drift length	69
5.7	Track efficiency and track purity for the case that the scale factor of the fit range was one and 2 mm distance of two tracks in the Y direction	70
5.8	Track efficiency and track purity for the case that the scale factor of the fit range was one and 5 mm distance of two tracks in the Y direction	71
5.9	The scale factor 1.5 and 2 mm distance two tracks in the Y direction . .	72
5.10	The scale factor 1.5 and 5 mm distance two tracks in the Y direction . .	73
5.11	Track efficiency and track purity for 203 mm drift length and 2 mm distance in the Y direction	75
5.12	Two tracks simulation for the S-Z plane optimization	76
5.13	Track efficiency and purity for two tracks with 5 mm distance in the Z direction and 30 mm drift length	77
5.14	Track efficiency and purity for two tracks with 5 mm distance in the Z direction and 500 mm drift length	78
5.15	Track efficiency and purity for two tracks with 10 mm distance in the Z direction and 30 mm drift length	79
5.16	Track efficiency and purity for two tracks with 10 mm distance in the Z direction and 500 mm drift length	80
5.17	Track efficiency and track purity for the case that the scale factor of the fit range was one and 5 mm distance of two tracks in the Z direction	82
5.18	Track efficiency and track purity for the case that the scale factor of the fit range was one and 10 mm distance of two tracks in the Z direction .	83
5.19	The scale factor 1.5 and 5 mm distance two tracks in the Z direction . .	84
5.20	The scale factor 1.5 and 10 mm distance two tracks in the Z direction .	85
6.1	Large Prototype TPC at DESY	88
6.2	A sketch of the generation of electrons and positrons in DESY II	88
6.3	LP TPC end-plate and three modules position	89
6.4	The status of Octoboards during data taking	90
6.5	The pipeline of the physics analysis for the test beam data.	92
6.6	Occupancy plot for run 83 before implementing cut	93
6.7	Chain of the track reconstruction for test beam data.	95
6.8	xy-residual along the y-axis before correction	96
6.9	xy-residual along the y-axis after correction	96
6.10	Distribution of χ^2/ndf for merging process for before and after correction	97
6.11	An example of a reconstructed track for before and after correction process	98
6.12	Distribution of the number of hits on a track and D0 before and after cutting	98
6.13	The spectrum of the momentum for all runs.	100
6.14	The spectrum of $1/p_t$	101
6.15	Difference between the expectation and measurement momentum. . .	102
6.16	The X-Y residual distribution and the RMS distribution for run 135 . .	104
6.17	Z residual distribution for run 135.	105
6.18	The transverse spatial resolution the longitudinal spatial resolution for the runs 124 to 135	107

6.19	The transverse spatial resolution the longitudinal spatial resolution for the runs 76 to 88	109
6.20	The transverse spatial resolution the longitudinal spatial resolution for the runs 178 to 190	111
B.1	Track efficiency and track purity for the case that the scale factor of the fit range was 2 and 2.5, and 2 mm distance of two tracks in the Y direction	119
B.2	Track efficiency and track purity for the case that the scale factor of the fit range was 2 and 2.5, and 5 mm distance of two tracks in the Y direction	120
B.3	Track efficiency and track purity for the case that the scale factor of the fit range was 1.5,2 and 3, and 5 mm distance of two tracks in the Z direction	121
B.4	Track efficiency and track purity for the case that the scale factor of the fit range was 1.5, 2 and 3.5, and 10 mm distance of two tracks in the Z direction	122
C.1	samples of the track reconstruction	123
C.2	Tracks for the momentum resolution analysis	124
C.3	Tracks for the first package dataset for Transverse and longitudinal spatial resolution analysis	125
C.4	Tracks for the second package dataset for Transverse and longitudinal spatial resolution analysis	126
C.5	Tracks for the third package dataset for Transverse and longitudinal spatial resolution analysis	127

List of Tables

2.1	Performance and design parameters of the ILD TPC	9
2.2	The number of electron-ion pair and other parameters for different gas	14
4.1	The parameters for InGridBNDHoughTransformProcessor	59
4.2	The parameters for InGridCollectHitPostProcessor	60
5.1	The mandatory parameters for InGridDigitisationProcessor	63
5.2	The mandatory parameters for InGridTrackAnalysisProcessor	63
5.3	The parameters of the optimization	64
5.4	The scale factor of the ellipse axes in the X-Y plane.	74
5.5	The scale factor of the fit range in the X-Y plane.	74
5.6	The scale factor of the ellipse in the S-Z plane.	81
5.7	The scale factor of the fit range in the S-Z plane.	81
6.1	Parameters of six package datasets for the Z-scan	91
6.2	The compositions of gas mixture used for MAGBOLTZ simulation for runs 124-135	94
6.3	Drift velocity for runs 124-135 from MAGBOLTZ simulation.	94
6.4	Parameters used for each run for momentum scanning.	99
6.5	Energy spread of the T24 test beam area at DESY	99
6.6	Mometum and momentum resolution before cutting	102
6.7	Mometum and momentum resolution after cutting	102
6.8	Momentum resolution from Gluckstern equation and measurement	103
6.9	Parameters for runs 124 to 135	105
6.10	The drift length of runs 124 to 135.	106
6.11	Parameters for runs 76 to 88	108
6.12	The drift length of runs 76 to 88.	108
6.13	Parameters for runs 178 to 190	110
6.14	The drift length of runs 178 to 190.	110

Chapter 1

Introduction

The main task in high energy physics is to answer many questions about our universe. Although the Standard Model (SM) theory explains most of the observed phenomena in particle physics, still there are many open questions for which there are no explanations or predictions in this theory.

Dark matter, which about 30 % of the universe consists of it, dark energy, which causes the expansion of the universe to accelerate, the charge conjugation parity (CP) violation needed for description of the imbalance of the matter-antimatter after the Big Bang, are some examples of these phenomena. In the last centuries, many new models have been created, called Beyond Standard Models (BSM), in order to extend the Standard Model, and there is a demand for a powerful instrument to examine these models or discover new particles.

The Large Hadron Collider (LHC) at CERN is the most powerful collider for this purpose. The LHC is able to reach a center of mass energy up to 14 TeV. One of the great achievements for LHC was the discovery of the Higgs boson which is predicted in the Standard Model.

Due to the large background from strong interaction, the physics analysis in the LHC experiment is a sophisticated process and therefore limits the physics studies needing the high precision. For solving this limitation a Lepton collider can be a solution to overcome this limitation. The International Linear Collider (ILC) is one of the candidates for this purpose and to compensate the LHC limitation. The current plan is to build the ILC in Japan.

There are two detectors foreseen for the ILC. One of them is the International Large Detector (ILD). A Time Projection Chamber (TPC) is foreseen as the main tracking detector for the ILD. A TPC has several advantages. In a TPC tracks can be measured with three-dimensional space points (called hits). Because of the high density of the hits, the continuous tracking is possible. It can measure the specific energy loss of a charged particle used for particle identification. And another important advantage of a TPC is the low material budget.

The higher precision in the measurement results in a more accurate physics analysis. Hence, new technologies are required to reach this purpose. The Pixel-TPC devised more than ten years ago is one of these technologies. Bonn University in collaboration with other universities and institutes had two successful experiments with a pixelized readout system. The results achieved on the hardware level showed that this technology is promising for the future. However, the lack of an acceptable algorithm to do pattern recognition with a high efficiency made a big challenge to study more on the performance of this new readout system at the software level.

During many years many algorithms have been tried and tested. Most of them work for specific conditions such as an experiment without a magnetic field, in which the track is straight, or the tracks are parallel to the X-Y plane but they have not been successful for all conditions.

Some of them strongly suffer from the noise in the system. Therefore an algorithm has been highly demanded not only to be robust against the noise but also to work in every condition.

The main topic of this thesis is to develop such an algorithm which has been found. Both, simulation and real data show this algorithm is promising for a pixelized readout system and also for the Pixel-TPC for the future.

Chapter 2 of this thesis briefly introduces the ILC, the physics in the ILC and the TPC. Chapter 3 explains a general concept of the track reconstruction and different methods implemented for track finding and fitting. Moreover, in this chapter, there is a definition of some concepts used for analysis.

Chapter 4 illustrates the track finder algorithm developed for InGrid chips. Developing this algorithm was the main goal of this thesis. The simulation chain and the optimization of the code based on the simulation are illustrated in chapter 5. In addition to the optimization process, some analysis has been done for real data. The chain of preparation, cleaning data, and the results of the analysis are mentioned in chapter 6.

Chapter 2

Foundation

2.1 The Standard Model

The Standard Model is a quantum field theory model which describes known elementary particles and the interactions between them. Based on this model there are two general kinds of particles: fermions with half-integer spin and bosons with integer spin [1]. Figure (2.1) shows these particles and their categories.

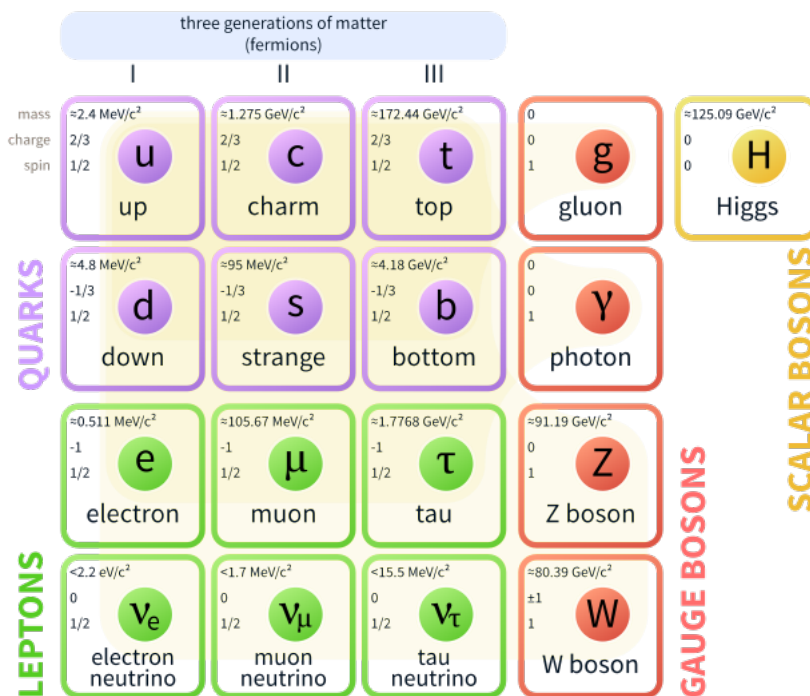


Figure 2.1: The Standard Model and the elementary particles [2].

The fermions are divided into two groups: leptons which carry electric charge one or zero, and quarks which carry $1/3$ or $2/3$ electric elementary charge. In general, these two groups are categorised into three generations. The first generation of the leptons includes the electron and electron neutrino and the quarks consist of the up and down quarks. These first generation particles are the lightest elementary particles which the stable matter surrounds us can be described by them. The other two generations are heavier particles. For this reason they are not stable and decay into the particles of the lower generation.

The bosons consist of four particles: the photon is the force carrier for the electromagnetic force, the gluon is the force carrier for strong force and Z and W^\pm are force

carrier for the weak force. In addition to these four particles, the Higgs boson (the scalar particle) is known as the boson particle with spin zero which was discovered by the LHC experiment [3][4]. The Higgs boson proves the Standard Model based on the mechanism of mass generation, i.e. is a theory which describes the origin of mass of the fundamental particles.

The Standard Model also includes a copy of the particles, mentioned above, with the inverse charge quantum number, known as antimatter. Despite the fact that the Standard Model can describe many phenomena, it is still not a complete theory. According to many astronomical observations, only about 4.9 % of our universe contains the ordinary matter explained by the Standard Model. The rest of the universe consists of about 26.8 % dark matter and 68.3 % dark energy which there is no explanation for them in the Standard Model [5]. Furthermore, there is no illustration in the Standard Model for other phenomena such as why the balance between matter and antimatter disrupt after Big Bang and so on. Therefore, other theories are needed to extend the Standard Model. In fact they have already been developed by many theoreticians. But they have to be examined and observe any evidence for them in an experiment. More information and overview of the Standard Model can be found in [1] and [6].

2.2 The International Linear Collider

One of the powerful tools for examining and finding any theory in particle physics are colliders. Generally, it consists of an accelerator, which accelerates bunches of two particles in opposite direction, and detectors, which are placed at an interaction region where two particles are collided to each other and can detect new particles from the collision.

The main motivation to have a lepton collider e.g. electron-positron collider is to have clear events in comparison with hadron colliders in which collision of two hadrons such as proton-proton happens. The last and largest lepton collider was the Large Electron-Positron Collider (LEP) with 208 GeV center of mass energy at the end up its operation (identified by LEP2) [7]. The LEP had a circular storage ring as an accelerator which causes a limitation to reach a higher center of mass energy. This limitation in a circular collider is because of the energy losses due to synchrotron radiation. This energy loss is calculated by

$$\Delta E \propto \frac{E^4}{m_0^4 \cdot r} \quad (2.2.1)$$

where m_0 is the mass of the particle at rest, E its energy and r the radius of the accelerator. According to equation (2.2.1), the energy loss per turn is inversely proportional to the fourth power of the particle's mass at rest and the radius of the storage ring. In order to reduce the energy losses, there are two main options; either using heavier particles such as proton used in Large Hadron Collider (LHC) [8] or increasing the radius of the storage ring. For the LEP2 with 208 GeV center of mass energy, the energy losses per turn (ΔE_{turn}) was 3.3 GeV. Meanwhile, the energy losses for LHC, using the same storage ring as LEP, is about $6 \cdot 10^{-6}$ GeV at 14 TeV center of mass energy. Comparison of these two numbers shows a significant reduction in case of using a heavier particle.

On the other hand, as mentioned before, another solution is to build a storage ring with a larger radius in the range of several tens of kilometers in order to reduce the energy losses to the same level as the LHC.

However, the cost and the time of building are issues. Hence, a linear collider is another solution in order to not only have clean events but also to reduce the energy losses.

The International Linear Collider (ILC) is one of the candidate colliders for the future of particle physics. Figure (2.2) shows a schematic of this collider. The ILC is a high-luminosity linear electron-positron collider with a center of mass energy of 250-500 GeV. It is also possibility to extend the ILC to 1 TeV [9] [10].

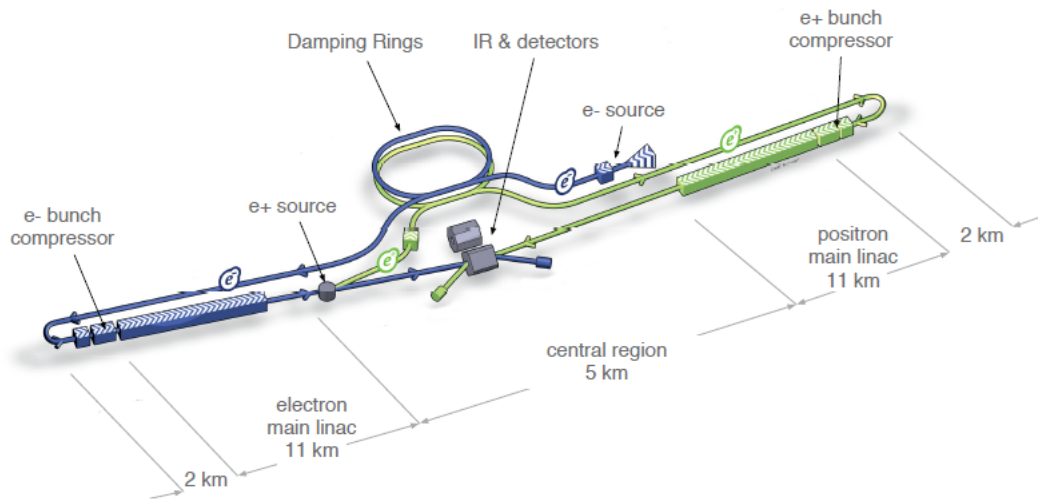


Figure 2.2: Schematic of the International Linear Collider (ILC) [11].

Generally, the ILC consists of the electron and positron source, the two damping rings, the two main linacs (with 22 km total length), the beam delivery system and two detectors. The polarized electrons are created by a photo-cathode DC gun and the polarized positrons are created via electron-positron pair production by photons. These photons are produced by passing the electrons through the main linac and a helical undulator. A Ti-alloy target is used for electron-positron pair production. More details of ILC are available in [9] [10].

At the interaction point, there are two detectors foreseen for ILC [12]; Silicon Detector (SiD) and International Large Detector (ILD) which share one interaction region based on the push-pull configuration.

For linear collider, it is possible to run it at any center-of-mass energy in the given range and also upgrade it to higher energies by extending the length of two main linacs. Another advantage is a possibility to have a polarized beam which is important in electroweak processes at high energies. And another advantage, as mentioned earlier, is in a linear collider the events are clean which leads to having less pileup and background events and hence more accurate analysis [13].

2.3 Physics at the ILC

As mentioned in the previous section, the main advantage of the ILC is to have clean environments which lead to having the higher precision to do the measurement. In fact, the ILC is a complementary collider for the LHC and many aspects of the physics can be measured with more precision which due to the background at the LHC their measurements either are not precise or impossible [14].

At the ILC the polarization of the beam can be chosen which causes to suppress background processes. In this section, two interesting examples of physics at the ILC will be briefly explained: Higgs physics and Top physics, and more details are available in [15].

2.3.1 Higgs physics

The Higgs-strahlung process is one of the most important processes which has to be studied at the ILC. According to this process, from the annihilation of an electron and a positron, a virtual Z boson is formed and it can emit a Higgs boson (figure (2.3-a)) and therefore the mass of the Higgs boson can be calculated, based on the recoil technique, by

$$M_H^2 = s + M_Z^2 - 2E_Z\sqrt{s} \quad (2.3.1)$$

where s is the initial state center of mass energy squared, M_Z is the Z boson mass and E_Z is the Z boson energy. At a center of mass energy of 250 GeV, the cross-section of the Higgs-strahlung process can reach to a maximum and this energy is the first stage of the running the ILC.

The energy of the Z boson can be reconstructed from the momenta of its decay products, for example from the momenta of electron-positron or muon-anti-muon [16]. At about 450 GeV as the center of mass energy, the Higgs production through WW fusion is dominating process (figure (2.3-b)). In this process, because the final state neutrinos cannot be directly reconstructed, therefore it is not possible to use the recoil technique. Hence, it is needed to rely on some exclusive Higgs decay such as $e^+e^- \rightarrow \nu\bar{\nu}H \rightarrow \nu\bar{\nu}b\bar{b}$ [17]. And from the center of mass energy 500 GeV, the trilinear Higgs self-coupling can be observed (figure (2.3)).

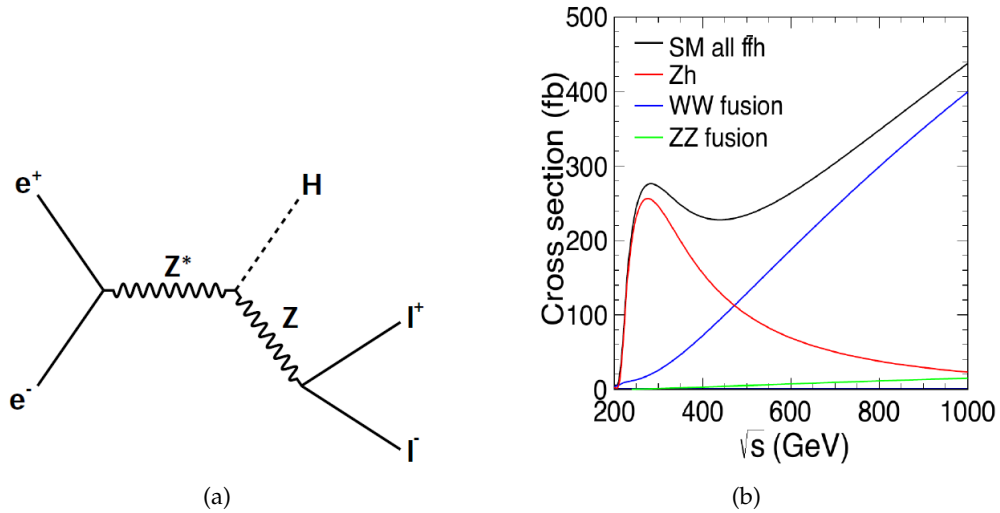


Figure 2.3: (a) Feynman diagram of Higgs-strahlung process [13] (b) Higgs production cross section for center of mass energies from 200 GeV up to 1 TeV [12].

It was mentioned above that the momenta of the Z boson decay will be utilized to reconstruct its energy. Hence, having a tracker detector with high momentum resolution is one of the important issues for ILD. For instance, figure (2.4) shows the result of simulation for distribution of mass recoiling from Z boson decay into two

muons at 500 GeV as the center of mass energy for two different momentum resolutions. From this figure, one can see how the momentum resolution can change the shape of the peak of signals for the simulated Higgs boson with mass 120 GeV. A Time Projection Chamber (TPC), i.e. a gaseous detector, is considered as the main tracker detector for ILD (see section 2.4). For this detector, one of the characteristics is to have a momentum resolution better than $2 \times 10^{-5} \text{ GeV}^{-1}$ and based on the technologies assumed to implement for this detector, this requirement is achievable (see section 2.5).

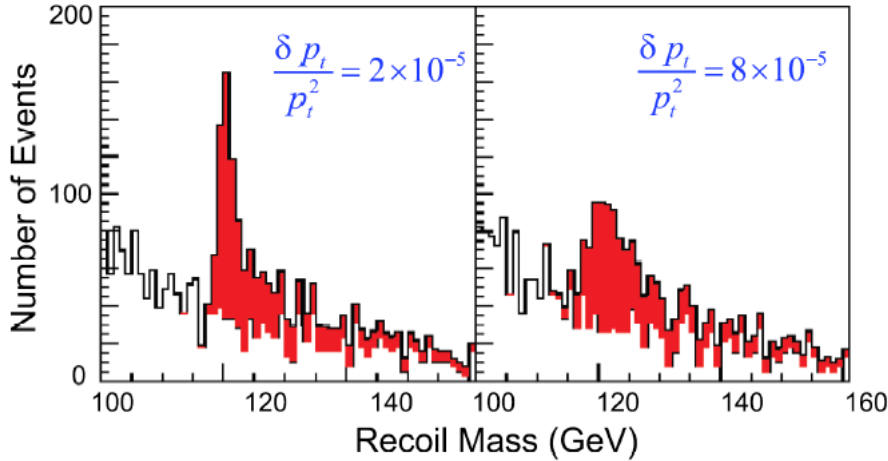


Figure 2.4: Simulation of the Higgs recoil mass based on the momentum of $\mu^+\mu^-$ production from the Z boson decay with two different momentum resolutions [15]. The left figure uses the resolution that should be reached with the ILD TPC.

2.3.2 Top physics

In the Standard Model the heaviest particle is the top quark and because of its mass, it is strongly coupled to the electroweak symmetry breaking mechanism [15]. Hence, top quark hints us to any new physics at the TeV energy scale. The top quark was discovered at the Tevatron proton-antiproton collider and up to now, it has been studied at hadron colliders, Tevatron and LHC [18] [19].

At the ILC, for studying the top quark the leptonic initial state is defined precisely and it results in a clean environment in which every individual event can be analyzed in details. In addition, it changes the production mechanism for top quark pairs to the electroweak interactions from the strong interactions which are more important to explore the electroweak symmetry breaking phenomena.

Moreover, it gives us a possibility to have experiments which are sensitive to the coupling of the top quark to possible new interactions such as weak interaction polarization and parity asymmetries. Thus, the study of top quark brings new expectation at the ILC in comparison with the Standard Model expectation at the LHC. More information and studies for top physics at ILC is available in [15].

2.4 The International Large Detector

The International Large Detector (ILD) is one of the main detector foreseen for ILC. It consists of different layers (sub-detector) for different tasks. Figure (2.5) shows a schematic of the ILD and some of the sub-detectors and they will be explained as follow [12]:

- **Vertex Detector (VTX):** consists of three super layers and each super layer contains two layers or a 5 layer geometry of silicon pixel detector. It is used to measure the position of the interaction point and also identify and reconstruct short-lived particles.
- **Time Projection Chamber (TPC):** is a gaseous tracker detector implemented as the main tracker of the ILD. Many three-dimensional points, minimum material budget in the field cage and in the end plate and also a possibility to measure dE/dx for particle identification are the advantages of the TPC (see section 2.5).
- **Electromagnetic Calorimeter (ECAL):** is segmented with 30 samples in depth and small transverse cell size. They are split into a barrel and end cap system. Tungsten has been chosen as the absorber and silicon diodes or scintillator strips are considered for the sensitive area. The ECAL measures the energy of the particles which interact via the electromagnetic interaction.
- **Hadronic Calorimeter (HCAL):** is segmented with 48 longitudinal samples and small transverse cell size. There are two options; one uses scintillator and another one uses a gas-based readout. Both options are based on a Steel-absorber structure. It measures the energy of the particles which interact via the strong force.
- **Muon System:** is the outermost detector of the ILD. It measures the muon particles.
- **Coil:** surrounds the calorimeters. It can create an axial B-field of 3.5 Tesla.

In addition to the sub-detectors explained above, there are other sub-detector layers which are illustrated in details in [12]. The ILD has been designed based on the particle flow concept [21]. In this case, every measurement in the detector is assigned to one particle. The low material budget for the main tracker detector which causes to have less scattering and energy loss, and the large volume for higher double tracks resolution are other advantages of the ILD detector.

2.5 The Time Projection Chamber

The Time Projection Chamber (TPC) was invented in the 1970s by David R. Nygren [22]. A TPC is a gaseous detector which measures the momentum and the energy loss of charged particles. Generally, a TPC consists of a large gas volume which is enclosed in a chamber and an anode and cathode walls (figure (2.6)). For the ILD, the TPC is constructed as a cylindrical barrel. The cathode is in the center and two anodes at each end cap. There is an inner cylinder hold inside the TPC for the beam pipe and vertex detector. There are three silicon tracker layer which the TPC is enveloped by them: one between the vertex detector and the TPC called Silicon Inner Tracker (SIT), one between the TPC and calorimeter in the barrel called Silicon External Tracker

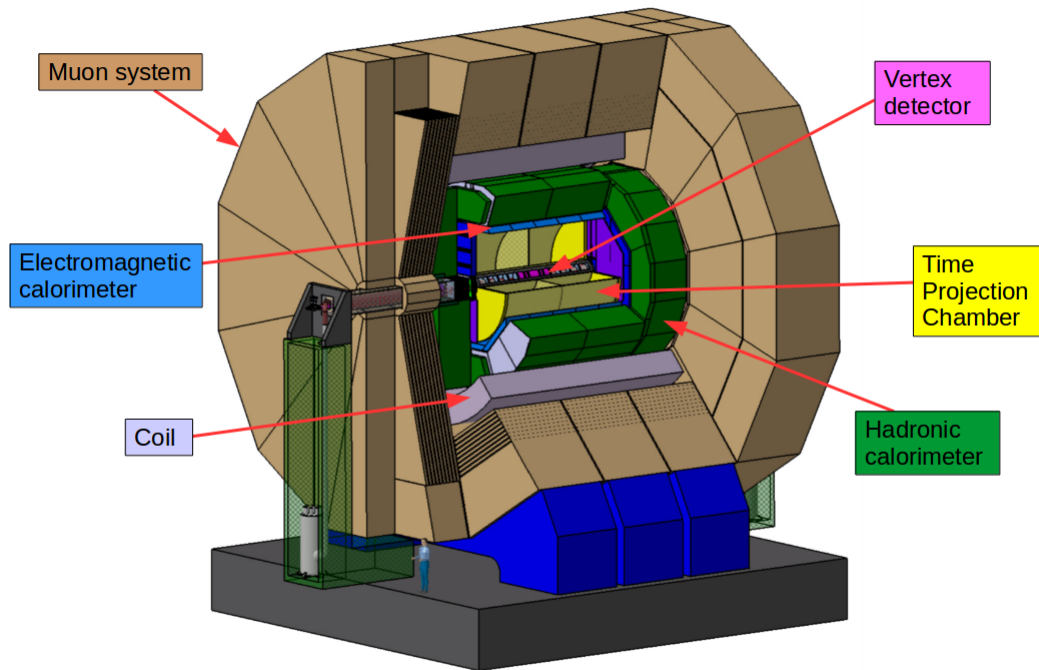


Figure 2.5: Schematic of the International Large Detector (ILD) [20].

(SET) and the last one is the Endcap Tracking Detector (ETD) between the TPC and the end cap region [12]. Figure (2.6) shows the schematic of a TPC and table (2.1) illustrates the performance and design parameters of the ILD TPC.

Parameter	r_{in}	r_{out}	z
Geometrical parameters	329 mm	1808 mm	± 2350 mm
Solid angle coverage	up to $\cos \theta \simeq 0.98$ (10 pad rows)		
TPC material budget	$\simeq 0.05 X_0$ including outer fieldcage in r $< 0.25 X_0$ for readout endcaps in z		
Number of pads/timebuckets	$\simeq 1-2 \times 10^6/1000$ per endcap		
Pad pitch/ no.padrows	$\simeq 1 \times 6 \text{ mm}^2$ for 220 padrows		
σ_{point} in $r\phi$	$\simeq 60 \mu\text{m}$ for zero drift, $< 100 \mu\text{m}$ overall		
σ_{point} in rz	$\simeq 0.4 - 1.4 \text{ mm}$ (for zero - full drift)		
2-hit resolution in $r\phi$	$\simeq 2 \text{ mm}$		
2-hit resolution in rz	$\simeq 6 \text{ mm}$		
dE/dx resolution	$\simeq 5 \%$		
Momentum resolution at $B=3.5 \text{ T}$	$\delta(1/p_t) \simeq 10^{-4}/\text{GeV}/c$ (TPC only)		

Table 2.1: Performance and design parameters of the ILD TPC [12].

Due to the interaction of a charged particle passing through a TPC with gas atoms, the gas is ionized and therefore many free electrons and ions are generated along its trajectory. This process is called primary ionization and the free electrons are recognized as primary electrons. By applying an electric field the free electrons are drifted to the anode plate, where a readout system is placed. The ions are drifted to the cathode. Normally, the electric field lines are parallel to the beam pipe and perpendicular to the end caps. The readout system, by registering the signal from primary electrons and measuring the time of arrival, can give three-dimensional space points used for reconstruction of the trajectory of the charged particle.

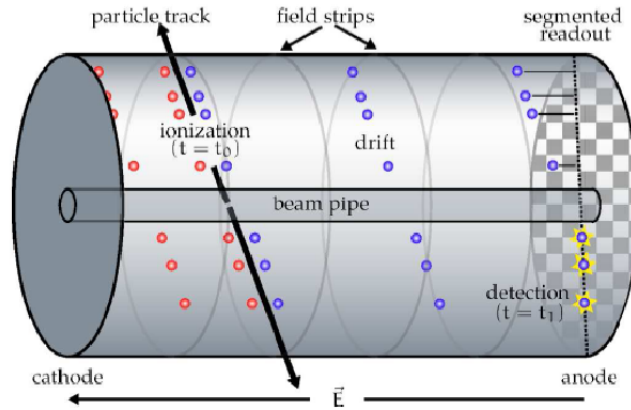


Figure 2.6: Schematic of a TPC [23].

Owing to the fact that the signal from the primary electrons is so weak, the registration of the signal is not done directly. Thus a gas amplification structure is placed at the anode. Additionally, a magnetic field is also implemented parallel to the electric field. This magnetic field bends the direction of the flight of the charged particles with respect to the end planes. In the following subsection the concept of ionization, drift, diffusion, gas amplification and momentum resolution calculation will be explained.

2.5.1 Interaction of charged particles with matter

The interaction of a charged particle with matter happens through different processes such as elastic scattering on electrons, deflection in the Coulomb field of an atom, inelastic scattering with the nucleus and so on. The electromagnetic interaction is one of these processes which causes the excitation and ionization of the medium.

Normally this interaction is the largest fraction of the interactions, particularly for the range of the energy between 1 GeV to 100 GeV of the charged particles. For charged particles with higher energy radiative processes e.g. Cherenkov radiation, transition radiation and bremsstrahlung are to be taken into account. The maximum energy transferred to an atomic electron (m_e) is given by [24] [25]

$$E_{kin}^{max} = \frac{2m_e p^2}{m_0^2 + m_e^2 + 2m_e E/c^2} \quad (2.5.1)$$

where m_0 is the rest mass of the incident particle, E its energy and p its momentum. Due to the fact that the electron is already there and there is no need to be produced, the kinetic energy is used instead of the total energy. The treatment of the maximum

transferable kinetic energy for an electron with mass m_e is different from a heavy particle ($m_0 \gg m_e$). For a heavy particle with an assumption that $((m_e/m_0)^2 \ll 1)$, equation (2.5.1) is given by

$$E_{kin}^{max} = \frac{p^2}{\gamma m_0 + m_0^2/2m_e} \quad (2.5.2)$$

where $\gamma = E/m_0c^2$ is the Lorentz factor. For relativistic particles $E_{kin} \approx E$ and $E \approx pc$ equation (2.5.2) can be written as

$$E^{max} = \frac{E}{E + m_0^2c^2/2m_e} \quad (2.5.3)$$

The energy loss dE per track length dx in matter for charged heavy particles is given by the relativistic Bethe-Bloch formula [24]

$$-\frac{dE}{dx} = 4\pi N_A r_e^2 m_e c^2 z^2 \frac{Z}{A} \cdot \frac{1}{\beta^2} \left[\ln \frac{2m_e c^2 \gamma^2 \beta^2}{I} - \beta^2 - \frac{\delta}{2} \right] \quad (2.5.4)$$

with

N_A Avogadro's number

Z, A atomic number and atomic weight of the absorber

z charge of the incident particle in unit of the elementary charge

r_e classical electron radius

β the velocity of the incident particle in terms of the velocity of light c

$\gamma = \frac{1}{\sqrt{1-\beta^2}}$

I ionization constant

δ correction term for the density effect.

With approximation for the maximum transferable kinetic energy, the Bethe-Bloch formula can be written as

$$-\frac{dE}{dx} = 2\kappa \left[\ln \frac{E_{kin}^{max}}{I} - \beta^2 - \frac{\delta}{2} \right] \quad (2.5.5)$$

where

$$\kappa = 4\pi N_A r_e^2 m_e c^2 z^2 \frac{Z}{A} \frac{1}{\beta^2}$$

Usually the energy loss is given in units of $\frac{\text{MeV}}{\text{g/cm}^2}$. For the heavy particles with lower energy, the energy loss decreases with $1/\beta^2$ and reaches a minimum of ionization at about $\beta\gamma \approx 4$. The particles with the energy loss at this minimum level are called Minimum Ionizing Particles (MIPs). The energy loss increases again because of the logarithm term in equation (2.5.4). As an example of the energy deposition for a particle heavier than the electron, figure (2.7) shows the energy deposition of a muon as a function of $\beta\gamma$. In this spectrum, the Bethe-Bloch equation is valid in the Bethe region, identified in this figure.

For the electron as the incident particle, the maximum energy transferred to an atomic electron is [24]

$$E_{kin}^{max} = E - m_e c^2 \quad (2.5.6)$$

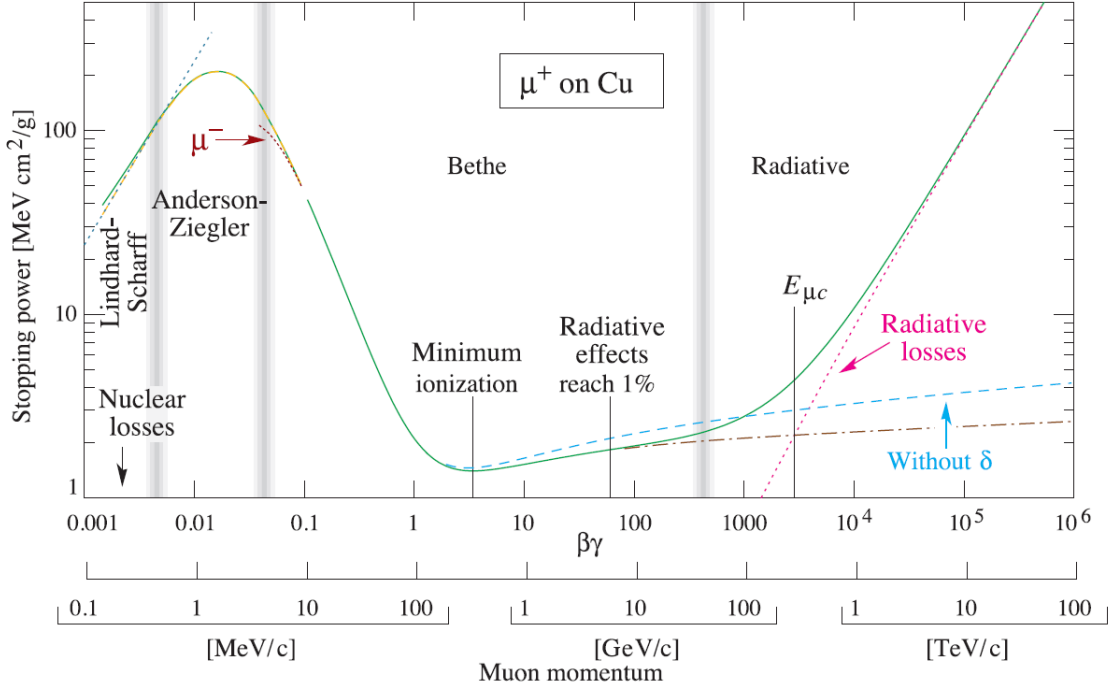


Figure 2.7: The energy deposition of a muon as a function of $\beta\gamma$. The Bethe-Bloch equation is valid only in the Bethe region [26].

And the energy loss of electrons is approximated by

$$-\frac{dE}{dx} = 4\pi N_A r_e^2 m_e c^2 \frac{Z}{A} \cdot \frac{1}{\beta^2} \left[\ln \frac{m_e c^2 \gamma}{2I} - \beta^2 - \frac{\delta^*}{2} \right] \quad (2.5.7)$$

where δ^* takes a different value in comparison with δ in equation (2.5.4). The treatment of the energy loss for positrons with low energy is different from electrons. The main reason is the positrons annihilate with an electron into two photons [24].

The Bethe formula describes only energy losses due to the ionization and excitation. As mentioned before for higher energies, radiation losses have a more important role. In addition, equation (2.5.4) describes the mean value of the energy loss per path length. For thin absorbers, i.e. mainly for gases, the distribution of the energy loss is asymmetric and it has a long tail. This distribution can be described by a Landau distribution [27].

The Landau fluctuations of the energy loss are due to the transfer of a large amount of energy from the incidence particle to atomic electrons. In such a case, the ionization electrons have a large energy that can cause further ionization. These electrons are called delta electrons.

Normally detectors measure the energy which is deposited in their sensitive volume, therefore the strong fluctuations of the energy loss are not frequently observed by a detector. For this reason, it is often better to consider an energy which is less than a cut value (E_{cut}). Thus, this truncated energy loss is [24]

$$-\frac{dE}{dx} |_{\leq E_{cut}} = \kappa \left[\ln \frac{2m_e c^2 \gamma^2 \beta^2 E_{cut}}{I^2} - \beta^2 - \delta \right] \quad (2.5.8)$$

Due to the fact that the Bethe-Bloch equation depends on the mass of the incidence particle, by measuring the specific energy loss and the momentum of the particle it is possible to determine the type of particle. Figure (2.8) shows an example of measurement of the specific energy loss in the ALICE TPC [28].

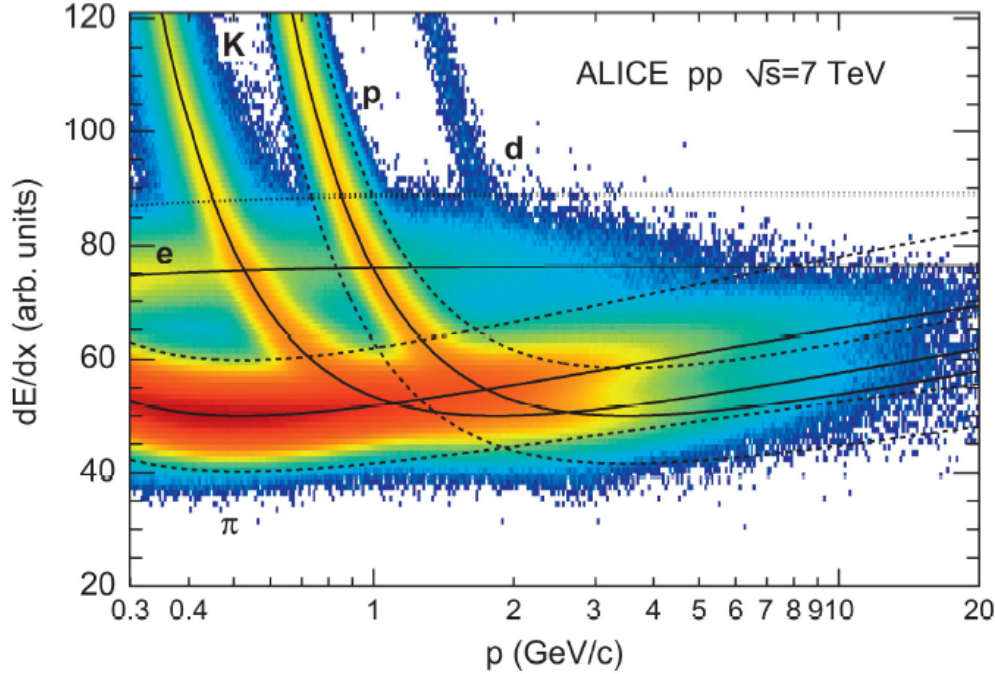


Figure 2.8: The spectrum of the energy loss against the momentum in the ALICE TPC from pp collisions at $\sqrt{s} = 7$ TeV [28].

2.5.2 Ionization yield

For the gaseous tracking detector, there are different ionization mechanisms. As mentioned before, one must distinguish between primary and secondary ionization. In primary ionization, the encountering of a fast charged particle with the atoms of the gas mixture causes one or sometimes two or three electrons to be ejected. For instance, the process of primary ionization of atom A encountered by π meson is [29]



However, most of the charge along a track is from secondary ionization. This is the result of either collision of ionization electrons with an atom or through intermediate excited A^* . The excitation of A^* is often a metastable state of a noble gas which can be created by either incidence particle or electrons from primary ionization. If the excitation energy of A^* is above the ionization potential of atom B in inhomogeneous absorber materials as gas mixture, then it causes secondary ionization and is called Penny effect.



Moreover, A^* can be an optical excitation with a long lifetime. In this case, this effect is called Jesse effect [29]. The total number of electron-ion pairs, identified by n_T , depends on the ionization potential of the gas (I_0) and the average energy needed to create an electron-ion pair (W). n_T includes the number of primary ionization (n_P) and secondary ionization.

$$n_T = \frac{\Delta E}{W} \quad (2.5.11)$$

where ΔE is the energy deposition. Table (2.2) illustrates these parameters for different gas mixture.

Gas	I_0 [eV]	W [eV]	$\frac{dE}{dx}$ [$\frac{\text{keV}}{\text{cm}}$]	n_P [$\frac{1}{\text{cm}}$]	n_T [$\frac{1}{\text{cm}}$]
He	24.5	41	0.32	4.2	8
Ne	21.56	36.3	1.56	12	43
Ar	15.7	26	2.44	23	94
Xe	12.1	22	6.76	44	307
CF ₄	15.9	54	7	51	100
DME	10.0	23.9	3.9	55	160
CO ₂	13.7	33	3.01	35.5	91
CH ₄	15.2	28	1.48	25	53
C ₂ H ₆	11.7	27	1.15	41	111
iC ₄ H ₁₀	10.6	23	5.93	84	195

Table 2.2: The number of electron-ion pair and other parameters for different gas at 20⁰ C and 1013.25 mbar for minimum ionising particle [30].

2.5.3 Drift and Diffusion

The motion of a charged particle in the presence of an electric and magnetic field is represented in terms of an equation of motion [29]

$$m \frac{dv}{dt} = e\mathbf{E} + e(\mathbf{v} \times \mathbf{B}) - K\mathbf{v} \quad (2.5.12)$$

where m and e are the mass and electric charge of the particle, \mathbf{v} is its velocity and K is a frictional force proportional to the velocity. This frictional force is from the interaction of the particle with the gas. The average time between two collisions (τ) is defined as the ratio of the mass over K . For the case that $t \gg \tau$, the acceleration by the Lorentz force is compensated by the frictional force (steady state). Thus the drift velocity (\mathbf{v}_d) is constant and equation (2.5.12) reads

$$\frac{\mathbf{v}_d}{\tau} - \frac{e}{m}(\mathbf{v}_d \times \mathbf{B}) = \frac{e}{m}\mathbf{E} \quad (2.5.13)$$

The solution of the drift velocity is derived from equation (2.5.13) to be

$$\mathbf{v}_d = \frac{e}{m}\tau|\mathbf{E}|\frac{1}{1+\omega^2\tau^2}(\hat{\mathbf{E}} + \omega\tau[\hat{\mathbf{E}} \times \hat{\mathbf{B}}] + \omega^2\tau^2(\hat{\mathbf{E}} \cdot \hat{\mathbf{B}})\hat{\mathbf{B}}) \quad (2.5.14)$$

where $\hat{\mathbf{E}}$ and $\hat{\mathbf{B}}$ denote the unit vectors in the direction of the fields and $\omega = (e/m)|\mathbf{B}|$ is the cyclotron frequency of the electron. In the absence of a magnetic field, equation (2.5.14) is simplified to

$$\mathbf{v}_d = \frac{e}{m}\tau\mathbf{E} = \mu\mathbf{E} \quad (2.5.15)$$

where $\mu = e\tau/m$ is the mobility. In the presence of a magnetic field, the amplitude of \mathbf{v}_d is given by

$$|\mathbf{v}_d(\omega)| = \frac{1 + \omega^2\tau^2 \cos(\phi)}{1 + \omega^2\tau^2} \cdot |\mathbf{v}_d(0)| \quad (2.5.16)$$

where $\mathbf{v}_d(0)$ is the drift velocity at $\mathbf{B} = 0$ and ϕ is the angle between electric and magnetic field [29]. After the primary ionization, a charge cloud of electrons from ionization in a gas diffuses because of the thermal movement. The thermal energy is given by $\epsilon_{therm} = 3/2k_B T$. k_B is the Boltzmann constant and T is the gas temperature. With an external electric field and drifting electrons, the total energy of a charge carrier is given by

$$\epsilon_{total} = \epsilon_E + \frac{3}{2}k_B T \quad (2.5.17)$$

with $\epsilon_E = 1/2m\mathbf{v}_d^2$ as the kinetic energy. For some gases such as Argon, the total energy is dominated approximately by kinetic energy. These kind of gases are known as *hot* gases. In contrast to hot gases, there are *cold* gases such as CO₂ which their total energy is dominated by thermal energy.

The drifting electrons and the diffusion simultaneously cause the charge cloud after some time t at $z_d = tv_d$ to show a Gaussian distribution as follows [23] [29]

$$n = \left(\frac{1}{\sqrt{4\pi\tilde{D}t}} \right)^3 \exp\left(-\frac{r^2(t)}{4\tilde{D}t} \right) \quad (2.5.18)$$

where $r^2(t) = x^2 + y^2 + (z - z_d(t))^2$ and \tilde{D} is diffusion coefficient and given by [31]

$$\tilde{D} = \frac{2}{3} \frac{\epsilon_{total}\tau}{m} \quad (2.5.19)$$

which shows the dependency of the diffusion coefficient on the gas mixture because of the total energy term. From equation (2.5.18) the width of the Gaussian distribution (σ), known as the resolution, in any direction is

$$\sigma = \sqrt{2\tilde{D}t} \quad (2.5.20)$$

With implementing an electric field the diffusion coefficient constant (D) is defined based on the drift velocity as

$$D = \sqrt{\frac{2\tilde{D}}{v_d}}$$

Thus, equation (2.5.20) can be written based on the Z position as

$$\sigma = D\sqrt{z_d} \quad (2.5.21)$$

where z_d is the drift length. For a TPC because the electric field is in the Z direction, and according to the equation (2.5.21), the collision is more probable along the drift length.

Thus, the width of the distribution in the X and Y directions is different from the one in the Z direction. For this reason, there are two diffusion coefficient constants, one for the X and Y directions (D_T) and another one for the Z direction (D_L). Hence, according to equation (2.5.18) there are two resolutions: one for the X and Y direction (σ_T) and one for the Z direction (σ_L) as follows:

$$\sigma_T = D_T \sqrt{z_d} \quad \text{and} \quad \sigma_L = D_L \sqrt{z_d} \quad (2.5.22)$$

σ_T and σ_L are called transverse and longitudinal resolution, respectively. The diffusion constants have a dependency on the gas mixture used in the TPC. With implementing a magnetic field parallel to the electric field, the trajectory of the electrons has a helix shape and it causes the transverse diffusion constant to be reduced in comparison with the case without magnetic field with a factor as follow:

$$D_T(B) = \frac{D_T(B=0)}{1 + \omega^2 \tau^2} \quad (2.5.23)$$

Meanwhile, the magnetic field does not have any influence on the longitudinal diffusion. For the ILC TPC, the studies show T2K gas (95 % Ar, 3 % CF₄, 2 % iC₄H₁₀) is promising to have a high drift velocity meanwhile the diffusion is minimal. Figure (2.9) shows the transverse diffusion constant and the drift velocity in T2K gas versus the electric field.

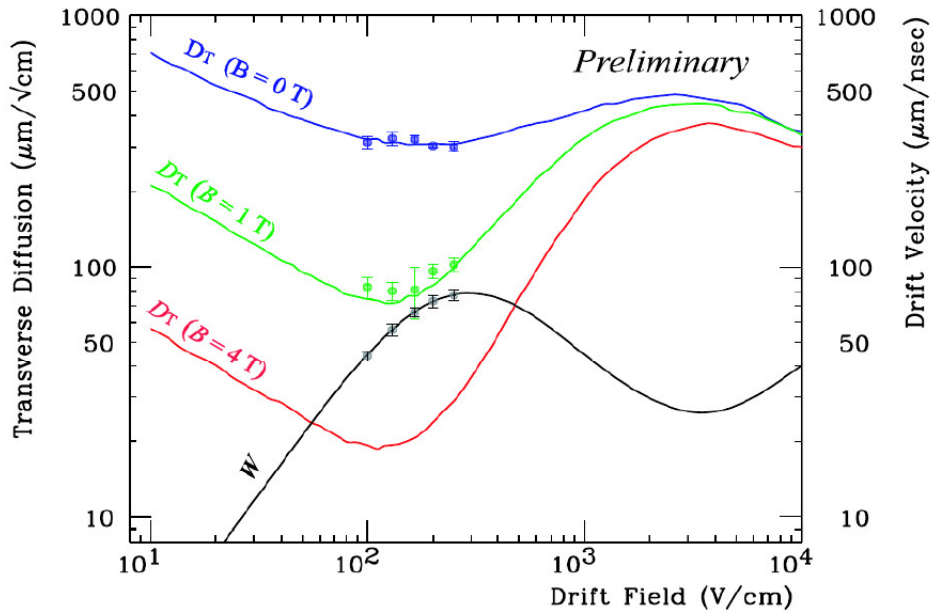


Figure 2.9: Simulation and measurement results of the transverse diffusion constant D_T for $B=0, 1$ and 4 T and the drift velocity (black line identified by W) against the electric field measured in T2K gas. The points are from experiment and the solid lines are from simulation with Magboltz [32].

2.5.4 Gas amplification

The primary electrons from the ionization process because of the drifting arrive at the end plate where is the host of the readout system and they must be detected and registered with a high timing precision. However, the current available readout systems are not sensitive to detect a single electron and therefore the charge has to be amplified. One of the common solutions is Proportional wires [26] [29].

Nevertheless, this method cannot be used for ILD TPC due to the lack of the ability to fulfill the requirements such as resolution and the material budget for the ILD TPC. For the ILD TPC, a new amplification technology is required. Micro-Pattern Gaseous Detectors (MPGDs) are reasonable options. Based on these techniques, a second region is formed in front of the end plate, being the host of the readout system. This region is called the amplification region. By applying an electric field in this region, the primary electrons are accelerated up to energies that they can ionize the gas. New electrons from these ionizations are called secondary electrons. The secondary electrons are accelerated and form an avalanche of the charge which provides the signal which can be detected by electronic systems.

Two types of the MPGDs which are under investigation, are the Gas Electron Multiplier (GEM) [33] and the Micro Mesh Gaseous Structure (Micromegas) [34] and a brief introduction of these two methods are presented in the following.

Gas Electron Multipliers

GEM was invented by Fabio Sauli in 1996. It is a foil of isolating material (Kapton) with $50 \mu\text{m}$ thickness and coated with copper. There are many holes which are etched or drilled into the foil in a regular pattern. By applying a potential difference between the two sides of the GEM, the electrons are accelerated through the holes and generate the secondary electrons. For a GEM the gas amplification can reach values of 10-1000 and this is at the edge of electronic sensitivities.

For higher gains, the probability of the discharged increases which causes the stability of the GEM decreases. For this reason, normally two or more GEMs are placed on top of each other. The field in the space between the GEMs is called transfer field and the field between the last GEM and the readout system is called induction field. The ion backflow i.e. ions generated in the secondary ionization can be minimized by applying different fields and shifting the different GEMs with respect to each other [35]. Figure (2.10) shows a GEM and the shape of field lines in a GEM.

Micromegas

The Micromegas was invented by Yannis Giomataris in 1995. It consists of a thin metallic grid which separates the drift region from the amplification region. The grid is mounted between 10 to $100 \mu\text{m}$ on top of the readout system and it is on high potential with respect to the anode. The typical gains for Micromegas are a few thousands, however, it is possible to reach also up to 10^5 . The advantage of Micromegas is that the avalanche of electrons can reach to readout system very fast, about 1 ns. Another characteristic of the Micromegas is because the amplification gap is small, the avalanche ends up on a narrow area at the readout system. For pad readout system which needs the charge spread over several pads, this characteristic is a drawback. In contrast in pixelized readout, it can be an advantage. The InGrid which the main topic of this thesis is to develop a pattern recognition algorithm for that is a combination of the Micromegas and Timepix chip (see section 2.8).

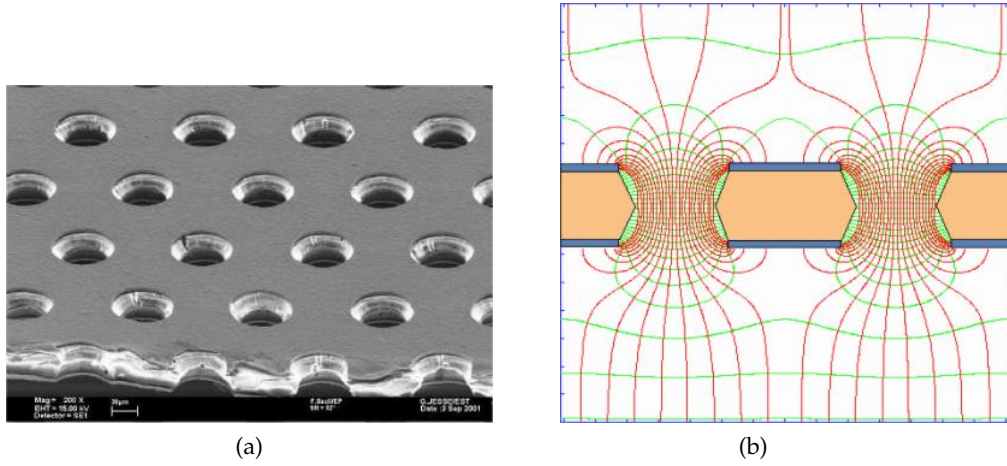


Figure 2.10: (a) Scanning Electron Microscope (SEM) image of a GEM with $50 \mu\text{m}$ thickness and its holes with $70 \mu\text{m}$ diameter. The distance between each hole is $140 \mu\text{m}$. (b) Schematic of the field lines pass through a hole for a GEM amplification structure [36].

2.5.5 Momentum resolution

The decomposition of the momentum $\mathbf{P} = [p_x, p_y, p_z]$ of a particle in spherical coordinate system is [37]

$$\begin{aligned} p_x &= P \cdot \sin(\theta) \cdot \cos(\phi) \\ p_y &= P \cdot \sin(\theta) \cdot \sin(\phi) \\ p_z &= P \cdot \cos(\theta) \end{aligned} \quad (2.5.24)$$

which has three components in three directions. In equation (2.5.24), θ and ϕ are azimuthal and zenith angle, respectively. With implementing a homogeneous magnetic field parallel or anti-parallel to the z-axis, bending the radius of the trajectory of a charged particle is given by the Lorentz equation [38]

$$\frac{mv^2}{r} = |q\mathbf{v} \times \mathbf{B}| = qv_{\perp} \cdot |\mathbf{B}| \quad (2.5.25)$$

Because the Lorentz force is perpendicular to the velocity, the energy of the particle maintains constant and it implies a helix trajectory. Therefore the trajectory of the charged particle can be separated into a circular motion in the X-Y plane and a straight line in the Z direction. The momentum of the charged particle can be written as:

$$\begin{aligned} p_t &= P \cdot \sin(\theta) = \sqrt{p_x^2 + p_y^2} \\ p_z &= P \cdot \cos(\theta) \end{aligned} \quad (2.5.26)$$

where p_t is the component of the momentum orthogonal to the magnetic field and called transverse momentum, and p_z is the component parallel to \mathbf{B} field. From equations (2.5.25) and (2.5.26) the radius of the circle (r) can be calculated [38]

$$r[m] = \frac{p_t[GeV/c]}{a \cdot B[T]} \quad (2.5.27)$$

where with the unit-dependent constant (reference [39], chapter 12)

$$a = (10^{-9} \frac{c}{m/s}) \cdot \frac{[length]}{m} \frac{GeV/c}{T \cdot [length]} \approx 0.29979 \frac{GeV/c}{T \cdot m} \quad (2.5.28)$$

Equation (2.5.27) is practical for charged particles with low energy which cannot leave the tracking detector. For other charged particles with high energy passing through the tracker detector, tracking measurements are only on a limited arc length of the circle. In such a case, the radius of curvature is calculated in terms of the measured *sagitta*. As it is shown in figure (2.11), the sagitta, s , is related to the radius, r , as [38]

$$s = r - \sqrt{r^2 - (L/2)^2} = r - r\sqrt{1 - (L/2r)^2} \approx \frac{L^2}{8r} \quad (2.5.29)$$

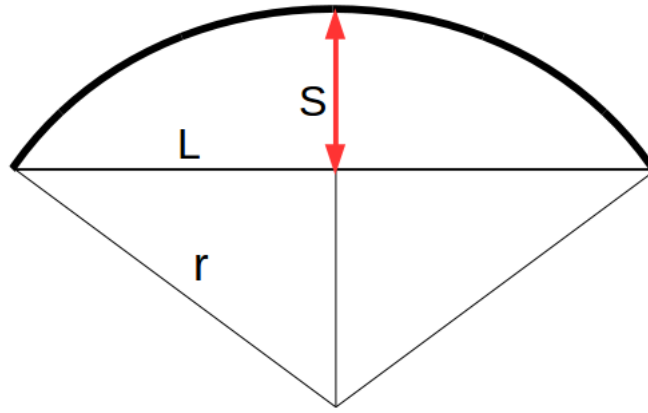


Figure 2.11: The sagitta of a circle with radius r and the arc length L .

According to equation (2.5.27) and for the case that $L \ll r$ the transverse momentum and the inverse transverse momentum of a particle are [38]

$$p_t = \frac{0.3BL^2}{8s} \quad \text{and} \quad \frac{1}{p_t} = \left(\frac{8}{0.3BL^2} \right) s \quad (2.5.30)$$

From equation (2.5.30) the momentum resolution is calculated

$$\delta\left(\frac{1}{p_t}\right) = \left(\frac{\sigma_{p_t}}{p_t^2}\right) = \left(\frac{8}{0.3BL^2}\right) \delta s \quad (2.5.31)$$

Because the uncertainty of the sagitta (δs) depends on the single point measurement precision (σ_{xy}), therefore the equation (2.5.31) can be written as

$$\left(\frac{\sigma_{p_t}}{p_t^2}\right) = \left(\frac{8}{0.3BL^2}\right) \sigma_{xy} \quad (2.5.32)$$

where the single point resolution is presumed to be Gaussian distributed around the track. Consequently, the inverse momentum is Gaussian distributed. From equation (2.5.32) it is clear that the momentum resolution is inversely proportional to the magnetic field and also the square of the lever arm (L).

In order to achieve the highest momentum resolution, the easiest way is to increase L . However, because a calorimeter and a solenoid outside the tracking system scale in volume like L^3 , hence, this method is very costly [38].

As stated by Gluckstern approach [40], the momentum resolution can be written in terms of point measurement resolution, multiple scattering and the optimum spatial distribution of the measured points. Generally, a path of a track is not a straight line because of two main reason: the magnetic field which bends the trajectory of a charged particle, and multiple scattering due to the interaction of a charged particle with the nuclei of the medium.

According to equation (2.5.27), one can define the curvature of the track as $k = \frac{1}{r}$. The uncertainty of the curvature has two terms; one is δk_{sag} for the sagitta due to the bending of the trajectory and δk_{MS} because of the multiple scattering. For N equally spaced points on a track with spatial precision σ_{xy} , the momentum resolution in term of the sagitta is [40]

$$\delta k_{sag} = \frac{\sigma_{xy}}{L^2} \sqrt{\frac{720}{N+4}} \quad (2.5.33)$$

If one end of the track can be identified, for example the vertex point, then the numerical value 720 reduces to 320. Moreover, the optimum distribution is $N/2$ of the measurement at the center and $N/4$ of the measurements at each end [39][40]. Another term of the uncertainty of the curvature because of the multiple scattering is

$$\delta k_{MS} = \frac{0.0157 GeV/c}{L p_t} \sqrt{\frac{L}{X_0}} [1 + 0.038 \ln(L/X_0)] \quad (2.5.34)$$

where X_0 is the radiation length. This equation is an approximation for relativistic particles which $\beta \approx 1$. For a TPC because of $X_0 \gg L$, the logarithmic term of equation (2.5.34) is negligible therefore this equation is simplified to

$$\delta k_{MS} \approx \frac{0.0157 GeV/c}{p_t} \sqrt{\frac{1}{L X_0}} \quad (2.5.35)$$

Hence, the total momentum resolution is calculated in accordance with formulas (2.5.27), (2.5.34) and (2.5.35):

$$\frac{\sigma_{p_t}}{p_t^2} = \frac{\sigma_{xy}}{0.3 B L^2} \sqrt{\frac{720}{N+4}} \oplus \frac{0.0157 GeV/c}{0.3 B p_t} \sqrt{\frac{1}{L X_0}} \quad (2.5.36)$$

The momentum resolution for ILD TPC with $N=220$, $L \approx 1.5$ m, $B=3.5$ T, and $X_0 = 110 \text{ g} \cdot \text{cm}^{-2}$ has to be 10^{-4} . This requirement resolution is from the physics. Based on the Gluckstern formula, in order to reach to this momentum resolution, it needs to have the spatial resolution better than $100 \mu\text{m}$. However, this formula does not describe the systematic effect such as field distortion.

For a low momentum particle, the resolution is limited by multiple scattering. For instance for ILD TPC for a 1 GeV particle the first term of equation (2.5.36) is about 1.2×10^{-3} and the second term is around $7.59 \times 10^{-5} \cdot p_t$ [GeV]. But for a higher momentum particle the multiple scattering is negligible.

2.6 Software framework

As mentioned before, the ILD has different layers for the different purposes and at the end, all information from all layers are utilized for the analysis. In order to do analysis, simulation, reconstruction, and digitization, a software framework called ILCSoft has been developed which consists of different packages for each layer [41]. In the following, three packages utilized for this thesis will be explained.

2.6.1 LCIO

Linear Collider I/O (LCIO) [42] [43], a persistency framework, has been developed to define a data model for the linear collider physics community. The LCIO consists of different classes. The classes, used for this thesis, are defined as follow:

- **MCParticle** holds the Monte Carlo truth particles generated by the generator or by the simulation program.
- **TrackerRawData** holds the raw tracker data. In this class, the cell ids are used to encode the module number, row and column of the hit.
- **TrackerData** is the same as TrackerRawData but for the data which has been corrected. It contains cell ids and ADC values.
- **TrackerHit** contains three-dimensional space point (hits) and their error matrix (covariance matrix) which are used for pattern recognition.
- **SimTrackerHit** is for storing simulated hits from tracking detectors.
- **Track** contains all hits and reconstructed tracks from the track reconstruction.

As mentioned before, for a TPC with a magnetic field tracks have helicoidal shapes which can be described by five parameters. For charged particles with high energy, the effect of the magnetic field is small and the trajectory of these particles is an almost straight line, therefore, the parameters have to describe straight tracks.

The parameters in LCIO are chosen with respect to the point of closest approach (pca) to a reference point. The selection of the reference point can be arbitrary but normally the origin of the coordinate system is considered as the reference point. More information about the parameters is available in [44] and [37].

Usually, the z-axis is parallel to the magnetic field and the coordinate system is chosen such that the readout plane is in the X-Y plane. The projection of the helix onto the X-Y plane has a circular shape which is described by three parameters as follow (figure (2.12-a)):

- ϕ_0 is the azimuthal angle of the momentum of the particle and the positive direction of the x-axis at pca.
- Ω describes the curvature of the track and it is defined $\Omega = \frac{1}{R}$. The sign of Ω is defined such that it is negative for counter-clockwise motion of the particle in the X-Y plane and it is positive for clockwise motion.
- d_0 is the minimum distance between the reference point and the pca. If the reference point is located inside the circle, d_0 and Ω have the same sign. Otherwise they have opposite sign.

For describing the whole helix in space, two additional parameters are needed. To define these two parameters, the definition of arc length (s) is required. The arc length is the distance of hits to pca along the circle in the X - Y plane. The arc length at pca is zero. In the direction of the charged particle motion, it is positive and in the opposite direction is negative. The projection of a track in S - Z plane is a straight line and it is described by two parameters as follows (figure (2.12-b)):

- $\tan(\lambda)$ is the slope of the straight line in the S - Z plane.
- z_0 is the z position of the track at the pca with respect to the reference point.

With these five parameters one can describe a helix. In the absence of the magnetic field, Ω is zero.

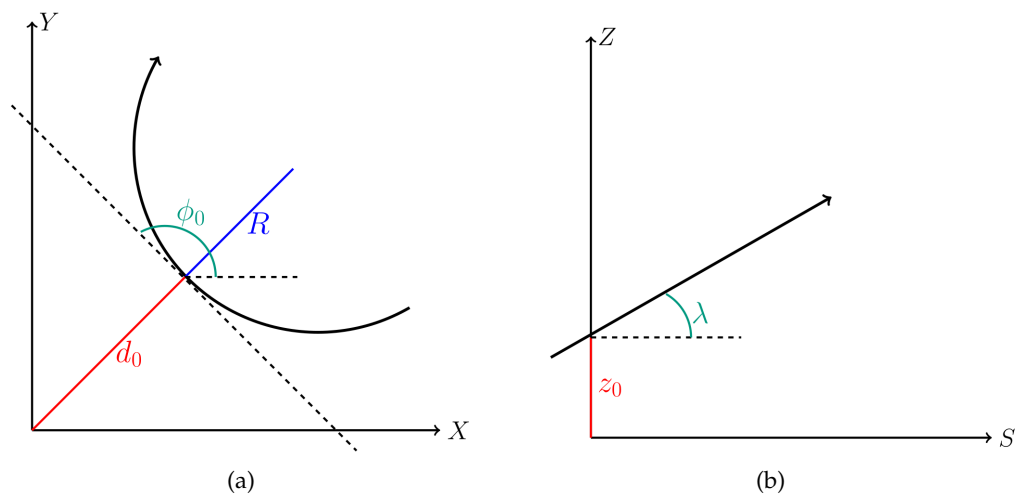


Figure 2.12: Parameters of a helix (a) in the X - Y plane and (b) in the S - Z plane.

2.6.2 GEAR

GEometry API for Reconstruction (GEAR) [45] is a software package used to describe the geometry of the detector during data reconstruction and simulation. The description of the detector is provided via an XML file. In this file, TPC parameters such as the position of each module, the drift length of the TPC, the magnetic field, the type of coordinate, the radius of the TPC (inner and outer radius) and so on, are identified.

2.6.3 MarlinTPC

Modular Analysis and Reconstruction for the LINear collider (Marlin) is a modular C++ software framework for analysis, simulation, and reconstruction based on LCIO. For using Marlin, a user can define and sort processors in an XML file called steering file, and parameters needed by processors. Marlin can read multiple LCIO files and the input and output data are collected in terms of $LCCollections$ in a container called $LCEvent$. Then Marlin calls the processors for every event and they read existing $LCCollections$ and write a new one. In the end, the output can be saved to an LCIO file. Figure (2.13) illustrates the principle of the Marlin [46] [47].

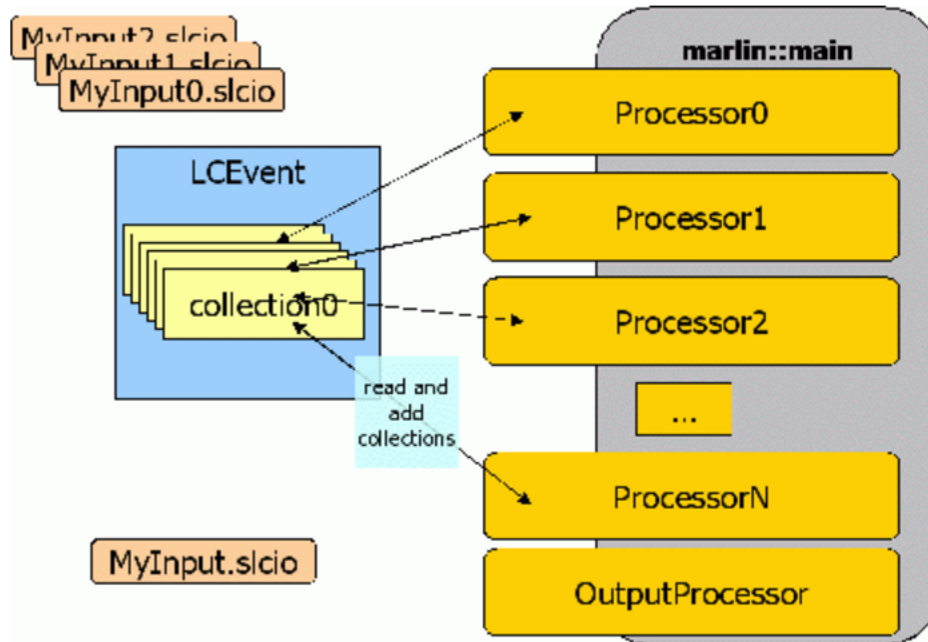


Figure 2.13: Schematic of the principle of how Marlin works [46].

MarlinTPC [48] [49] is a software package based on Marlin which has been developed specifically for a TPC. It consists of many processors for analysis, simulation, reconstruction and digitization for both pad and pixelized readout and also for different gas amplification methods. All algorithms for this thesis are developed in this framework.

2.7 The Timepix chip

Timepix chip [50] [51] is an imaging chip based on the CMOS technology and consists of a 256×256 pixels matrix [52]. Each pixel has the physical dimension $55\mu\text{m} \times 55\mu\text{m}$ and therefore a Timepix chip has $14.08\text{mm} \times 14.08\text{mm}$ active area. The logic of each pixel can be divided into two main parts: the analog side and the digital side. Figure (2.14) shows the architecture of these two parts. The analog side consists of the pixel pad, test pulse input, charge sensitive pre-amplifier and discriminator and the digital side contains the Timepix Synchronisation Logic (TSL), 14-bit shift register and overflow control. More information about all these parts is available [50].

Generally there are four modes for each pixel in which they can be programmed to run. These four modes are (figure (2.15-a))

- **Medipix mode:** counts the sampling clock cycles once, whenever the signal is over the threshold during the shutter time.
- **Time over threshold (TOT) mode:** counts the number of the sampling clock (f_{clock}) cycles as long as the discriminator signal is above the threshold during the shutter time.
- **Time of arrival (TOA) mode:** counts the sampling clock cycles from the first discriminator signal being over the threshold until end of the shutter time.

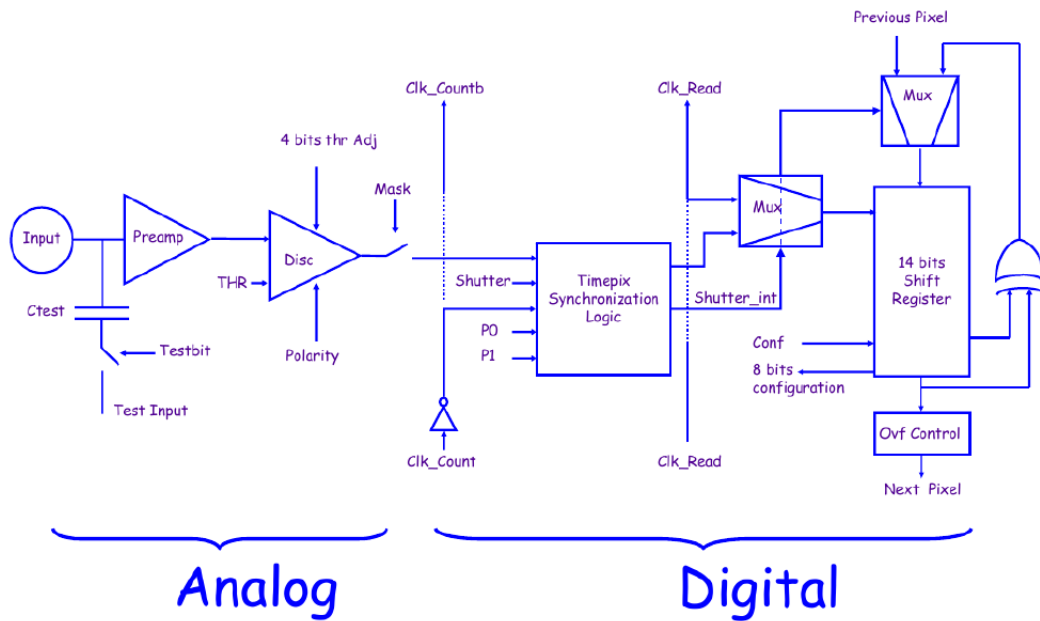


Figure 2.14: Diagram of a pixel for Timepix chip [50].

Based on this mode, the arrival time of charge can be calculated and hence is the candidate mode to reconstruct the drift time in a TPC.

- **1st hit mode:** counts the sample clock cycles only once for whole opening shutter time whenever the signal is over the threshold.

In the TOA mode, there is an effect called *time walk* effect. It happens when the different pulse heights (different amount of charge) are registered at the same time. It causes the measured time to be different. The reason is the rise time of the pre-amplifier in the analog part of the pixel depends on the absolute charge of the signal. From figure (2.15-b) it can be seen that for the higher threshold, this effect increases. This effect can be calibrated by sending test pulses with a fixed delay and slanted pulse shape [53].

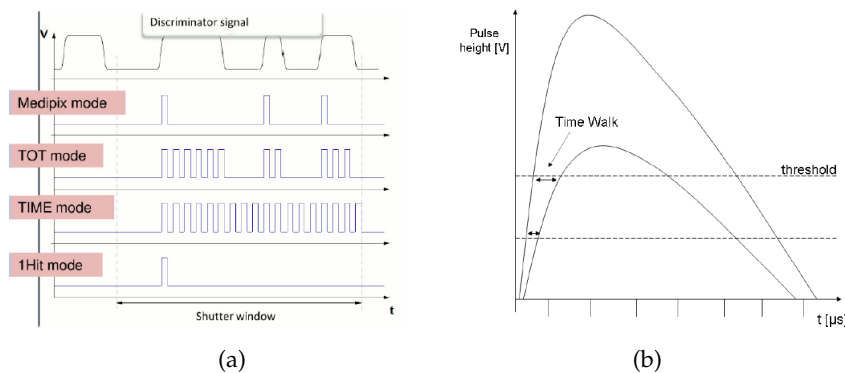


Figure 2.15: (a) Different modes of the operating Timepix chip [54] and (b) time walk effect [53]

2.8 The InGrid chip

An InGrid chip is a combination of a Macromegas and a pixel readout. In order to have a gas amplification, the grid is set to a negative potential with respect to the chip. The granularity of the grid, the size of the holes and the height of the amplification region ($50\mu\text{m}$) causes each pixel to monitor one hole. Hence, when a primary electron goes through a hole the avalanche of it spreads over the pixel underneath of that hole. The signal from the avalanche of charge is strong enough to exceed the threshold of the pixel underneath.

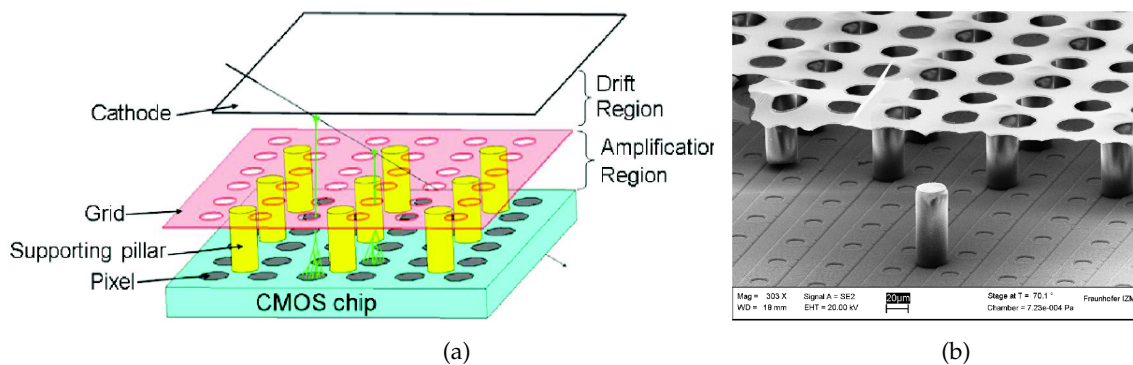


Figure 2.16: (a) Schematic illustration of using InGrid technology in a detector [55] and (b) SEM image of an InGrid prepared by the IZM¹Berlin [56].

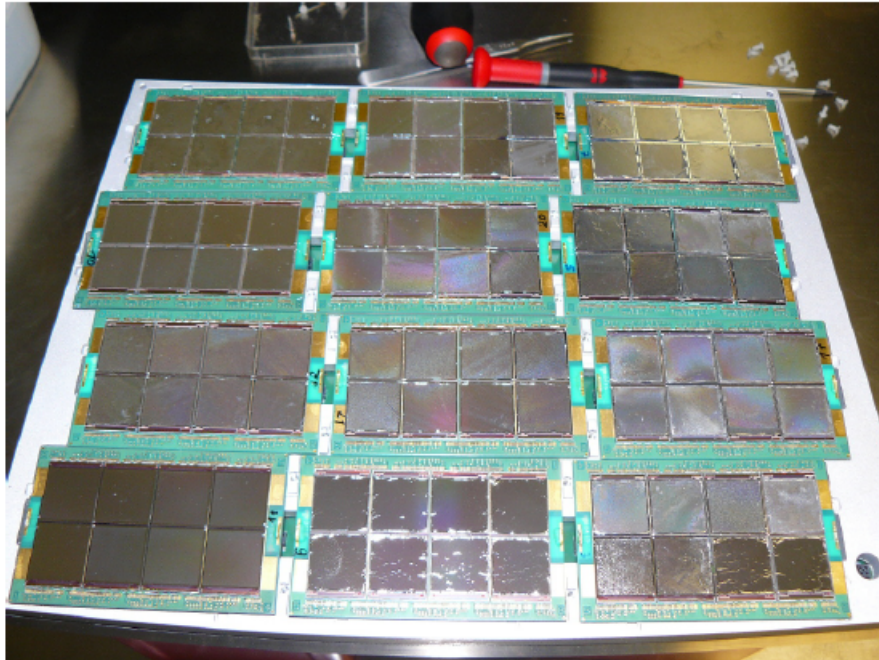
The general method to register hits on the typical readout system is to calculate the center of gravity of the charged cluster shaped after the avalanche from more than one primary electrons passing through the holes of a gas amplifier. This causes the spatial resolution of the detector to decrease due to that fact that this method returns the mean value of the positions of several primary electrons. In addition, it is not possible to resolve delta electrons from the charged cluster.

In contrast, the structure of the InGrid results each primary electron to be visible in exactly one each pixel. Hence, instead of having charged clusters from several primary electrons, there are point hits from each primary electron. It leads not only to have a high spatial resolution but also to register many hits with more precision of the position of the primary electrons. Moreover, the energy loss dE/dx of a particle is directly accessible from counting the hits of the reconstructed track.

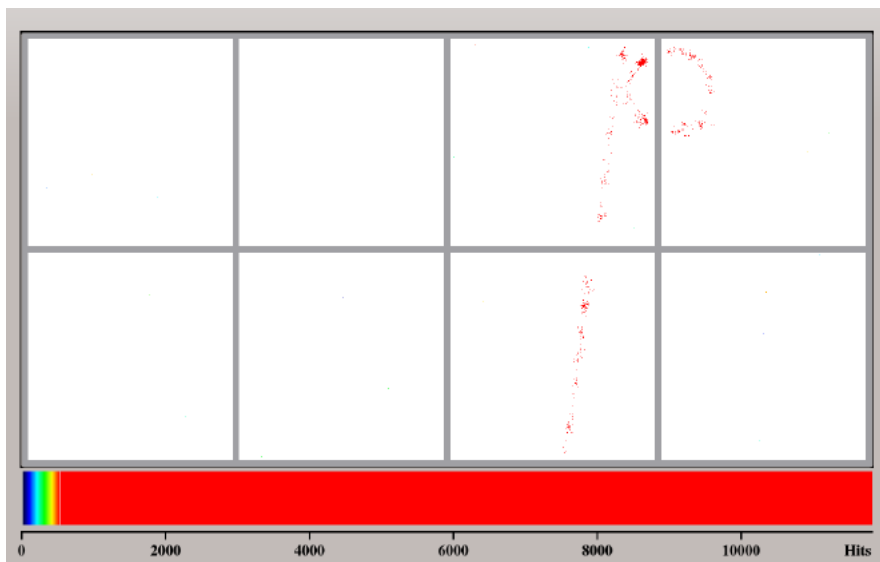
Despite the fact that the property of the InGrid should lead to having a higher double track resolution i.e. separating two tracks from each other, the high amount of hits in addition to the noise in the system and also diffusion in a TPC makes the pattern recognition to become very challenging.

For two experiments having done at the LP TPC at the DESY, every eight InGrid chips were mounted in an unit structure called Octoboard. Figure (2.17-a) shows a picture of 12 Octoboards which prepared for a test beam experiment done on 2015 (see chapter 6) and figure (2.17-b) shows an event display view of an Octoboard during data taking for the same experiment. More information about the history of the InGrid and also the process of producing an InGrid is available in [56].

¹The Fraunhofer IZM in Berlin is the producer of the InGrid.



(a)



(b)

Figure 2.17: (a) 96 InGrid chips arranged on 12 Octoboards [56] and (b) Event display view of an Octoboard during data taking for the test beam experiment done on 2015 at LP TPC, DESY [56].

Chapter 3

Track reconstruction

3.1 Introduction

Track reconstruction is one of the fundamental steps in the data analysis chain of particle physics experiments. The main goal of the track reconstruction is to find the direction, the location, and momentum of charged particles. Generally, track reconstruction consists of three parts: track finding (pattern recognition), track fitting and analysis of the quality of the reconstructed tracks [57]:

- **Track finding (pattern recognition)** is used in order to assign hits to the right tracks.
- **Track fitting** estimates the track parameters based on the assigned hits and depends on the track finding performance.
- **Analysis** is used to check the quality of the performance of the track finding and track fitting.

This definition of the track reconstruction is known as a classical approach. However, with the modern tracking detectors with many hits somehow it is difficult to have a boundary between track finding and track fitting. In the modern approach, there is a pre-estimation the track parameters and consequently, pre-selection of the track in the finding process which can improve the result of the track fitting. Moreover, the final decision is done by a track fitting process [57]. At the end, the performance of track reconstruction has to be tested. This analysis is done based on the data for which the final result or target is identified.

The following sections explain briefly about each of these parts and refer to some reference for whom are interested to read more about each of them. The first section explains the concept of pattern recognition, the second section illustrates what the track fitting is with some example and at the end, the evaluation and qualification of a reconstructed track will be explained.

3.2 Track finding (Pattern recognition)

Pattern recognition is a field, which with applying mathematics, focuses on the recognition of the patterns in a data set for many demanding fields such as astronomy, computer science, High-Energy physics and etc. The aim of pattern recognition is to classify the objects under study and an algorithm that classifies the objects is called *classifier*. For a tracking detector, the objects are hits generated by charged particles and the purpose of pattern recognition is to group the hits into track candidates. This process is called *track finding* [58].

Each object has to be described by a finite number of parameters resulting from measurements. The number of parameters identifies a dimension of a space formed by parameters which are called *pattern space* $\{P\}$. The numerical values of the measurement of an object are grouped in a vector \mathbf{X} of length n called *measurement vector*. The length of a measurement vector is the dimension of the pattern space. For instance, each hit in a TPC detector is identified by 3 values x , y and z , the position of the hit in a Cartesian coordinate system. These values form a vector with $n = 3$ and therefore $\{P\}$ is the 3-dimensional Euclidean space. A pattern space requires that all n components of the measurement vectors already exist for all hits in this space [58].

In the case of tuning an algorithm to calculate efficiency, purity or other output results, a *training sample* is used. Moreover, a training sample helps to find a mathematical description when there is no one, or for convenience if it exists. A training sample is a set of objects which can be anything depending on the field of the study. For instance, in the case of tracking detectors, it is many particle trajectories, however, it can be a single hit or track segments or else [58]. In some cases, it is possible to use a training sample with its corresponding target. All targets for all training samples are grouped in a vector called *target vector*. In such a case, the application of the pattern recognition is known as a *supervised learning* problem. In other words, based on the supervised training sample, supervised learning gives a predictive model for future data without target e.g. real data from experiment [59] [60]. For this reason, it is better to have enough training samples that can be representative of the problem which is under study.

An example for a supervised learning in High-Energy physics is a simulation of a tracking detector. In this case, the Monte Carlo method is used to generate one, two or more particles called MCParticle. These MCParticles traversing the detector have their trajectories. Each object (hit) of these trajectories is identified by the corresponding MCParticle. In this case, an algorithm learns to associate and classify the hits to the right MCParticle trajectory. As mentioned before, the main goal of pattern recognition is to classify a set of objects. For each class, there is a certain criterion and a class is formed by objects that fulfill the criteria of the class. In order to classify the objects, the pattern recognition has to find a decision function such that

$$C = f(\mathbf{X}) \quad (3.2.1)$$

where C is the number of class to which the object described by \mathbf{X} belongs. All C for all objects generate a space called *classification space* $\{C\}$. The decision function divides the input space into regions called *decision regions* which means every object inside these regions is assigned to the class. In addition, *decision boundaries* are defined as boundaries between decision regions. In High-Energy physics, normally classes do not share objects i.e. each track (class) does not have shared hits with other tracks [58] [60].

Sometimes it is easier to work in a space called *feature space* $\{F\}$ in order to reduce computing time. Many parameters in pattern space can transform to the feature space with fewer elements with dimension m [58]:

$$Z = R(\mathbf{X}), \quad Z \in \{F\}, \quad \mathbf{X} \in \{P\} \quad (3.2.2)$$

where R is an arbitrator transformation. It is important to find a transformation in a way that m would be as small as possible.

According to the definition of the different spaces, one can consider that the task of pattern recognition is to find the transformation [58]

$$\{P\} \implies \{C\} \text{ or } \{P\} \implies \{F\} \implies \{C\} \quad (3.2.3)$$

Normally, the hits within a given distance from a reconstructed track are called *inliers* and other hits are called *outliers*. In order to find whether an algorithm can find inliers correctly or not a supervised learning task can be used such as MCTParticle generator while the target set, in this case, inliers and outliers, are already identified. Consequently, the algorithm should work with an unsupervised data set such as a real data from an experiment.

Generally, there are two methods for track finding; *global* and *local* method. For the global method, all objects (hits) enter into the algorithm in the same way. Then the algorithm produces a list of tracks that can be found on the original data set. For a global method, the computing time is proportional to the number of hits [58].

On the contrary, a local method is that one selects one track candidate at a time, typically by selecting a few hits only as a segmentation of the track, and then by interpolation or extrapolation of the current segment, makes a prediction as to find further hits which belong to the track candidate. Normally there is a certain number of tries to collect hits [58].

As examples for each method, it can be mentioned to some algorithms such as Kalman filter [61] [62], the combinational method, the histogram method [58] and Hough transform [63] as the typical algorithm for the global method. Moreover, track following, track roads and track elements are the usual algorithm for local method. For more information about these methods see [58].

For this thesis, due to the fact that there are many hits along a track, a local method for the track finding is used and it is close to the concept of the track elements algorithm. The algorithm tries to find a segment of a track called *tracklet* and then merges all relevant segments or tracklets to each other in order to have a full track. Normally, a particular unit in a TPC is used to define segmentation. For instance, in our experiment, each Octoboard, i.e. a board consisting of eight InGrid chips (figure (2.17)), is used for the segmentation. For each Octoboard the Hough transform and a bivariate normal distribution (BND) method are used to find inliers and consequently tracklets. The Hough transform is one of the typical methods e.g. in image processing and High-Energy physics for finding parameters of a line or curve. Both, the Hough transform and BND, will be explained in detail in chapter 4.

3.3 Track fitting

Generally, track fitting is a technique of using a mathematical method based on the hits found by pattern recognition, in order to have an estimation of the kinematic parameters of a particle such as the momentum vector. A charged particle in a homogeneous magnetic field has a helical motion. But this is not true in a real experiment. Because of the energy loss reducing the momentum of the particle, multiple Coulomb scattering causing random changes in the direction of the flight or inhomogeneous magnetic field, the motion of the charged particle is not completely a helix [64][38].

Although the effect of the multiple scattering and energy loss for a gaseous detector is small in comparison with a solid detector, for a charged particle with a low energy is not completely negligible and it has a tiny effect on the momentum resolution. In contrast, distortions of the magnetic or electric field have an important role in a TPC and cause deviations from the ideal path for a charged particle.

For instance, the distortions of the magnetic field change the curvature of the motion because of a changing magnetic field. For track fitting, there are two general approaches; classical approach and adaptive approach. In the classical approach, the candidate track is passed to a least-squares estimator. Overall, there are three ways to implement an estimator. It can be used as a non-linear regression, as a breakpoint fit, or as a recursive estimator [57].

For instance, one of the very popular recursive estimators in High-Energy physics is Kalman filter. It proceeds in three steps:

- **Prediction** which returns the state vector of the parameters for a track and its covariance matrix propagated to the next state or layer of the detector.
- **Filtering** which updates the state vector of the state or layer based on the measurement on that state.
- **Smoothing** which optimizes the estimation of the track parameters in each layer or state of the detector based on all observations up to that layer.

However, Kalman filter is not robust which means it is sensitive to the outliers and each outlier biases the entire track. Consequently, it is difficult to identify multiple outliers. More information about Kalman filter is available in [58] and [61].

General broken Lines (GBL) [64] is another track fitting method for tracking detectors. It is a fast global track refit and powerful to deal with the multiple scattering. In addition, the GBL is able to calculate the full covariance matrix of all track parameters and hence it can be implemented for track based alignment and calibration of detectors with the global Millepede-II algorithm [64]. For a TPC, although the multiple scattering is almost negligible, there is still an interaction of the particle with the wall of the TPC. In such a case, the GBL can consider this issue. It also can be used to correct parameters such as geometry used for alignment [65].

Another advantage of the GBL is that it can describe the trajectory of a charged particle in an arbitrary magnetic field and material distribution. In comparison with the Kalman filter, the GBL mathematically is equivalent to the Kalman filter but computationally in comparison with Kalman filtering and smoothing is almost three times faster than the Kalman filter. About the GBL and comparing this model with the Kalman filter there is a nice explanation in [64].

In order to have a robust fitting, an adaptive approach is used. In this approach, an adaptive estimator is implemented and it has several advantages. For instance, in this approach, the background is suppressed automatically and hence this reduces the bias due to the outliers. Moreover, if there are several observations in a layer which are compatible with the track candidate, the estimator selects the globally best match.

Typically, in the adaptive approach, both pattern recognition and track fitting work simultaneously but the final decision is done at the fit stage. As some example of this approach, it can be mentioned to Elastic tracking, Elastic arm, and combinatorial Kalman filter. More information and explanation of these methods are available in [57].

For this thesis, the GBL is implemented as the main track fitting algorithm because of more accuracy and reliability. After that, the results of simulation and real data experiment have to be controlled. In the following subsection, it will be explained how this job will be done.

3.4 Analysis

After track reconstruction, the quality of its performance has to be checked. The best source for this propose is to use supervised data such as a data set based on a Monte Carlo generator. In this case, the targets are identified and the quality of reconstructed tracks can be compared with the targets and then see how the algorithm works. One of the important objectives of this study is optimization of the algorithm for different situations such as different drift length, the distance of two tracks, etc.

Generally, there are two methods to check the quality of the reconstructed tracks; Hit matching and Parameters matching [66] [67]. For the first one, every hit of a track is compared with the associated MC particle's hits and for the second one, the parameters and momentum calculated from parameters of the reconstructed track are compared with the associated MC particle's parameters. For this thesis, the Hit matching is used for pattern recognition part. As mentioned before, the main goal of the pattern recognition or track finding is to collect inliers and for this reason, it is the main task to check the performance of the algorithm to see how successful it is to collect the right hits.

Moreover, by definition, the main job of the track fitting is to estimate the parameters of a track based on the assigned hits. In this case, the Parameters matching is utilized in order to see how the track reconstruction chain works.

3.4.1 Hit matching

Each hit in the simulation has information about its original MC Particle. It means according to the simulation it is clear that each hit belongs to a particle or not and if so belongs to which particle. According to the ILCSOFT framework, all generated hits are saved in a file and one can identify the MC particle of a hit in this file. Later this information is accessible for analysis. In addition, it is also possible that some hits are generated by noise in simulation and therefore there is no associated MC particle for them.

For the hit matching method, there are two main subjects considered for this thesis; one the quality of tracks i.e. track efficiency and track purity and one the quality of inliers i.e. hit efficiency and hit purity. But before going further, first of all we need to have some general definition for analysis as follow [66][67]:

- **Correct track:** is a track that is associated with more than $X\%$ (usually $X > 60\%$) of the hits of one MC particle. This track is assigned as a correct track (or found track) to this MC particle.
- **Ghost track:** a track that is not associated with any MC particle. The origin of the hits for a ghost track can be noise or a mixture of two or more tracks.
- **Loss track:** if the algorithm can not find any track for a MC particle then it is counted as a loss track e.g. according to the simulation for an event, it is expected to find two tracks but the algorithm can find only one of them then we have one loss track.

- **Clone track:** if there is more than one associated track to a particle, these extra tracks are counted as a clone track. For simulation clone tracks only exist, if X in the correct track association is chosen to be less than 50%. For real data the value of X is not known for a given particle and therefore clone tracks are common in data.

According to these definitions, the track efficiency and the track purity are defined as follow [67]:

$$\text{Track Efficiency} = \frac{N_{\text{CorrectTrack}}}{N_{\text{MCParticle}}} \quad (3.4.1)$$

and

$$\text{Track Purity} = \frac{N_{\text{CorrectTrack}}}{N_{\text{CorrectTrack}} + N_{\text{Ghost}} + N_{\text{Clone}}} \quad (3.4.2)$$

where $N_{\text{CorrectTrack}}$, $N_{\text{MCParticle}}$, N_{Ghost} , N_{Clone} are the number of correct tracks, particles from MC generator, ghost tracks and clone tracks, respectively. In addition, the loss rate and the loss fraction are determined as:

$$\text{Loss Rate} = \frac{N_{\text{LossTrack}}}{N_{\text{Event}}} \quad (3.4.3)$$

and

$$\text{Loss Fraction} = \frac{N_{\text{LossTrack}}}{N_{\text{MCParticle}}} \quad (3.4.4)$$

where $N_{\text{LossTrack}}$ is the number of particles that are not identified by algorithm. N_{Event} is the number of all events that we have in our simulation. Moreover, the hit efficiency and the hit purity are defined as:

$$\text{Hit Efficiency} = \frac{N_{\text{RightHits}}}{N_{\text{SimHits}}} \quad (3.4.5)$$

and

$$\text{Hit Purity} = \frac{N_{\text{RightHits}}}{N_{\text{RightHits}} + N_{\text{WrongHits}}} \quad (3.4.6)$$

where

- N_{SimHits} : Number of the simulated hits for an MC particle.
- $N_{\text{RightHits}}$: Number of hits on a track from the associated MC particle.
- $N_{\text{WrongHits}}$: Number of hits on a track from noise or other MC particles.

These are general definitions for analysis tools which are implemented in this thesis for evaluating the performance of the track finding algorithm and also for optimization of the free parameters of the code.

3.4.2 Parameter matching

Another method for evaluation of the track reconstruction is parameter matching. In this method, the parameters of a track are compared with reference parameters which could be simulation data or real data. For instance, as mentioned in chapter 2, there are 5 parameters which determine the trajectory of a track in a TPC [44].

For generating a MC particle in a simulation, these parameters are identified and therefore they will be used as the reference between the reconstructed and generated tracks in order to estimate track efficiency and purity. If the parameters agree within certain limits, then the corresponding track is called *correct track*. However, parameter matching suffers from clone tracks. This kind of fake track can be accepted as a correct track.

Further, the parameter matching is the best method for real data e.g. from test beam. For real data, the origin of each hit is not clear, and the only method for controlling the inliers and outliers is using eye which means one has to check a bunch of events by eye and compare what one can recognize as a track (and the inliers) and what the algorithm found and reconstructed. Thereafter, the track efficiency and purity are defined according to equations (3.4.1) and (3.4.2). For such a method, the human mistakes certainly should be taken into account and the result is not completely reliable. In addition, for real data, the reference parameters also depend on the performance of the experiment. If the experiment runs with high accuracy then it is possible to consider the initial setup of the experiment as the reference parameters.

Moreover, if the energy of a particle is known during an experiment, consequentially, the transverse momentum and momentum of the particle can be calculated for the track parameters, which is the main goal of the track reconstruction and therefore the performance of the algorithms can be tested.

Nevertheless, this evaluation strongly depends on the hardware performance during running the experiment. Any misalignment or other defects such as electric or magnetic field distortions could have an influence on the quality of the data and on the result of the track reconstruction. For instance, a magnetic field distortion causes the curve of tracks to have a deviation from what was expected. Thus this issue has a negative effect on the calculation of the momentum. If all of the defects are small, one can take them into account as the systematic error otherwise the result is not trusty to test and control the performance of the algorithms.

As a conclusion of this chapter, it was mentioned that the best method for the case that there are many hits along a track is to use a local method. After that, the GBL is the main track fitting method for this thesis because it is fast and reliable. In the analysis chapter, some of these methods explained in this chapter will be used for optimization of the main code for pattern recognition and analysis the simulation and real data.

Chapter 4

Track finding for InGrid chips

4.1 Introduction

In the previous chapters, it was mentioned that for the readout system based on the InGrid chip for a TPC, there are many hits along a track (see chapter 2). This causes the assigning of hits to the correct track to be difficult for pattern recognition. Concurrently, the diffusion effect in the TPC increases this difficulty. Furthermore, the general definition of the track reconstruction and different methods were introduced and it was mentioned which one is the preference for our case (see chapter 3).

This chapter explains the algorithms and methods which are used in this thesis for the track reconstruction, first for one Octoboard and then for many Octoboards. Each Octoboard consists of eight InGrid chips (see chapter 2) and it is considered as a unit of the segmentation of a track called tracklet.

For the case that there is only one Octoboard, the tracklets are assigned as tracks. Albeit, when there are more than one Octoboard there is a merging process which examines all tracklets in order to connect the relevant tracklets to have a full track. At the end, a fitting process method is implemented for the full track. For this thesis, the General broken lines algorithm (GBL) [68] is utilized as the track fitting processor.

The two following sections first introduce the Hough transform and bivariate normal distribution (BND) and then how to initialize and fit a BND in a Hough space. After that in section 4, it is explained how to collect inliers. Section 5 introduces the Karimaki [69] and straight line fit; and the calculation of tracklet's parameters. The merging process for many Octoboards is illustrated in section 6. And the last section is about how to recollect the missed inliers along a track after the fitting process.

4.2 Hough Transform

The Hough transform [63] is one of the typical methods which is used in image processing, computer vision and also in High-Energy physics to detect lines, circle or other parametric curves consisting of many points or hits in an image space based on a voting process. The Hough transform can be considered as a kind of the transform from the pattern space (here image space consisting of hits) with the equation of a straight line or curve to the feature space called Hough space or parameter space (see chapter 3). The voting process is a procedure that finds a local maximum peak in a histogram or accumulator presenting parameter space. This local maximum specifies the best parameters for the fit.

The Hough transform was invented by Paul Hough in 1959, implemented for Bubble chambers, and later in 1962 was patented. Figure (4.1) shows the Bubble chamber and also tracks and their Hough transformation [63].

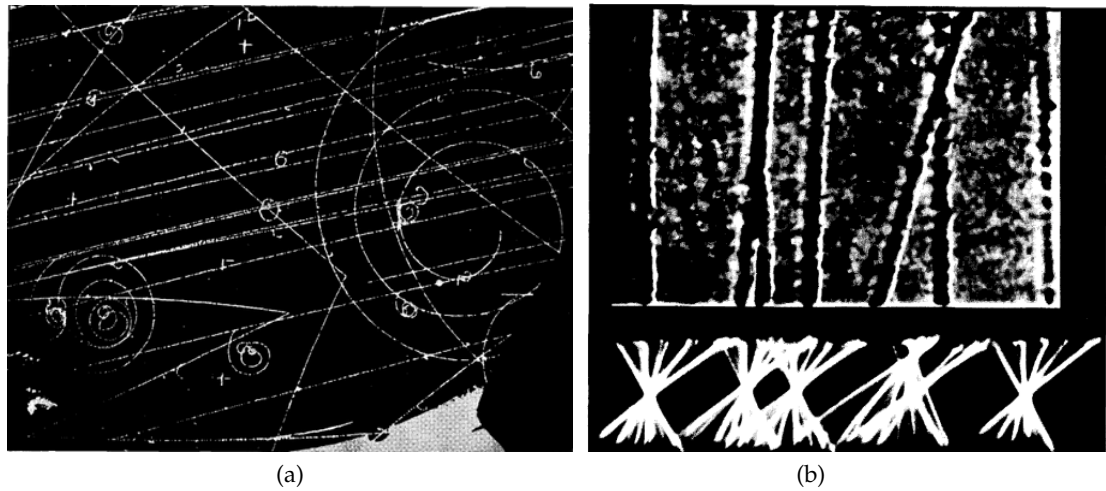


Figure 4.1: (a) Bubble Chamber with many trajectories of particles (b) Upper part shows all tracks that should be found and lower part shows the Hough transformation of them. These pictures are taken from [63].

The original form of transformation is based on the slope-intercept parametrization. In such a case, a straight track $y = mx + n$ can be indicated as a point (m,n) in a Hough space. Each point (x_i, y_i) on the track is transformed into a straight line, where the Hough space is represented by the a - b plane (figure (4.2)):

$$b = y_i - ax_i \quad (4.2.1)$$

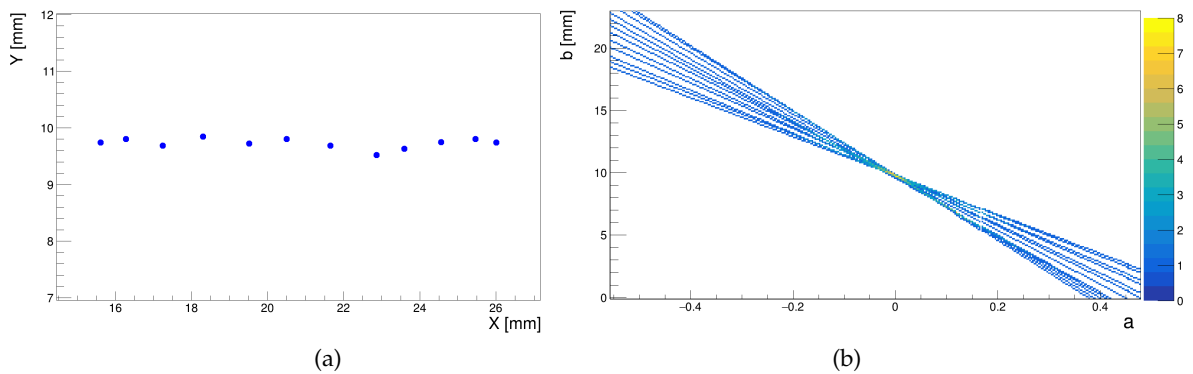


Figure 4.2: (a) an example of a track in the image space (X-Y plane) and (b) the Hough space using the straight line form for the same hits in the a - b plane.

For those points (x_i, y_i) that belong to the same track, their generated lines intersect each other in the point (m,n) in the Hough space. This point specifies the slope and intercept of the candidate straight line for the track [13]. However, all points along a track do not lie exactly on a straight line. Consequently, the intersection of the lines in the Hough space is not point-like. A Hough space can be represented by a histogram i.e. a graphical display of the distribution of numerical data, with the dimension based on the number of parameters. For each point (x_i, y_i) the algorithm increments all bins in the histogram that equation (4.2.1) passes through. Finally, the

voting process finds the bin with maximum entries and this bin presents the parameters of the track.

The main problem of this original method is that the equation (4.2.1) is not able to represent vertical lines. In this case, the slope becomes infinite and there is no point in Hough space for the infinite slope. One solution is to have two Hough spaces based on two different equations; one for tracks with an angle of more than 45° and one for less than 45° .

In 1972, Richard Duda and Peter Hart solved this problem by using the Hesse normal form [70]

$$\rho = x_i \cos(\phi) + y_i \sin(\phi) \quad (4.2.2)$$

This equation is the normal equation of the line based on ρ and ϕ which are the normal parameters of the straight line. For the normal equation (4.2.2), ρ is the minimum distance of the origin of the coordinate system to the line. The corresponding point on the line is called **point of closest approach (pca)**, in the image space. In addition, ϕ is the angle between the line from the origin of the coordinate system to pca and the x-axis. Figure (4.3) shows an example of a track with few hits in image space and the relevant Hough space.

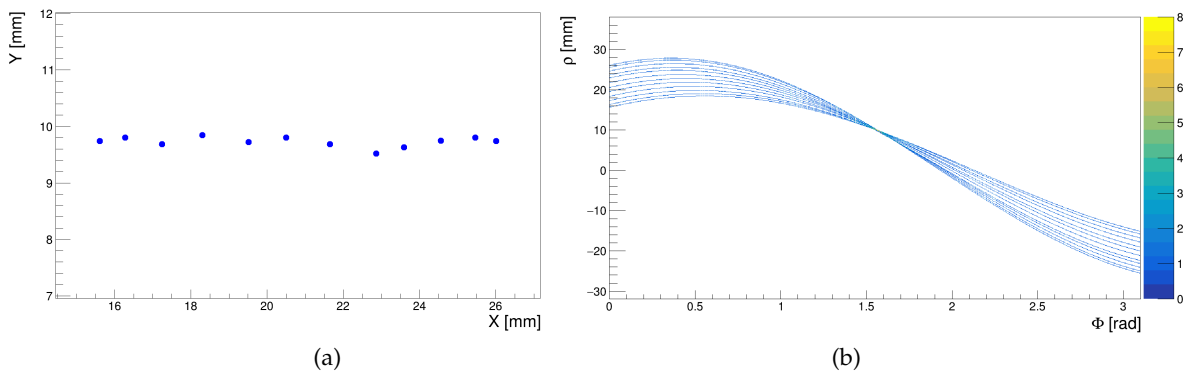


Figure 4.3: (a) an example of a track in the image space (X-Y plane) and (b) the Hough space using the Hesse normal form for the same hits in the ρ - ϕ plane.

Later we will use equation (4.2.2) in the S-Z plane in order to find two other parameters of a track. Figure (4.4) illustrates ρ , ϕ , ϕ_0 and pca in the X-Y plane. As explained chapter 2, $\phi_0 = \phi - \frac{\pi}{2}$ is the angle of momentum of the particle at the pca and the positive x-axis.

According to equation (4.2.2), every point in the image space corresponds to a sinusoidal shaped line in the ρ - ϕ plane. For each Octoboard the origin of the coordinate system is chosen on the left bottom corner of the Octoboard (see figure (2.17)). This leads to restrictions for ϕ in an interval $[0, \pi]$, and for ρ in $[-R, R]$ where $R = \sqrt{w^2 + h^2}$ which is about 80 mm. w and h are the width and height of the Octoboard, respectively.

In the case of using the local finding method, due to the fact that we use an Octoboard as a segment of a track, and because of the size of the Octoboard ($45 \times 65 \text{ mm}^2$), it is assumed that the tracklet is a straight line even with a magnetic field. Nevertheless, this assumption is not completely true, particularly, for a low momentum particles with the energy in the range of some MeV.

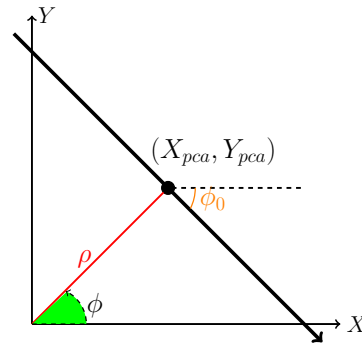


Figure 4.4: This figure shows an example of a track which intersects both the x and the y axes. ρ is the minimum distance from the origin of the coordinate system to the track, ϕ is the angle between the line from the origin of the coordinate system to pca and the x-axis. In addition, ϕ_0 is the angle of momentum of the particle at the pca. (X_{pca}, Y_{pca}) is the point of closest approach (pca) in the X-Y plane.

We explained before that we need to find 4 or 5 parameters (depending on a magnetic field) for a particle trajectory in order to reconstruct the track and to be able to calculate the momentum of the particle in three-dimensional space. For this case, it is important to find inliers in 3D space and be able to separate two tracks not only in the X-Y plane but also in the Z direction. For this reason, first it is tried to find inliers in the X-Y plane and then select inliers in S-Z plane. S is defined as the arc length in the XY-Plane, and in the case of $B=0$ T (or straight tracks), is the shortest distance between a hit and the point of closest approach (pca). Hence, we have two Hough transforms; one in the X-Y plane and one in the S-Z plane. The disadvantage of this method is that normally the Hough transform is slow. But the advantage is the separation of two or more tracks in 3D space is more robust with respect to the outliers.

As described before, the Hough transform is utilized to find inliers in an Octo-board. It was also mentioned that in a TPC the diffusion effect is one of the important issues that should be considered in pattern recognition. The diffusion causes the width of a track to increase and thus the size of the bins of the Hough space also would be an important issue. For instance, for a short drift length, the width of a charge cloud is small and therefore the track looks like a thin line.

Assume that there are two particle trajectories with the low drift length and we can see their separation by eyes. In case that the size of a bin would be too big then there is a probability to merge two tracks in the Hough space. In other words, theoretically, most lines for hits belonging to a track have to pass through a bin which returns the parameters of the track. If the size of the bin would be larger than some distances between the two tracks then most lines of two tracks pass through the same bins and therefore separation of them would be impossible. However, with the right size of the bin, there is still some limitation to separate two tracks especially for the case that one can not see two track even by eyes.

In contrast, for a long drift length, a charge cloud has a large width and if the bin's size would be too small then the algorithm could find two or more tracks for the same particle. In this case, the number of clone tracks increases. Hence, the best solution is to have a flexible bin size for the Hough transform based on the drift length. Otherwise there is a possibility to find two or more tracks for one particle with long drift length.

The strategy which is implemented in this thesis is to set up the width of bins for the ρ -axis based on the transverse and longitudinal spatial resolution in both the X-Y and the S-Z plane. For an InGrid transverse and longitudinal spatial resolution are defined:

$$\sigma_{xy} = \sqrt{\sigma_{0,xy}^2 + \sigma_T^2} \quad (4.2.3)$$

$$\sigma_z = \sqrt{\sigma_{0,z}^2 + \sigma_L^2} \quad (4.2.4)$$

where $\sigma_{0,xy}$ and $\sigma_{0,z}$ are the intrinsic transverse and longitudinal resolution of the In-Grid, and σ_T and σ_L are transverse and longitudinal resolution, the variance of the Gaussian distribution of hits in X, Y and Z direction which are calculated according to equation (2.5.22), respectively. In equation (4.2.3), the intrinsic transverse resolution $\sigma_{0,xy}$ is $55\mu\text{m}/\sqrt{12} = 15.9\mu\text{m}$. In addition, the intrinsic longitudinal resolution $\sigma_{0,z}$ in equation (4.2.4) is calculated based on the intrinsic timing resolution $\sigma_{0,t}$ and drift velocity as follow:

$$\sigma_{0z} = \nu_d \sigma_{0,t} = \nu_d \sqrt{\frac{2T_c^2}{12}} \quad (4.2.5)$$

where $T_c = 1/f_c$ is the clock period of the chip at which operated. The signal from the shutter and the hit are synchronized to an internal clock in every pixel [51]. For this reason, the error on the time measurement can be up to two clock cycles and thus the factor two is added to the last term of equation (4.2.5) under the square root.

This method is done automatically by the algorithm. First of all the algorithm calculates the transverse and longitudinal spatial resolution of all hits as an average for each Octoboard and then the size of bins is defined based on this calculation. In the X-Y plane the width of bins are set to $1 \sigma_{xy}$ and in the S-Z plane are equivalent to full width at half maximum (FWHM $\approx 2.355 \sigma_z$) of the longitudinal diffusion due to the bigger width of the track in the Z direction. In addition, the width of each bin for the ϕ -axis is one degree and it is fixed.

4.3 Bivariate normal distribution (BND)

As the general definition in statistics, *Multivariate normal distribution* is defined in D-dimensional vector \mathbf{x} as [59]:

$$G(\mathbf{x}|\boldsymbol{\mu}, \boldsymbol{\Sigma}) = \frac{1}{(2\pi)^{D/2}} \frac{1}{|\boldsymbol{\Sigma}|^{1/2}} \exp \left[\frac{-1}{2} (\mathbf{x} - \boldsymbol{\mu})^T \boldsymbol{\Sigma}^{-1} (\mathbf{x} - \boldsymbol{\mu}) \right] \quad (4.3.1)$$

where $\boldsymbol{\mu}$ is the mean vector and $\boldsymbol{\Sigma}$ is the DxD-dimensional covariance matrix. In general terms, for a D-dimensional Multivariate normal distribution there are $D(D+1)/2$ independent parameters for $\boldsymbol{\Sigma}$. Meanwhile, there are also D independent parameters in $\boldsymbol{\mu}$ which leads to having $D(D+3)/2$ parameters in total [59].

Bivariate normal distribution (BND) is the 2-dimensional case for multivariate normal distribution. Figure (4.5) shows an example of a bivariate normal distribution. Previously mentioned to this point that the size of bins in the Hough space of the X-Y and S-Z plane is defined as the $1 \sigma_{xy}$ and about $2.3 \sigma_z$, respectively. Because of the diffusion and based on these sizes of the bins some lines could not pass through the bin with maximum entries.

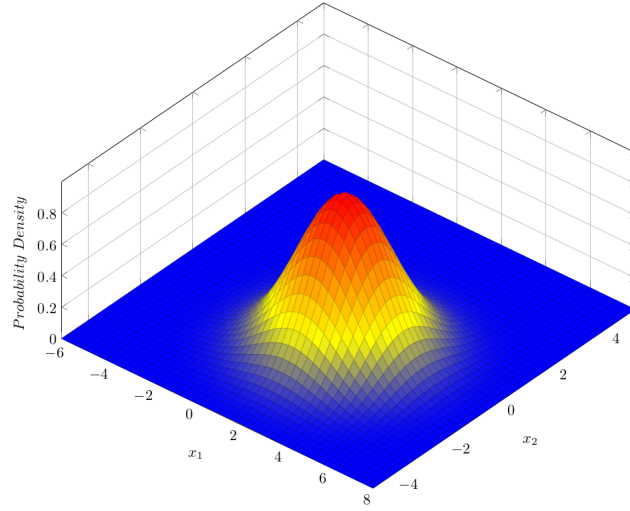


Figure 4.5: Bivariate normal distribution which is a 2-dimensional multivariate normal distribution

For this reason, in order to collect more inliers, the resolution of the track in the Hough space is calculated, and it is used as an initialization of the fit. Then by using a bivariate normal distribution fit around the bin with maximum entries the inliers are collected directly in the Hough space [71].

In other words, with a BND fit the decision regions are defined in the Hough space. For defining decision boundaries, an ellipse corresponding to the $\frac{1}{e}$ of the peak of the BND fit is used (see chapter 3).

The original idea of this method is from *Kernel-based Hough transform* (KHT) [71] developed for image processing. But the main difference between KHT method used in [71] and the implementation of a BND here is that in the image processing by applying some preprocessors the clustering, i.e. is a kind of unsupervised learning algorithm in machine learning, is done and then by using a BND according to the uncertainty associated with the best-fitting line for each cluster, the result of the voting is improved. However, in the case of InGrid chips with many hits, the main issue is the classification and finding inliers. Here the track finding is equivalent to the clustering in the image processing.

Generally, a bivariate normal distribution shows the distribution of two parameters which could have a correlation such as what we have for ϕ and ρ in the Hough space. The general equation for the bivariate normal distribution is

$$G(\phi, \rho) = \frac{1}{2\pi\sigma_\rho\sigma_\phi\sqrt{1-r^2}} \exp\left(-\frac{c}{2(1-r^2)}\right) \quad (4.3.2)$$

where

$$c \equiv \frac{(\phi - \mu_\phi)^2}{\sigma_\phi^2} - \frac{2r(\phi - \mu_\phi)(\rho - \mu_\rho)}{\sigma_\phi\sigma_\rho} + \frac{(\rho - \mu_\rho)^2}{\sigma_\rho^2} \quad (4.3.3)$$

and μ_ϕ and μ_ρ are the mean values for ϕ and ρ , respectively. The correlation between ϕ and ρ is define as:

$$r \equiv \frac{\sigma_{\rho\phi}}{\sigma_\rho\sigma_\phi} \quad (4.3.4)$$

where $\sigma_{\rho\phi}$ is the covariance between these two parameters.

The bivariate normal distribution has an elliptical shape. In case there is a correlation between the ϕ and ρ , this ellipse has a tilt to the x-axis otherwise it would be a vertical or horizontal ellipse depending on the semi-minor and semi-major axes. In equation (4.3.2), the term before the exponential part is the normalization factor [72].

Fitting the BND in the Hough space is done by using ROOT [73] around the bin with the maximum entries which is only local fitting in the histogram [74]. For fitting, first of all the mean values and covariance matrix have to be initialized. For initialization, the corresponding ϕ and ρ for the bin with maximum entries are implemented as the initial value for mean values. On the other hand, the initial value for covariance matrix has to be calculated based on the diffusion effect. The expected longitudinal and Transverse spatial resolution are calculated based on the average of the Z position of all hits in each Octoboard. Figure (4.6) shows an example of a BND fit around the bin with maximum entries in the Hough space.

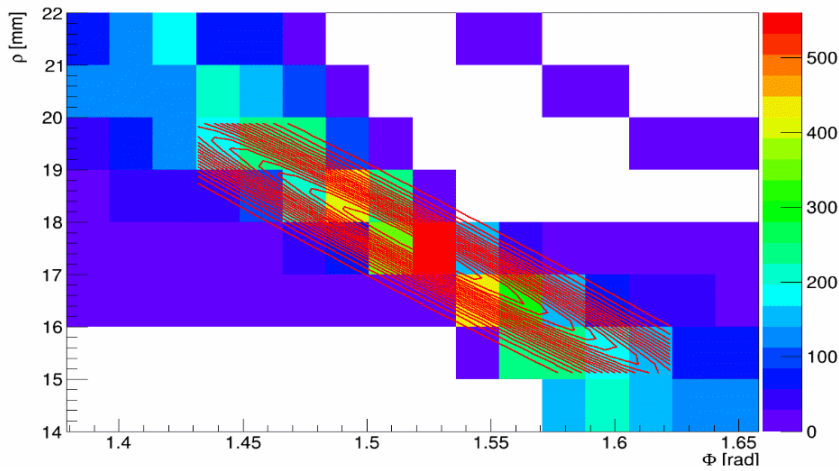


Figure 4.6: Iso-contour of the bivariate normal distribution fit in the Hough space

One issue that can happen for the local fitting is for some events the mean value for ϕ or ρ from the fit becomes infinity. In order to solve this problem, a limitation on parameters for fitting is considered. In this case, it is also avoided to bias the fit with fixing parameters. This limitation is in the range of one standard deviation of ϕ and ρ according to the calculation in the Hough space. Due to the fact that the local fit in the histogram is used, the fit range is also considered as a factor of σ_ρ and σ_ϕ in both the X-Y and the S-Z plane. These factors are free parameters in the code. According to the many simulations, the correlation between these factors for two planes is negligible. Therefore, for optimization, they are considered as two independent parameters.

In chapter 5, the result of the optimization of these two factors for different drift length will be shown. Moreover, because of the limitation for fitting for ϕ and ρ , the changes in the fitting ranges have an effect on the mean value of them and the new mean values from the fit's result later will be used for the calculation of the ellipse utilized for collecting the inliers.

4.3.1 Covariance matrix in the X-Y plane

As previously explained, the normal equation is used for the Hough transform. For the first step the track parameters in 2D (only in the X-Y plane) are calculated. In this case, the covariance matrix in the image space (or hits space) is based on the transverse spatial resolution and it is written:

$$C = \begin{bmatrix} \sigma_{xy}^2 & 0 \\ 0 & \sigma_{xy}^2 \end{bmatrix} \quad (4.3.5)$$

The next step is to calculate the covariance matrix in Hough space. For this calculation, first-order error propagation is used:

$$\begin{bmatrix} \sigma_\rho^2 & \sigma_{\rho\phi} \\ \sigma_{\rho\phi} & \sigma_\phi^2 \end{bmatrix} = \mathbf{J} \begin{bmatrix} \sigma_{xy}^2 & 0 \\ 0 & \sigma_{xy}^2 \end{bmatrix} \mathbf{J}^T \quad (4.3.6)$$

where $\sigma_{\rho\phi}$, σ_ρ and σ_ϕ are covariance and variance of ρ and ϕ in the Hough Space, respectively. In addition, \mathbf{J} is the Jacobian matrix of equation (4.2.2) [75]:

$$\mathbf{J} = \begin{bmatrix} \frac{\partial \rho}{\partial x} & \frac{\partial \rho}{\partial y} \\ \frac{\partial \phi}{\partial x} & \frac{\partial \phi}{\partial y} \end{bmatrix} \quad (4.3.7)$$

4.3.2 Covariance matrix in the S-Z plane

In order to separate two tracks or better say to find inliers in the z direction, the Hough transform is also implemented in the S-Z plane. The arc length is [13]

$$S = \pm \sqrt{(x_{hit} - x_{pca})^2 + (y_{hit} - y_{pca})^2} \quad (4.3.8)$$

where according to equation (4.2.2) and the value of ρ and ϕ_0 from the BND fit in the X-Y plane

$$\begin{aligned} x_{pca} &= -\rho \sin(\phi_0) \\ y_{pca} &= \rho \cos(\phi_0) \end{aligned} \quad (4.3.9)$$

In equation (4.3.8) the negative sign of S is for the case that the hit lies on the part of the trajectory of the particle before it reaches the pca point and the positive sign is for the reverse condition. For calculating σ_S , first-order error propagation is used based on equation (4.3.8):

$$\sigma_S^2 = \left(\frac{\partial S}{\partial x}\right)^2 \sigma_{xy}^2 + \left(\frac{\partial S}{\partial y}\right)^2 \sigma_{xy}^2 \quad (4.3.10)$$

According to equations (4.3.10) and (2.5.22) the covariance matrix in the S-Z plane is defined as follows:

$$C = \begin{bmatrix} \sigma_S^2 & 0 \\ 0 & \sigma_z^2 \end{bmatrix} \quad (4.3.11)$$

For the Hough transform in the S-Z plane the following equation is used

$$\rho_z = S_i \cos(\theta) + z_i \sin(\theta) \quad (4.3.12)$$

and therefore

$$\begin{bmatrix} \sigma_{\rho_z}^2 & \sigma_{\rho_z\theta} \\ \sigma_{\rho_z\theta} & \sigma_\theta^2 \end{bmatrix} = \mathbf{J} \begin{bmatrix} \sigma_S^2 & 0 \\ 0 & \sigma_z^2 \end{bmatrix} \mathbf{J}^T \quad (4.3.13)$$

with \mathbf{J} is, as before, the Jacobian matrix [75]:

$$\mathbf{J} = \begin{bmatrix} \frac{\partial \rho_z}{\partial S} & \frac{\partial \rho_z}{\partial z} \\ \frac{\partial \theta}{\partial S} & \frac{\partial \theta}{\partial z} \end{bmatrix} \quad (4.3.14)$$

4.4 Ellipse equation and semi-major and semi-minor axes

The iso-contours of equation (4.3.2) have an elliptical shape. To find the semi-minor and semi-major axes for the first step, it is considered one level of iso-contours consisting of all points where $G(\phi, \rho) = t$ which $t \in \mathbf{R}$. From equation (4.3.2) there is:

$$t = \frac{1}{2\pi\sigma_\rho\sigma_\phi\sqrt{1-r^2}} \exp\left[-\frac{c}{2(1-r^2)}\right] \quad (4.4.1)$$

$$2\pi\sigma_\rho\sigma_\phi t \sqrt{1-r^2} = \exp\left[-\frac{c}{2(1-r^2)}\right]$$

$$k = 2\pi\sigma_\rho\sigma_\phi\sqrt{1-r^2}$$

then

$$\ln(kt) = -\frac{c}{2(1-r^2)}$$

$$\ln\left(\frac{1}{kt}\right) = \frac{c}{2(1-r^2)}$$

$$1 = \frac{c}{2(1-r^2) \ln\left(\frac{1}{kt}\right)}$$

For simplicity, it is assumed that

$$q = 2(1-r^2) \ln\left(\frac{1}{kt}\right) \quad (4.4.2)$$

and then by using equation (4.3.3)

$$1 = \frac{(\phi - \mu_\phi)^2}{q\sigma_\phi^2} + \frac{(\rho - \mu_\rho)^2}{q\sigma_\rho^2} - \frac{2r(\phi - \mu_\phi)(\rho - \mu_\rho)}{q\sigma_\phi\sigma_\rho} \quad (4.4.3)$$

In case that there is no correlation, the third term in equation (4.4.3) vanishes and this equation would be a horizontal or vertical ellipse equation. Therefore calculating semi-major and semi-minor axes is straight forward. However, because of correlation, the semi-major and semi-minor axes will be changed.

Before continuing with equation (4.4.3), one should find out how to calculate semi-minor and semi-major axes for an ellipse when there is a rotation. Figure (4.7) shows a rotated ellipse with a and b as the semi-major and semi-minor axes, respectively, which is α degree rotated with respect to the x-axis. In a general sense, an ellipse equation is given by $Ax^2 + Bxy + Cy^2 = 1$. Without any rotation it can be written as:

$$\frac{x^2}{a^2} + \frac{y^2}{b^2} = 1 \quad (4.4.4)$$

With a α degree rotation with respect to the x-axis then the ellipse equation is calculated as [76] :

$$\frac{x'^2}{a^2} + \frac{y'^2}{b^2} = 1$$

with

$$\begin{bmatrix} x' \\ y' \end{bmatrix} = \begin{bmatrix} \cos(\alpha) & -\sin(\alpha) \\ \sin(\alpha) & \cos(\alpha) \end{bmatrix} \begin{bmatrix} x \\ y \end{bmatrix}$$

and

$$\begin{aligned} x' &= x \cos(\alpha) - y \sin(\alpha) \\ y' &= x \sin(\alpha) + y \cos(\alpha) \end{aligned}$$

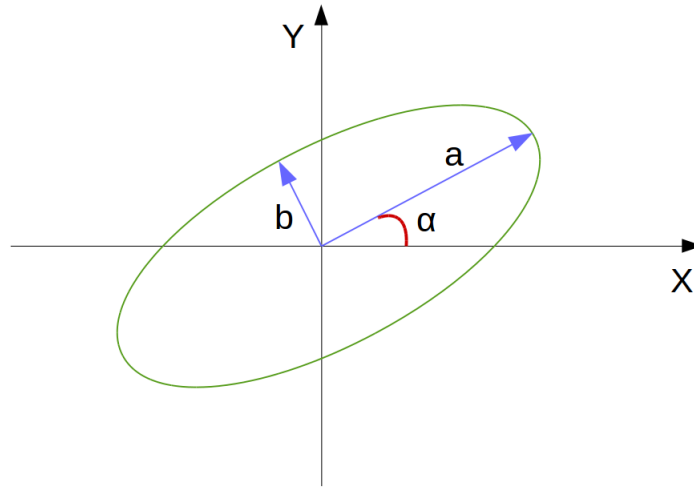


Figure 4.7: The rotated ellipse with α degree with respect to the x-axis, a semi-major and b semi-minor axes.

After substituting x' and y' in equation (4.4.4) and expanding each terms then:

$$1 = \left(\frac{\cos^2(\alpha)}{a^2} + \frac{\sin^2(\alpha)}{b^2} \right) x^2 - 2 \cos(\alpha) \sin(\alpha) \left(\frac{1}{a^2} - \frac{1}{b^2} \right) xy + \left(\frac{\sin^2(\alpha)}{a^2} + \frac{\cos^2(\alpha)}{b^2} \right) y^2 \quad (4.4.5)$$

According to the general equation of an ellipse then A, B and C are

$$\begin{aligned} A &= \frac{\cos^2(\alpha)}{a^2} + \frac{\sin^2(\alpha)}{b^2} \\ B &= -2 \cos(\alpha) \sin(\alpha) \left(\frac{1}{a^2} - \frac{1}{b^2} \right) \\ C &= \frac{\sin^2(\alpha)}{a^2} + \frac{\cos^2(\alpha)}{b^2} \end{aligned} \quad (4.4.6)$$

and

$$\cot(2\alpha) = \frac{C - A}{B} \quad (4.4.7)$$

According to equations (4.4.1) and (4.4.2), one can calculate semi-major and semi-minor axes of the ellipse equation when there is a rotation (due to the correlation) based on the σ_ϕ and σ_ρ . In this case,

$$\begin{aligned} A &= \frac{1}{q\sigma_\phi} \\ C &= \frac{1}{q\sigma_\rho} \\ B &= \frac{-2r}{q\sigma_\phi\sigma_\rho} \end{aligned} \tag{4.4.8}$$

Comparing equations (4.4.6) and (4.4.8) one can find a^2 and b^2

$$\begin{aligned} \frac{1}{q\sigma_\phi^2} &= \frac{\cos^2(\alpha)}{a^2} + \frac{\sin^2(\alpha)}{b^2} \\ \frac{1}{q\sigma_\rho^2} &= \frac{\sin^2(\alpha)}{a^2} + \frac{\cos^2(\alpha)}{b^2} \end{aligned} \tag{4.4.9}$$

$$\frac{2r}{q\sigma_\phi\sigma_\rho} = -2\cos(\alpha)\sin(\alpha)\left(\frac{1}{a^2} - \frac{1}{b^2}\right)$$

therefore:

$$\begin{aligned} a^2 &= \frac{q\sigma_\phi^2\sigma_\rho^2\cos(2\alpha)}{\sigma_\rho^2\cos^2(\alpha) - \sigma_\phi^2\sin^2(\alpha)} \\ b^2 &= \frac{-q\sigma_\phi^2\sigma_\rho^2\cos(2\alpha)}{\sigma_\rho^2\sin^2(\alpha) - \sigma_\phi^2\cos^2(\alpha)} \end{aligned} \tag{4.4.10}$$

For the case of $\frac{1}{e}$ of the peak of the bivariate normal distribution corresponding to the one σ , the q from equations (4.4.1) and (4.4.2) is calculated:

$$t = \frac{1}{e} \left(\frac{1}{2\pi\sigma_\rho\sigma_\phi\sqrt{1-r^2}} \right) \tag{4.4.11}$$

$$q = 2(1 - r^2)$$

In order to find the semi-minor and semi-major axes of the ellipse that corresponds to one σ of the BND, one has to take the ellipse that corresponds to the $\frac{1}{e}$ of the peak value of the BND. This ellipse identifies the decision boundary in the Hough space and all hits that their line in the Hough space passes through this ellipse are collected as an *inlier*. Figure (4.8) shows the ellipse corresponding to the one σ of the fit. The important point of this method is that one can tune a free parameter with which both axes can be scaled. This means the number of inliers can be changed. In the code, there are two free parameters considered as scale factors; one for the X-Y plane and one for the S-Z plane.

Based on the many simulations and experiences, these two scale factors as well as the factors for the range of fitting, are independent. In chapter 5, the result of the optimization of these factors for different drift lengths and also for the case that there are two tracks for an Octoboard will be presented.

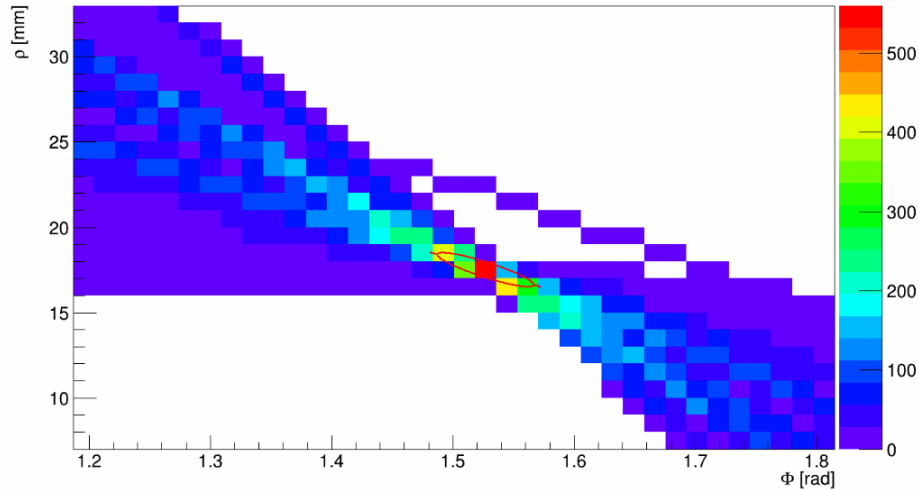


Figure 4.8: The ellipse corresponding to $1/e$ of the peak of Bivariate normal distribution.

4.5 Tracklet Parameters

It was mentioned before that in the modern track finding method, an algorithm must have a rough calculation of track parameters and therefore it must rely on a method to estimate the curve of the found tracks when there is a magnetic field. Thus, for each tracklet, there are 4 or 5 parameters depending on a magnetic field that must be identified. According to the LCIO format, these parameters are ϕ , d_0 and $\Omega = \pm \frac{1}{R}$ in the X-Y plane and z_0 and $\tan(\lambda)$ in the S-Z plane [44].

In the following subsections, it will be illustrated in detail how to find them in both the X-Y and the S-Z plane with and without magnetic field [67]. For all calculations in the following subsections, it is considered that the reference point of each tracklet is at the middle point of the tracklet in the X-Y plane. In other words, the reference point for each tracklet is defined as $r = (\langle x \rangle, \langle y \rangle, 0)$. Later this reference point will have an important role for merging relevant tracklets.

4.5.1 The X-Y plane parameters

In order to measure a particle momentum, a TPC is usually placed in an almost uniform magnetic field. Consequently, a particle's trajectory forms a circular arc in the X-Y plane. It was mentioned before that for an Octoboard as a unit of the tracklet, it is normally assumed that tracklets are a straight line. This assumption is sufficient for collecting the inliers. Nevertheless, it is better to use some method to calculate the parameters of a tracklet for more precision in this level. As much as we have more information about each tracklet, the merging process will be more accurate.

On the other hand, for a charged particle with very low momentum (for example in the range of few MeV), the curvature of the tracklet is not completely negligible. However, the necessity to find very low particles must be considered based on the physics study and separating background.

One of the general solutions for a curved trajectory is the least squares circle fitting problem involving the minimization of the function [69]

$$\chi^2 = \sum_i \omega_i \epsilon_i^2 \quad (4.5.1)$$

where ω_i are weights and ϵ_i are

$$\epsilon_i = \pm \left[\sqrt{(x_i - a)^2 + (y_i - b)^2} - R \right] \quad (4.5.2)$$

measurement residuals normal to the trajectory. Moreover, x_i and y_i are the position of the each hit and a , b and R are the coordinates of the center of the circle and its radius with respect to the reference point, respectively. The sign convention before the bracket is for two possible propagation directions depending on the charge of a particle. Subject to this definition for least square, the minimizing problem is nonlinear and requires an iterative solution. For the condition $|\epsilon_i| \ll R$ the equation (4.5.2) becomes

$$\epsilon_i \approx \varepsilon_i = \pm \frac{1}{2} R^{-1} \left[(x_i - a)^2 + (y_i - b)^2 - R^2 \right] \quad (4.5.3)$$

This expression was used for solving the circle fitting problem non-iteratively for a , b and R but there are two main problems for the usage of these parameters. First, these are not Gaussian distributed and the second is for the straight track this solution does not work. In 1990, V.Karimäki introduced a non-iterative procedure to solve a least squares circle fitting problem. For his method, he redefined least squares according to the curvature ($\Omega = \pm \frac{1}{R}$), the distance of closest approach (d_0) to the origin and the direction of propagation (ϕ_0) at the pca. (Here different symbols are used from those that were used for the Hough transform). These parameters are statistically Gaussian distributed. Then equation (4.5.3) in term of these parameters is

$$\varepsilon_i = (1 + \Omega d_0) \eta_i, \quad (4.5.4)$$

where

$$\eta_i = \kappa r_i^2 - r_i \sin(\phi_0 - \phi_i) + \delta, \quad (4.5.5)$$

with

$$\kappa = \frac{1}{2} \frac{\Omega}{1 + \Omega d_0} \quad \text{and} \quad \delta = \frac{1 + \frac{1}{2} \Omega d_0}{1 + \Omega d_0} d_0. \quad (4.5.6)$$

In equation (4.5.5) r_i and ϕ_i are the polar coordinate of each hit. In this notation:

$$\chi^2 = (1 + \Omega d_0)^2 \hat{\chi}^2 \quad (4.5.7)$$

where

$$\hat{\chi}^2 = \sum_i \omega_i \eta_i^2 \quad (4.5.8)$$

For non-iterative solution, first equation (4.5.8) is minimized with respect to the κ , ϕ_0 and δ . And second, the curvature and distance parameters are solved by inverting equation (4.5.6). The result for the first step is

$$\begin{aligned}\phi_0 &= \frac{1}{2} \arctan\left(\frac{2q_1}{q_2}\right) \\ \kappa &= \frac{\sin(\phi_0)C_{xr^2} - \cos(\phi_0)C_{yr^2}}{C_{r^2r^2}} \\ \delta &= -\kappa\langle r^2 \rangle + \sin(\phi_0)\langle x \rangle - \cos(\phi_0)\langle y \rangle\end{aligned}\quad (4.5.9)$$

where $\langle \rangle$ means a weighted average and C_{yr^2} ... are the statistical covariances of the measurements x_i , y_i and $r_i^2 = x_i^2 + y_i^2$ calculated as below:

$$\begin{aligned}C_{xx} &= \langle x^2 \rangle - \langle x \rangle^2 \\ C_{yy} &= \langle y^2 \rangle - \langle y \rangle^2 \\ C_{xy} &= \langle xy \rangle - \langle x \rangle \langle y \rangle \\ C_{xr^2} &= \langle xr^2 \rangle - \langle x \rangle \langle r^2 \rangle \\ C_{yr^2} &= \langle yr^2 \rangle - \langle y \rangle \langle r^2 \rangle \\ C_{r^2r^2} &= \langle r^4 \rangle - \langle r^2 \rangle^2\end{aligned}\quad (4.5.10)$$

And in equation (4.5.9) $q_1 = C_{r^2r^2}C_{xy} - C_{xr^2}C_{yr^2}$ and $q_2 = C_{r^2r^2}(C_{xx} - C_{yy}) - C_{xr^2}^2 + C_{yr^2}^2$. At the end, Ω and d_0 are calculated by inverting equation (4.5.6):

$$\Omega = \frac{2\kappa}{\sqrt{1 - 4\delta\kappa}} \quad \text{and} \quad d_0 = \frac{2\delta}{1 + \sqrt{1 - 4\delta\kappa}}. \quad (4.5.11)$$

As mentioned before, Ω , ϕ_0 and d_0 are statistically Gaussian distributed and therefore the covariance matrix is calculated according to these parameters. The covariance matrix of circle fitting (\mathbf{V}) is given by the inverse of a matrix with elements

$$(\mathbf{V}^{-1})_{jk} = \sum_i \omega_i \frac{\partial \varepsilon_i}{\partial P_j} \frac{\partial \varepsilon_i}{\partial P_k} \quad (4.5.12)$$

computed at minimum χ^2 . For simplicity we denoted the Ω , ϕ_0 and d_0 as P_1 , P_2 and P_3 , respectively [69]. In appendix A the full procedure of V^{-1} calculation is explained. For the condition that $B = 0$ T, the trajectory of a charged particle is a straight line. Thus $\Omega = 0$ and d_0 is simplified to

$$d_0 = x \sin(\phi_0) - y \cos(\phi_0) \quad (4.5.13)$$

After calculating these three parameters, one can find the arc length and therefore the two other remaining parameters for a tracklet.

4.5.2 The S-Z plane parameters

It was explained before that in order to find $\tan(\lambda)$ and z_0 , first, it is needed to calculate the arc length (S), i.e. the shortest distance between a hit and the pca, in the X-Y plane. Equation (4.3.8) shows the arc length for the case that it is assumed the tracklet is a straight line. However, in case the tracklet is curved, it is more precise to use the form of the arc length for the circle [13]. Figure (4.9) shows the arc length, a hit position and the pca point in a trajectory.

For this figure, the reference point is shown in the origin of the coordinate system to simplify the explanation of the arc length. The arc length for a circle is calculated:

$$S = \frac{\Delta\theta}{\Omega} \quad (4.5.14)$$

where $\Omega = \pm \frac{1}{R}$ from equation (4.5.11) and $\Delta\theta = (\theta_{pca} - \theta_{hit})$ is the angle between a hit and the pca position. In addition, the center of the circle is [13] [44]

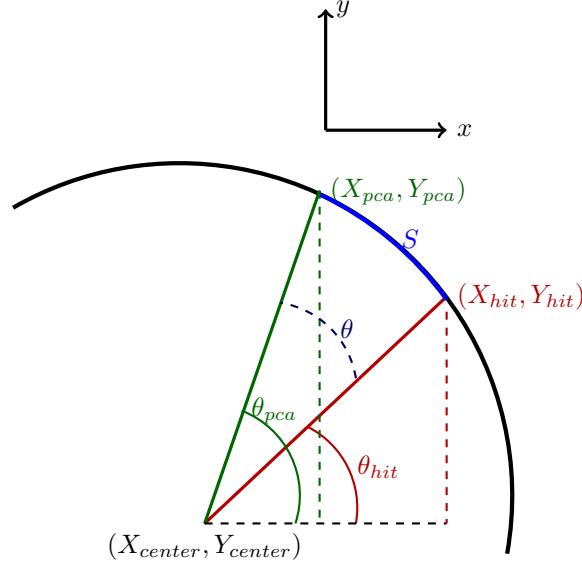


Figure 4.9: The arc length, a hit position, and the pca position. In this figure, for simplicity, the reference point of the track is in the origin of the coordinate system.

$$X_{center} = r_x + \left(\frac{1}{\Omega} - d_0\right) \sin(\phi_0) \quad (4.5.15)$$

$$Y_{center} = r_y - \left(\frac{1}{\Omega} - d_0\right) \cos(\phi_0)$$

where r_x and r_y are the position of the reference point, respectively. Then one can calculate the angle of the pca and the hit position as shown below:

$$\theta_{pca} = \arctan\left(\frac{Y_{pca} - Y_{center}}{X_{pca} - X_{center}}\right) \quad (4.5.16)$$

$$\theta_{hit} = \arctan\left(\frac{Y_{hit} - Y_{center}}{X_{hit} - X_{center}}\right)$$

Therefore the equation (4.5.14) becomes

$$S = \frac{1}{\Omega} \cdot \left(\arctan\left(\frac{Y_{pca} - Y_{center}}{X_{pca} - X_{center}}\right) - \arctan\left(\frac{Y_{hit} - Y_{center}}{X_{hit} - X_{center}}\right) \right) \quad (4.5.17)$$

And as mentioned before, S is negative for the case that the particle first crossed the hit and then pca point and it is positive if the particle first crossed the pca point.

In the S-Z plane, the projection of a helix is a straight line and its equation generally is

$$z = (z_0 + r_z) + S \cdot \tan(\lambda) \quad (4.5.18)$$

where $\tan(\lambda)$ is the slope dz/dS and z_0 is the intersect of the straight line and r_z is the z component of the reference point which according to the assumption, it is zero because of the reference point position. For finding the parameters of equation (4.5.18), the linear regression is implemented.

In this case, a linear least squares estimation is used for the parameters. The general equation for a straight line is [67] [77]

$$\mathbf{Y} = \hat{\beta} \mathbf{X} \quad (4.5.19)$$

where

$$\hat{\beta} = \begin{bmatrix} \beta_0 \\ \beta_1 \end{bmatrix} \text{ is a (2x1) matrix}$$

$$\mathbf{X} = \begin{bmatrix} 1 & x_1 \\ 1 & x_2 \\ \vdots & \vdots \\ 1 & x_n \end{bmatrix} \text{ is a (nx2) matrix}$$

and

$$\mathbf{Y} = \begin{bmatrix} y_1 \\ y_2 \\ \vdots \\ y_n \end{bmatrix} \text{ is a (nx1) matrix}$$

Therefore the slope and intersect of the straight line are calculated in the matrix form

$$\hat{\beta} = (\mathbf{X}' \mathbf{X})^{-1} \mathbf{X}' \mathbf{Y} \quad (4.5.20)$$

where X is a matrix of S and Y is a matrix of z. $\hat{\beta}$ consists of $\beta_0 = z_0$ as the intersect and $\beta_1 = \tan(\lambda)$ as the slope of the straight line.

As regards to the longitudinal resolution in the z direction, the weighted linear least square is used for finding parameters. The weight is taken from the uncertainty in Z which for a TPC is ($w = 1/\sigma_L^2$) [67]. Therefore there is a $n \times n$ diagonal matrix (G) which should be taken into account. In this case, $\hat{\beta}$ is [77]

$$\hat{\beta} = (\mathbf{X}' \mathbf{G}^{-1} \mathbf{X})^{-1} \mathbf{X}' \mathbf{G}^{-1} \mathbf{Y} \quad (4.5.21)$$

where G is

$$\mathbf{G} = \begin{bmatrix} w_1^2 & 0 & \cdots & 0 \\ 0 & w_2^2 & \ddots & \vdots \\ \vdots & \ddots & \ddots & 0 \\ 0 & \cdots & 0 & w_n^2 \end{bmatrix}$$

At the end, the parameters of all tracklets, the covariance matrices and their hits are collected and sorted based on their Octoboard's number for the merging process. Figure (4.10) illustrates the flowchart of the finding process for an Octoboard.

The general procedure of finding a tracklet is summarized as follows:

1. For the first step, the Hough transform is used in the X-Y plane for initialization of a bivariate normal distribution (BND) fit in the Hough space utilized to have a pre-selection of inliers and calculate the XY-ellipse.
2. The Hough Transform and a BND are performed for the pre-selected inliers in the S-Z plane for calculating the SZ-ellipse.
3. For the final selection, there is a loop over all hits again. Based on the two ellipses the inliers are collected and stored in a vector for the next step.
4. After that, a fitting method is used on the inliers in each plane to estimate the parameters of each segment. Then, each segment with its parameters is identified as a tracklet. Finally, all tracklets are collected and sorted based on the relevant Octoboard's number.

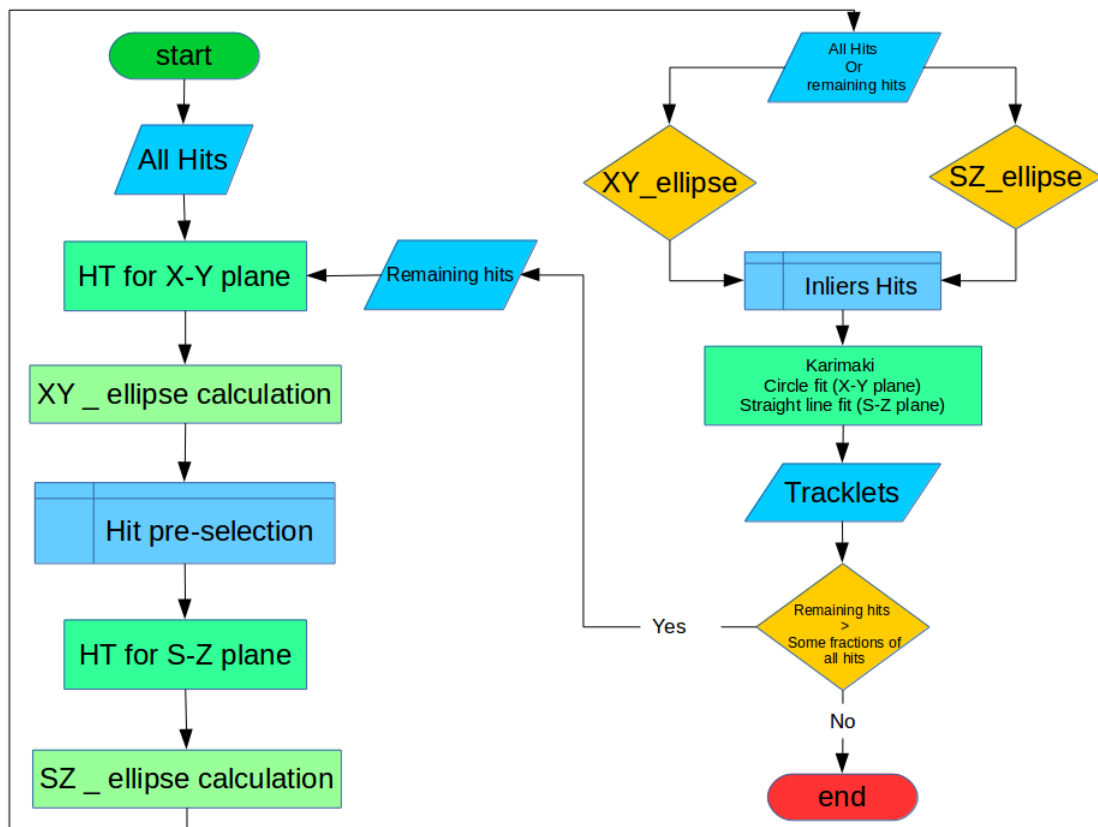


Figure 4.10: The general flowchart of the track finding for an Octoboard.

4.6 The merging process

The last part of the track finding is the merging process. In this step, an algorithm based on the least square tries to connect and merge the relevant tracklets to each other. For this purpose, there is a loop over all Octoboards which have at least one tracklet. These Octoboards are sorted from the outer layer of a TPC to the inner layer which is close to the vertex point. The main reason is, the density of the tracks is higher in the inner layer or vertex point, thus, separation of two or more tracklets is easier in the outer layer.

The Merging process is done in three steps and figure (4.11) illustrates these steps of the merging process for three Octoboards as an example [67].

- **Extrapolation:** first of all the middle points of two tracklets from two sequential Octoboards are extrapolated to a point in the middle of the two tracklet (figure (4.11-a)). This new point is defined as the new reference point for both tracklets and the parameters for these two tracklets are recalculated based on this new reference point.
- **Comparison:** then the χ^2/ndf based on the new parameters for the two tracklets is calculated and if it is less than a criterion then these two tracklets belong to the same track. Otherwise, this process will be done with the tracklet from the first Octoboard and either another tracklet from the second Octoboard, depending on whether or not there is another one, or a tracklet from the next Octoboard in the sequence.
- **Merging:** the relevant tracklets are merged together and a new tracklet is defined. The first step is repeated using the new tracklet with a tracklet from the next Octoboard (figure (4.11-b)). These steps continue until the end of the sequence and then it returns back to the beginning for the remaining tracklets (figure (4.11-c)). At the end, all tracks which have a number of hits more than a criterion are collected as the found tracks.

For extrapolation, the new parameters for both tracklets at the new reference point are defined as $(d'_0, \phi'_0, \Omega', \tan \lambda', z'_0)$ where $\Omega' = \Omega$ because the curvature of the particle's trajectory is the same in the different points along the trajectory. In addition, λ is also fixed. The new coordinate point for the new reference point at the X-Y plane is [37]

$$r'_x + (R - d'_0) \sin(\phi'_0) = r_x + (R - d_0) \sin(\phi_0) \quad (4.6.1)$$

$$r'_y + (R - d'_0) \cos(\phi'_0) = r_y + (R - d_0) \cos(\phi_0)$$

where $R = \frac{1}{\Omega}$ is the radius of the trajectory in the X-Y plane. For simplicity these two equations are written as:

$$\frac{(R - d'_0)}{(R - d_0)} \sin(\phi'_0) = \sin(\phi_0) - \frac{\Delta r_x}{(R - d_0)} \quad (4.6.2)$$

$$\frac{(R - d'_0)}{(R - d_0)} \cos(\phi'_0) = \cos(\phi_0) - \frac{\Delta r_y}{(R - d_0)}$$

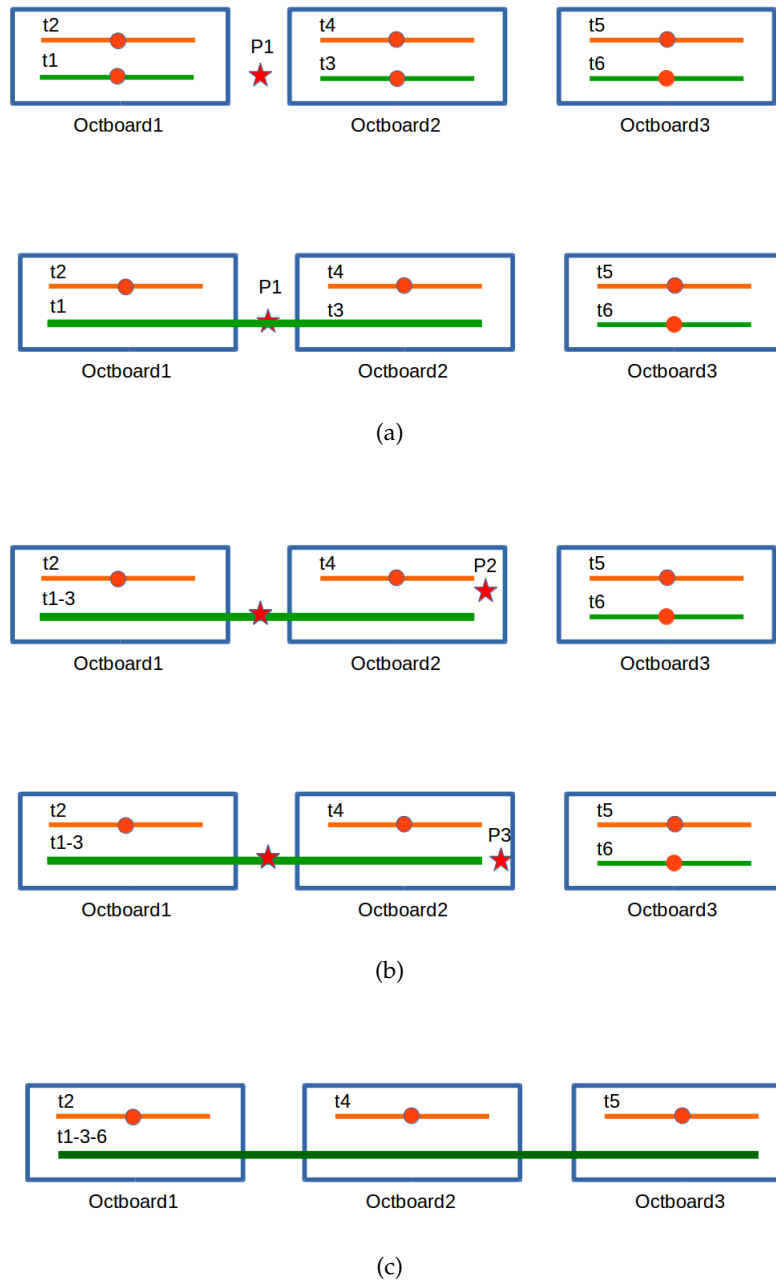


Figure 4.11: (a) The extrapolation of t_1 and t_3 from Octboard 1 and 2, respectively, to point P_1 (the midpoint between two tracklets as a new reference point). If the least square over the number of degrees of freedom is less than a criterion, they are merged together. (b) Then first, the new tracklet called t_{1-3} and t_5 from Octboard 3 are extrapolated to point P_2 . If χ^2/ndf does not fulfill the criterion, then it will be repeated for t_{1-3} and t_6 for the new reference point at P_3 . (c) At the end, the full track is found.

where $\Delta r_x = r'_x - r_x$ and $\Delta r_y = r'_y - r_y$. Then ϕ'_0 and d'_0 are calculated as follows:

$$\phi'_0 = \arctan \left(\frac{\sin(\phi_0) - \frac{\Delta r_x}{(R-d_0)}}{\cos(\phi_0) - \frac{\Delta r_y}{(R-d_0)}} \right) \quad (4.6.3)$$

$$d'_0 = R - (R - d_0) \sqrt{1 + \frac{-2\Delta r_x \sin(\phi_0) + 2\Delta r_y \cos(\phi_0)}{(R - d_0)} + \frac{\Delta r_x^2 + \Delta r_y^2}{(R - d_0)^2}} \quad (4.6.4)$$

For $\Omega \rightarrow 0$ limit, there is another expression for d_0 with better behavior

$$d'_0 = d_0 + \Delta r_x \sin(\phi_0) - \Delta r_y \cos(\phi_0) + (\Delta r_x \cos(\phi_0) + \Delta r_y \sin(\phi_0)) \tan \left(\frac{\phi'_0 - \phi_0}{2} \right) \quad (4.6.5)$$

In the S-Z plane, the arc length S is

$$S = \frac{\phi'_0 - \phi_0}{\Omega} \quad (4.6.6)$$

and its sign depends on the direction of flight of the particle. At the end, z'_0 is given by

$$z'_0 = z_0 + S \tan(\lambda) \quad (4.6.7)$$

The covariance matrix of each tracklet in the new reference point is

$$\mathbf{C}' = \mathbf{J} \mathbf{C} \mathbf{J}^T \quad (4.6.8)$$

where \mathbf{J} is the Jacobian matrix, \mathbf{C} is the original covariance matrix of the tracklet and \mathbf{J}^T is the transpose of the Jacobian matrix. In the X-Y plane, the Jacobian matrix is calculated based on equation (4.6.1). The final result of the relevant derivatives of the transformation for the curved track are [37]

$$\begin{aligned} \frac{\partial \Omega'}{\partial \Omega} &= 1 \\ \frac{\partial \Omega'}{\partial \phi_0} &= 0 \\ \frac{\partial \Omega'}{\partial d_0} &= 0 \\ \frac{\partial \phi'_0}{\partial \Omega} &= -\frac{1}{(1 - \Omega d'_0)^2} (\Delta r_x \cos(\phi_0) + \Delta r_y \sin(\phi_0)) \\ \frac{\partial \phi'_0}{\partial \phi_0} &= \left(\frac{1 - \Omega d_0}{1 - \Omega d'_0} \right) + \frac{\Omega^2 (1 - \Omega d_0)}{2(1 - \Omega d'_0)^2} (d_0'^2 - (\Delta r_x + d_0 \sin(\phi_0))^2 - (\Delta r_y - d_0 \cos(\phi_0))^2) \\ \frac{\partial \phi'_0}{\partial d_0} &= -\frac{\Omega^2}{(1 - \Omega d'_0)^2} (\Delta r_x \cos(\phi_0) + \Delta r_y \sin(\phi_0)) \\ \frac{\partial d'_0}{\partial \Omega} &= \frac{1}{2(1 - \Omega d'_0)} (d_0'^2 - (\Delta r_x + d_0 \sin(\phi_0))^2 - (\Delta r_y - d_0 \cos(\phi_0))^2) \\ \frac{\partial d'_0}{\partial \phi_0} &= \frac{1 - \Omega d_0}{1 - \Omega d'_0} (\Delta r_x \cos(\phi_0) + \Delta r_y \sin(\phi_0)) \\ \frac{\partial d'_0}{\partial d_0} &= 1 + \frac{\Omega^2}{2(1 - \Omega d'_0)} (d_0'^2 - (\Delta r_x + d_0 \sin(\phi_0))^2 - (\Delta r_y - d_0 \cos(\phi_0))^2) \end{aligned} \quad (4.6.9)$$

For the case that the tracklet is straight line the Jacobian matrix is

$$\begin{aligned}
\frac{\partial \Omega'}{\partial \Omega} &= 1 \\
\frac{\partial \Omega'}{\partial \phi_0} &= 0 \\
\frac{\partial \Omega'}{\partial d_0} &= 0 \\
\frac{\partial \phi'_0}{\partial \Omega} &= -(\Delta r_x \cos(\phi_0) + \Delta r_y \sin(\phi_0)) \\
\frac{\partial \phi'_0}{\partial \phi_0} &= 1 \\
\frac{\partial \phi'_0}{\partial d_0} &= 0 \\
\frac{\partial d'_0}{\partial \Omega} &= \frac{1}{2}(d'_0 - (\Delta r_x + d_0 \sin(\phi_0))^2 - (\Delta r_y - d_0 \cos(\phi_0))^2) \\
\frac{\partial d'_0}{\partial \phi_0} &= (\Delta r_x \cos(\phi_0) + \Delta r_y \sin(\phi_0)) \\
\frac{\partial d'_0}{\partial d_0} &= 1
\end{aligned} \tag{4.6.10}$$

Moreover, in the S-Z plane the Jacobian matrix is

$$\begin{aligned}
\frac{\partial \tan(\lambda')}{\partial \tan(\lambda)} &= 1 \\
\frac{\partial \tan(\lambda')}{\partial z_0} &= 0 \\
\frac{\partial z'_0}{\partial \tan(\lambda)} &= S \\
\frac{\partial z'_0}{\partial z_0} &= 1
\end{aligned} \tag{4.6.11}$$

After calculating the parameters and covariance matrices of the two tracklets at the new reference point, the least square is

$$\chi^2 = (\mathbf{v}'_1 - \mathbf{v}'_2)(\mathbf{C}'_1 + \mathbf{C}'_2)^{-1}(\mathbf{v}'_1 - \mathbf{v}'_2)^T \tag{4.6.12}$$

where \mathbf{v}'_1 , \mathbf{v}'_2 , \mathbf{C}'_1 and \mathbf{C}'_2 are the vector of the parameters and covariance matrices of the first and second tracklets, respectively.

In addition, the number of degrees of freedom (*ndf*) depends on the magnetic field. In the absence of a magnetic field, *ndf* is 4 and for experiments with a magnetic field, it is 5. In case that the χ^2/ndf is less than a criterion then these two tracklets are merged together. The criterion for the merging step is determined experimentally. Figure (4.12) shows two samples of the χ^2/ndf distribution for the real and simulation data for an experiment which was done at the LP TPC at DESY with 20 Octoboards and a 1 T magnetic field. The energy of the electron was 1 GeV for both simulation and real experiment. Figure (a) is for 5000 events for a real data experiment and figure (b) is for 1000 events for a simulation data experiment. These plots can give a hint for choosing a cut for each experiment for both real and simulation data.

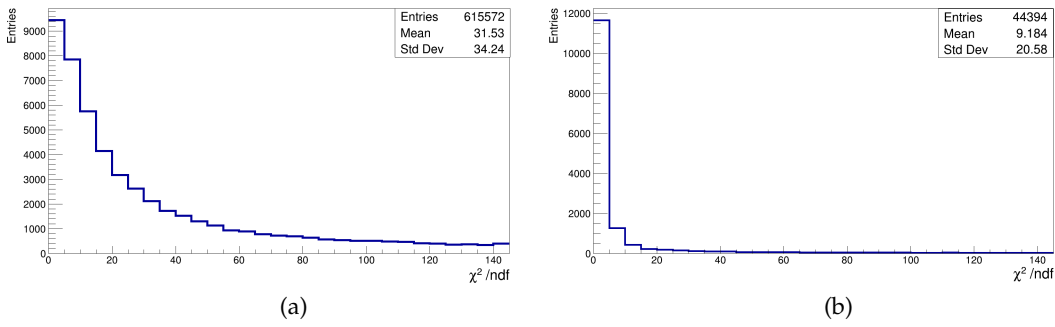


Figure 4.12: Examples of the χ^2/ndf distribution (a) for real data for 5000 events with more than 600000 merging process of tracklets and (b) for simulation data for 1000 events with more than 40000 merging process of tracklets.

According to these two example plots, one can choose a criterion between 80 to 100 for real data for finding the relevant tracklets. However, this criterion for simulation could be less than 10 because of the better quality of hits and tracklets in the simulation. After that all hits for relevant tracklets are collected and again by using Karimäki and the weighted linear least square the new parameters and the covariance matrix of the new tracklet are defined. The new reference point is also used as the reference point of the new tracklet. These processes are repeated until all tracklets for all Octoboard are checked. At the end, only tracks with a certain number of hits are collected. After the finding process, the next step is track fitting to find the track parameters. It was mentioned before that the GBL is the track fitting algorithm implemented for this thesis.

4.7 Recollection inliers

After finding inliers and using an algorithm for fitting, it is found that in some events some Octoboards were missed. This happened during the merging process. As mentioned in the previous section, choosing a cut for merging needs to be optimized for each experiment. Sometimes the value for cutting will not collect all relevant tracklets for all Octoboards.

Another reason is, for some events, there is a blob, maybe because of a delta electron, in some part of the track or tracklet. In such a case, this phenomenon has an effect on the parameters of the tracklet. Therefore during the merging step, this tracklet can not fulfill the criterion for merging and is rejected. Figure (4.13) shows an example of this issue. The red points are inlier hits and the rest are outliers which are mostly noise. One can see inside the blue circle an Octoboard which is along the track but it is missed. In this Octoboard there is a dense area next to the tracklet and this can affect the parameters of this tracklet.

In order to solve this issue and to collect all inliers, there is a post-processing after the fitting process. In this post-processor, the parameters of the track are used to recollect all hits missed in the previous step. In order to consider hits in this step, they need to have a distance less than a factor of the transverse and longitudinal spatial resolution in the X-Y and S-Z plane.

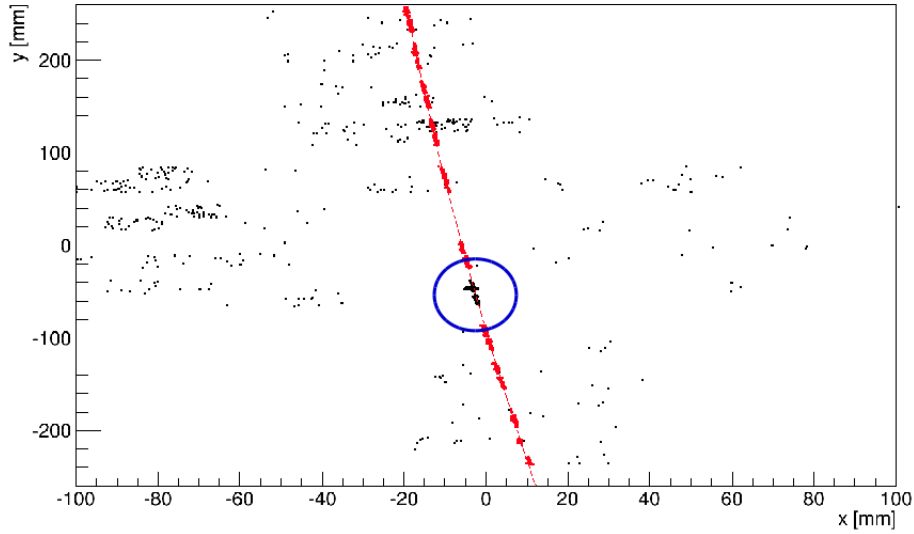


Figure 4.13: A track after finding and fitting. It can be seen an Octoboard (tracklet) is missed. Probably a blob, which is visible in this figure, has an effect on the parameters of the tracklet.

In this post-processor, first of all the direction of flight at each hit based on the track parameters is calculated [37]:

$$\phi = \arctan \left(\frac{\sin(\phi_0) - \Omega(x - r_x)}{\cos(\phi_0) + \Omega(y - r_y)} \right) \quad (4.7.1)$$

where (x, y) is the position of a hit and (r_x, r_y) is the position of the reference point in the X-Y plane, Ω is the curvature of the track and ϕ_0 is the direction of flight of the track. After that, according to ϕ , the X, Y and Z of a point along the track is given by:

$$\begin{aligned} X_t &= X_{center} - \left(\frac{1}{\Omega}\right) \sin(\phi) \\ Y_t &= Y_{center} + \left(\frac{1}{\Omega}\right) \cos(\phi) \end{aligned} \quad (4.7.2)$$

$$Z_t = z_0 + r_z + S \tan(\lambda)$$

where the arc length is calculated according to equation (4.6.6). From equations (4.2.3) and (4.2.4) it is possible to calculate the transverse and longitudinal spatial resolution at Z_t and then collect all missed hits for which $|X_t - x|$ and $|Y_t - y|$ are less than a factor of σ_{xy} and $|Z_t - z|$ is less than a factor of σ_z . For collecting inliers in the Z direction a constant (16 mm^2) was added under squirt root to the intrinsic longitudinal spatial resolution. This number was estimated based on the experiment results to correct time walk effect []. For this thesis five σ_{xy} and five σ_z have been utilized. Figure (4.14) shows the same event shown in figure (4.13) after recollecting inliers.

This post-processor works for most of the event perfectly. There are a few events that still have a missed Octoboard and the reason is the initial track for recollection is far away from those hits along the track. The only solution is to have again another recollection processor after the first one, however, the number of these events are so

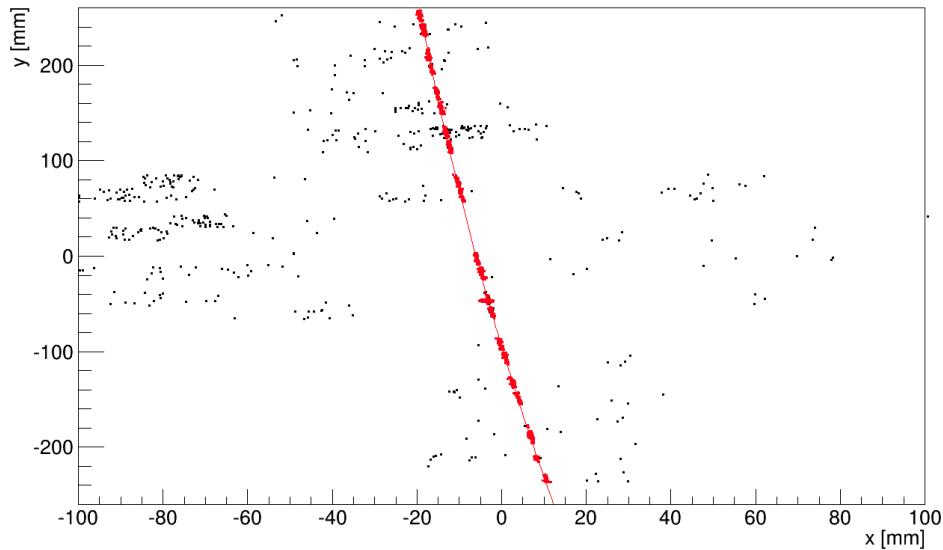


Figure 4.14: The same track shown in figure (4.13) after recollection inliers.

small that it can be ignored. After the recollection process, again one of the fitting processors is used for the final step of the track reconstruction. And finally, one can use these algorithms for different analysis. In section 4.8, the processors in the MarlinTPC for the finding and also for the recollection the inliers will be explained, particularly the parameters which are used in these codes.

4.8 Processors in MarlinTPC

In the previous sections, the finding and recollection of inliers were explained. In this section, two codes are introduced as implemented in the MarlinTPC framework for these purposes.

The first one is "**InGridBNDHoughTransformProcessor**" which is for the finding process and does the Hough transform and a bivariate normal distribution fit in the Hough space in order to collect the inliers. After that, the Karimäki and weighted linear regression fit defines and collects tracklets. At the end, as explained, the merging process is done by this processor and the output is a collection of candidate tracks. Table (4.1) illustrates the main and optional parameters used in this processor. Some parameters need more explanation to clarify the usage of them.

OffsetX and **OffsetY** are used for objects of some classes utilized in this processor. In the LP TPC, the position of each hit is identified by (x,y,z) with the origin of the coordinate system at the center of the X-Y plane in the anode side of the TPC. However, some classes that are used in this processor have been defined based on the coordinate system where the origin is outside of the TPC.

Therefore, in order to solve this mismatching, these two offsets are implemented to adjust the position of each hit according to the right origin of the coordinate system.

ManyOctoboards in the processor is for identifying whether the data is for many Octoboards or not. For each Octoboard there is a Hough space according to the local coordinate. For the case that there is only one Octoboard, the local coordinate

matches with the global coordinate but for data with many Octoboards, the local coordinate has to be calculated.

AutoScaling, as a default, is true which means the code based on the z position of the hits, chooses the appropriate scale factor for both fitting range and resizing the ellipse. It is done in both X-Y and S-Z plane. One can change this parameter to the false and tune **ScaleFactorBNDFitXY**, **ScaleFactorBNDFitSZ**, **ScaleFactorEllipseXY** and **ScaleFactorEllipseSZ** parameters manually.

In section 4.7, the recollection of the inliers was illustrated. In the MarlinTPC this job is done by "**InGridCollectHitPostProcessor**".

InGridBNDHoughTransformProcessor	
Mandatory Parameters	Description
Gas	Gas mixture (e.g. T2K ,...)
DriftField	Amount of the drift filed
PercentageAllHits	Percentage of the remaining hits from all hits to stop the loop for the collecting inliers (figure ??)
HoughSpaceMaxRho	Maximum range of ρ in the Hough space
HoughSpaceMaxPhi	Maximum range of ϕ in the Hough space
HoughSpaceMinPhi	Minimum range of ϕ in the Hough space
HoughSpaceMaxLambda	Maximum range of λ in the Hough space
HoughSpaceMinLambda	Minimum range of λ in the Hough space
Chi2/ndf	χ^2/ndf cut for the merging process
OffSetX	Offset in the x-axis for many Octoboards for shifting the origin of the coordinate
OffSetY	Offset in the y-axis for many Octoboards for shifting the origin of the coordinate
UnitOfSegments	Unit of the segmentation of a track (as default is 2 corresponding to an Octoboard)
MinimumNumberHits	Minimum number of hits in a candidate track as an acceptable track
Optional Parameters	Description
DeleteHistogram	Delete histogram for the Hough transform
ManyOctoboards	For experiments with many Octoboards
AutoScaling	Using auto scaling factor for ellipses and fitting ranges (default is true)
ScaleFactorBNDFitXY	Scale factor of the fitting range for BND fit in the X-Y plane
ScaleFactorBNDFitSZ	Scale factor of the fitting range for BND fit in the S-Z plane
ScaleFactorEllipseXY	Scale factor for resizing the ellipse for 1/e of the peak of the fit in the X-Y plane
ScaleFactorEllipseSZ	Scale factor for resizing the ellipse for 1/e of the peak of the fit in the S-Z plane

Table 4.1: The mandatory and optional parameters for InGridBNDHoughTransformProcessor in the MarlinTPC.

InGridCollectHitPostProcessor	
Mandatory Parameters	Description
Gas	Gas mixture (e.g. T2K ,...)
DriftField	Amount of the drift field
ScaleFactorSigmaT	Scale factor of the σ_{xy}
ScaleFactorSigmaL	Scale factor of the σ_z
MinimumNumberHits	Minimum number of hits in a candidate track as an acceptable track

Table 4.2: The mandatory parameters for InGridCollectHitPostProcessor in the MarlinTPC.

Chapter 5

Simulation and optimization

5.1 Introduction

In chapter 3, it was mentioned that simulation is a kind of the supervised learning in pattern recognition in order to improve and generalize an algorithm. According to this concept, the training dataset and their targets are identified. Therefore, it is the best method to control the performance of the algorithm. In addition, according to the supervised learning, the algorithm is designed in the way that can determine the best parameters for each event by itself. It means, instead of needing to tune the parameters manually, the algorithm is able to specify the optimum parameters for each track or event by itself.

As an example for **InGridBNDHoughTransformProcessor**, assume that for an event there are two tracks which their hits have different drift length. In such a case, the algorithm has to be able to find the best bin size, fit range of the bivariate normal distribution and consequently the scale factor of the ellipse in the Hough space in order to collect the inliers.

In chapter 4, it was explained that the size of the bin in the Hough space is matched according to the transverse and longitudinal resolution of the X-Y and S-Z plane. And in this chapter, the optimization process which has been done to find the best factors for the fit range and scale of the ellipse in both planes will be explained. According to these optimization results, the algorithm was written in the way that it can find the best factors based on the drift length of hits of a track for each Octoboard, therefore there is no need to tune parameters for each track manually.

In the first part of this chapter the simulation chain in the MarlinTPC [49] and the processor utilized for simulation will be explained and after that the optimization will be illustrated.

5.2 Simulation chain in MarlinTPC

Figure (5.1) shows the chain of processors which are used for simulation of hits for the InGrid chip. First of all, a charged particle, which for this thesis is normally an electron, is generated by a generator based on the Monte Carlo method in MarlinTPC called **generateelectronoctoboard**. This code is a modification code of the **generateElectronsForLP1** written for simulating one electron. This modified version was written for this thesis and can generate more than one electron for the LP TPC with different energies and parameters.

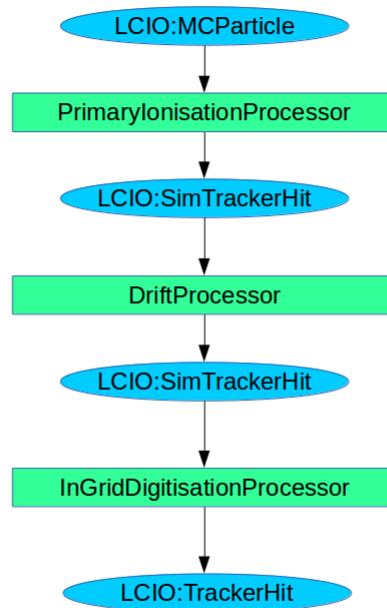


Figure 5.1: The chain of all processors used for simulation of InGrid

The output of this generator is collected as an `MCParticle` in LCIO [42][43] format which is the input of the first processor in the simulation chain. In the output the original particle is also identified. Therefore later the origin of each hit is clear and this information is used to find hit efficiency, hit purity, track efficiency, and track purity (see chapter 3).

The **PrimaryIonisationProcessor** [78] forms clusters of electrons from the primary ionization along the trajectory of the charged particle in a TPC. For this purpose, the information about the number of clusters on a certain track length and the number of electrons in these clusters is calculated by HEED, a software for the simulation of ionization in gases [79][80].

The **DriftProcessor** calculates the effect of the drift based on the drift velocity and transverse and longitudinal diffusion for the given E and B field [80]. The position of each electron changes during the drifting process based on a Gaussian distribution. In the X - Y plane, the width of this Gaussian is given by equation (2.5.22) and the new position of the primary electrons in this plane is calculated by adding a random value from the Gaussian distribution [78].

In a TPC the Z position is calculated from the measured drift time. Thus, for the simulation, a drift time is calculated from the drift velocity and the drift distance. Therefore, the drift time is the relevant coordinate of the electrons in the drift direction. In addition, the width of the Gaussian distribution based on the longitudinal diffusion is taken into account for specifying the width of the charge cloud in the Z direction [78].

The **InGridDigitisationProcessor** was prepared for converting simulated hits (`SimTrackerHit`) to hits in the readout electronics (`TrackerHit`) [43]. For the InGrid chip, it was always assumed that it can detect the primary electrons. Therefore, in this processor, each hit maps to a pixel which has the same X and Y coordinate as the hit. With this processor, one is also able to generate noise with a random distribution in 3-dimensions of the TPC and add to simulation.

Each hit has the information of the MCParticle and covariance matrix based on the transverse and longitudinal diffusion which later can be used for analysis. The Z position of each hit is calculated according to the drift time and the drift velocity. Table (5.1) illustrates the mandatory parameters for this processor in the MarlinTPC.

InGridDigitisationProcessor	
Mandatory Parameters	Description
Gas	Gas mixture (e.g. T2K ,...)
DriftField	Amount of the drift filed
Noise	Minimum number of noise for noisy events
MinimumRangeofReadoutX	Minimum range of the readout system in X direction
MaximumRangeofReadoutX	Maximum range of the readout system in X direction
MinimumRangeofReadoutY	Minimum range of the readout system in Y direction
MaximumRangeofReadoutY	Maximum range of the readout system in Y direction

Table 5.1: The mandatory parameters for InGridDigitisationProcessor in MarlinTPC.

In chapter 3, the general definitions for the track efficiency and purity were given. The algorithm in MarlinTPC which has been prepared for analysis based on the simulation is **InGridTrackAnalysisProcessor**. The input of this processor is the reconstructed track from simulation and the output is the result for track efficiency, track purity, hit efficiency, hit purity, loss rate of the reconstruction process, number of ghost and clone tracks. The numbering of the clone tracks is done assuming that the thresohld for defining the correct track is set to be less than 50% of the MC particle hits. Table (5.2) shows the parameters of this processor in MarlinTPC.

InGridTrackAnalysisProcessor	
Mandatory Parameters	Description
Gas	Gas mixture (e.g. T2K ,...)
DriftField	Amount of the drift filed
Percentage of MC Hits	Percentage of MC particle hits that a track needs to be counted as a correct track

Table 5.2: The mandatory parameters for InGridTrackAnalysisProcessor in MarlinTPC.

5.3 Optimization of InGridBNDHoughTransformProcessor

It was mentioned in chapter 4 that there are four parameters in the algorithm; two for changing the fit range in the X-Y and S-Z planes and the two others are the scaling factors in order to change the size of the ellipse in ρ and ϕ for collecting the inliers. It was also mentioned that the size of bins in the Hough space is adjusted according to the transverse and longitudinal diffusion. Therefore, because of the changing bin size, the fit range and also the size of the ellipse have to be changed, otherwise, the algorithm is not able to collect the sufficient inliers.

In order to avoid any arrangement of the four factors manually, the optimization process for four factors based on the simulation was done. All simulations were done based on the test beam for the LP TPC and for one Octoboard. These factors, however, later were modified based on the real data from the test beam experiment.

Due to the fact that the quality of the real data is not as good as the simulation data, this modification was necessary for improving the performance of the algorithm for the real data. It was explained that the correlation of these factors between the X-Y and S-Z plane are negligible (chapter 4-section 4.4). Thus the optimization process was done first for the X-Y plane and then for S-Z plane. For analysis and calculating track efficiency, it was assumed that a correct track is associated with its true MC particle on condition that it has more than 60% of MC particle hits (see chapter 3).

In addition, in the optimization process, the optimization of the efficiency is more important than the purity, as ghost tracks can be reduced by further algorithms while the efficiency cannot be increased later. For instance, the number of ghost track can be reduced by implementing a cut based on the number of hits per track.

5.3.1 Optimization in the X-Y plane

For the optimization, 1000 events with two electrons each with the trajectories parallel to the x-axis were generated for eight different drift distances. Table (5.3) illustrates the parameters and conditions used in the optimization process. This study was done for two cases; first for the case that the distance of two electrons in Y direction was 2mm (figures (5.2-a) and (5.2-b)). With this distance, one can see by eye two tracks for the low drift length (30 mm) but for the long drift length (500 mm), the distinction between two tracks is impossible. In the second case the distance of two electrons was 5 mm. For such a situation, two tracks even for a long drift length are distinguishable by eye as can be seen in figures (5.2-c) and (5.2-d). The Z position of the two tracks in both cases is the same.

Optimization in the X-Y plane	
Parameters	Description
Energy	6 GeV
Magnetic field	1 T
Drift length (mm)	30, 50, 70, 100, 203 , 300, 400, 500
The scale factor of the fit range	{1, ..., 4} of σ_ρ and σ_ϕ with 0.5 step
The scale factor of the ellipse	{1, ..., 8} of the semi-major and semi-minor axes with 0.5 step

Table 5.3: The parameters of the optimization in the X-Y plane.

In table (5.3), one of the selected drift lengths is 203 mm. The reason is that the transverse diffusion for this drift length and a 1 T magnetic field for LP TPC is equivalent to the transverse diffusion for the full drift length and 3.5 T magnetic field for the ILC TPC. Therefore, one can extrapolate the result of the track efficiency for this length to the full drift length of the ILC TPC.

For each drift length mentioned in table (5.3) the track efficiency and purity are determined as a function of both, the scale of the fit range and the scale of the ellipse axes. Figures (5.3) to (5.6) show these plots for the lowest and longest drift length for both cases (2 mm and 5 mm distance between two tracks). Each plot consists of three axes. The x-axis shows the scale factor of the fit range, the same factor is used for σ_ρ and σ_ϕ .

The y-axis shows the scale factor of the semi-major and semi-minor axes of the ellipse. Again one single factor is used for both axes. And the z-axis shows the track efficiency (upper plots) and purity (lower plots).

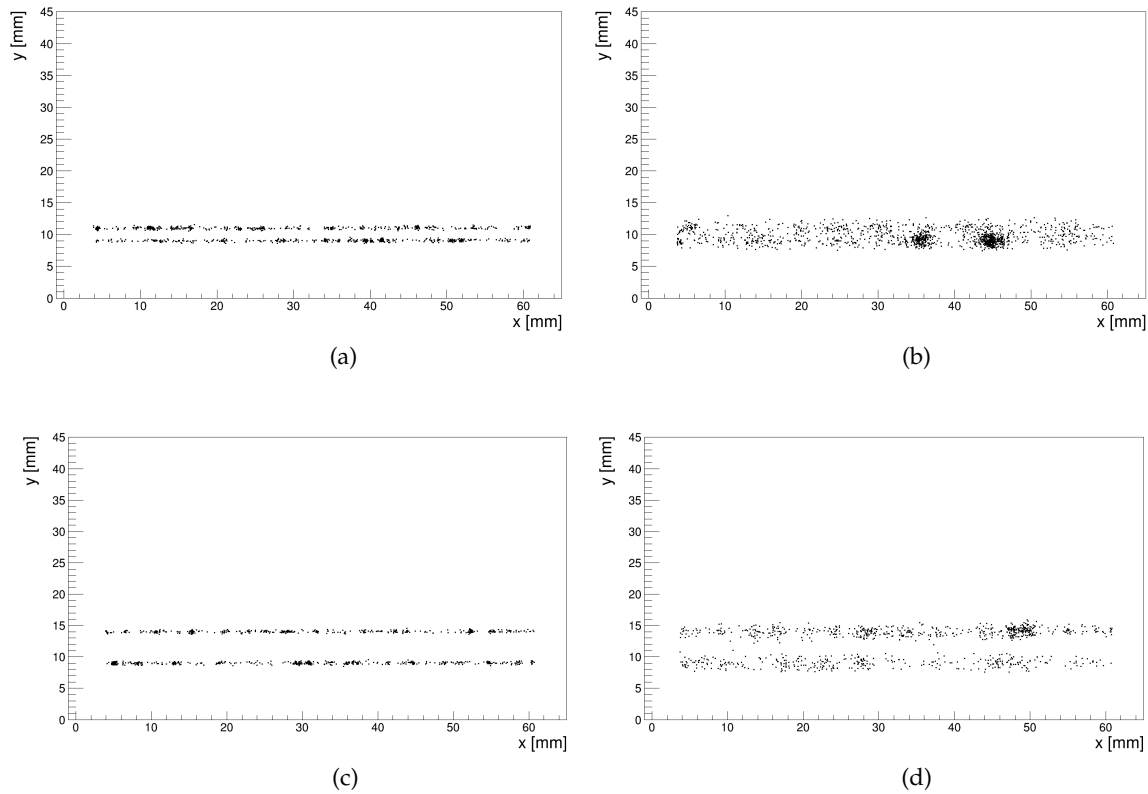
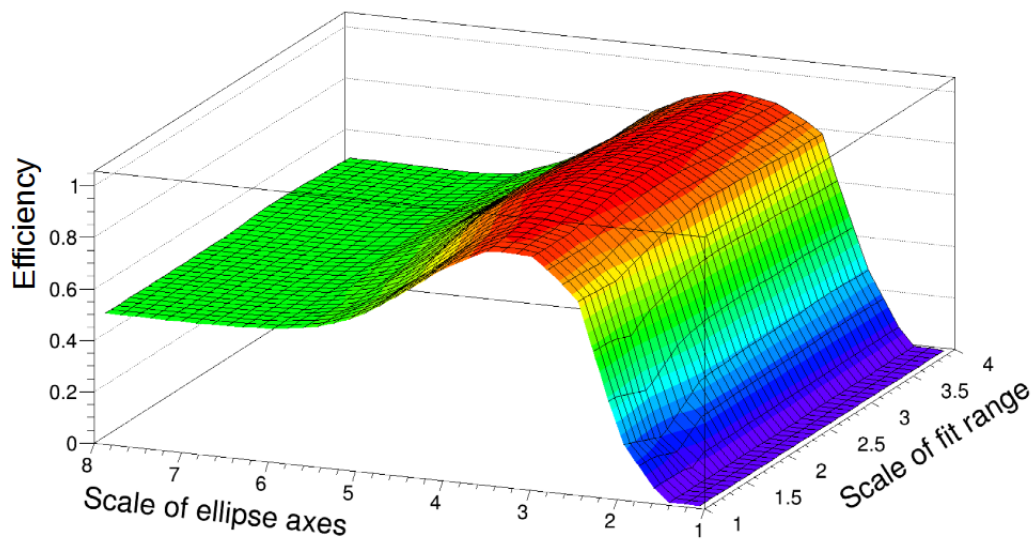


Figure 5.2: Simulation of two tracks (a) with 2 mm distance in the Y direction and 30 mm drift length, (b) with 2 mm distance and 500 mm drift length, (c) with 5 mm distance and 30 mm drift length and (d) with 5 mm distance and 500 mm drift length.

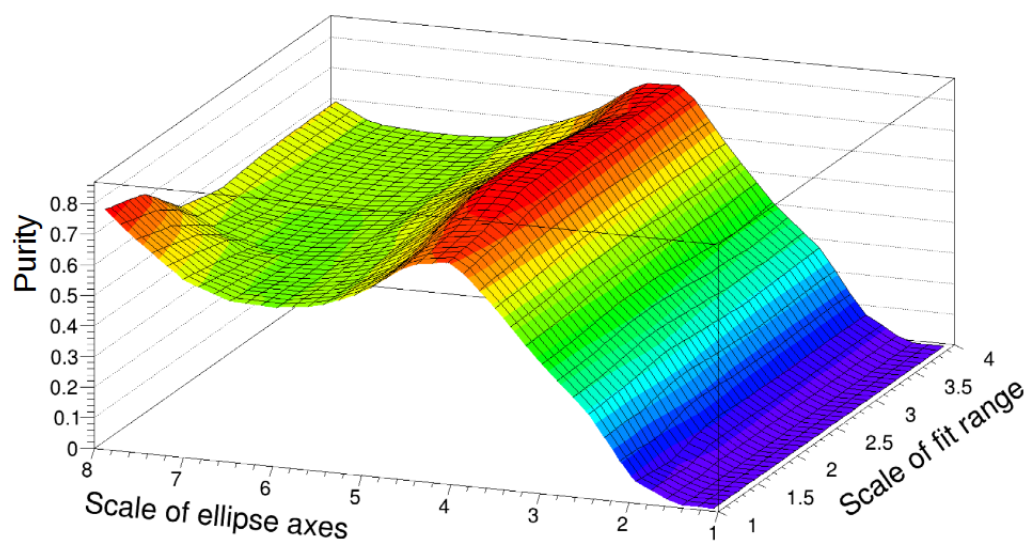
Figures (5.3) and (5.4) show the track efficiency and track purity for the minimum and maximum drift length with 2 mm distance between two tracks. Here and in the following figures, it can be seen that the efficiency and purity depend strongly on the scale factor for the ellipse axes, while the dependency on the scale of the fit range is minor. It can be seen from the figure (5.2) that for the 500 mm drift distance two tracks are merged together. For this reason, the track efficiency cannot be better than 50% as shown in figure (5.4-a) which means the algorithm is able to find only one track and it is also clear from the track purity.

Meanwhile, for the case that there was 5 mm distance between two tracks even for the maximum drift length the algorithm can find two tracks with high efficiency around 100% (figure (5.6-a)) for the scale factor of ellipse axes around two. The track purity, however, has a fluctuation for the scale factor of ellipse axes. There are two regions that have highest track purity; one for the large-scale factors and one for the scale factor between two and three. The reason is, for the scale factors more than four the algorithm collects and assigns all hits to one track. Therefore the track efficiency reduces to 50% (figure (5.6-a)) and consequently the purity increases to 100%.

For the first try to find the optimum scale factors, the result of the track efficiency for each fit range, for all scale factors of the ellipse axes against all drift lengths were plotted. Figures (5.7) and (5.8) show examples of these plots for the case that the scale factor of the fit range was one.

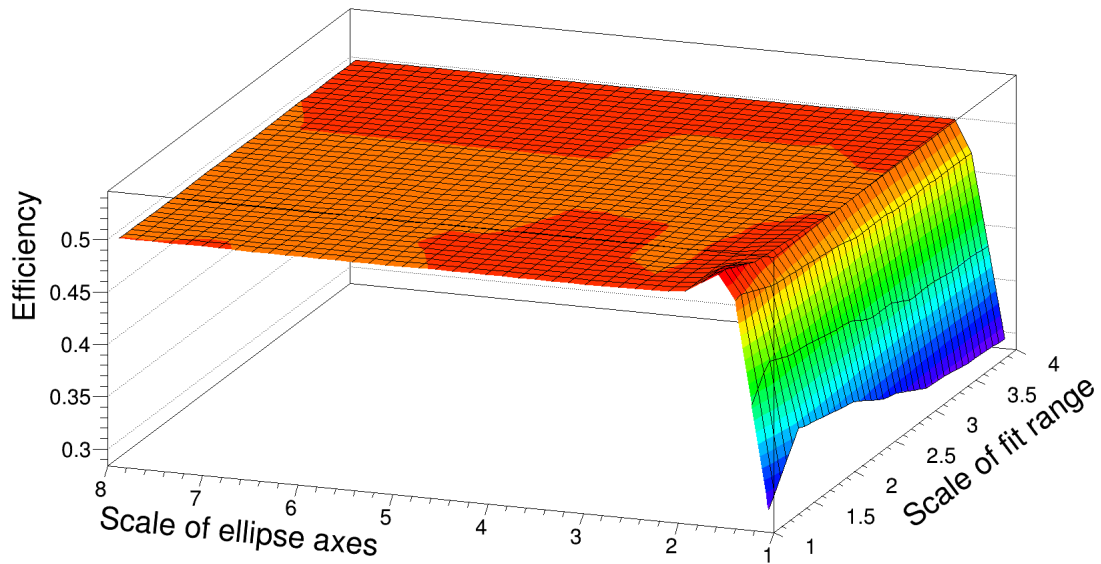


(a)

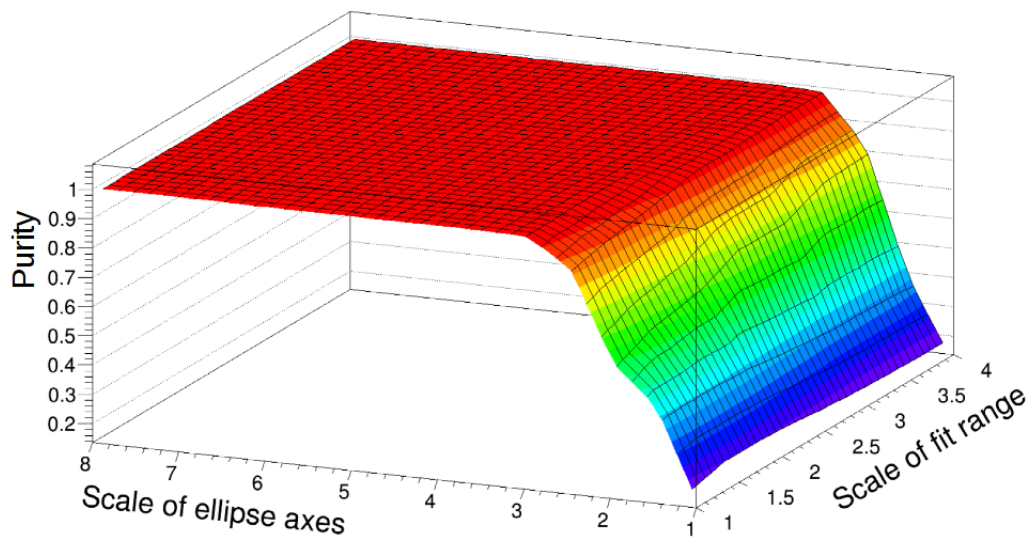


(b)

Figure 5.3: Result for the case that there was 2 mm distance between two tracks in the Y direction and the drift length was 30 mm (a) track efficiency and (b) track purity.

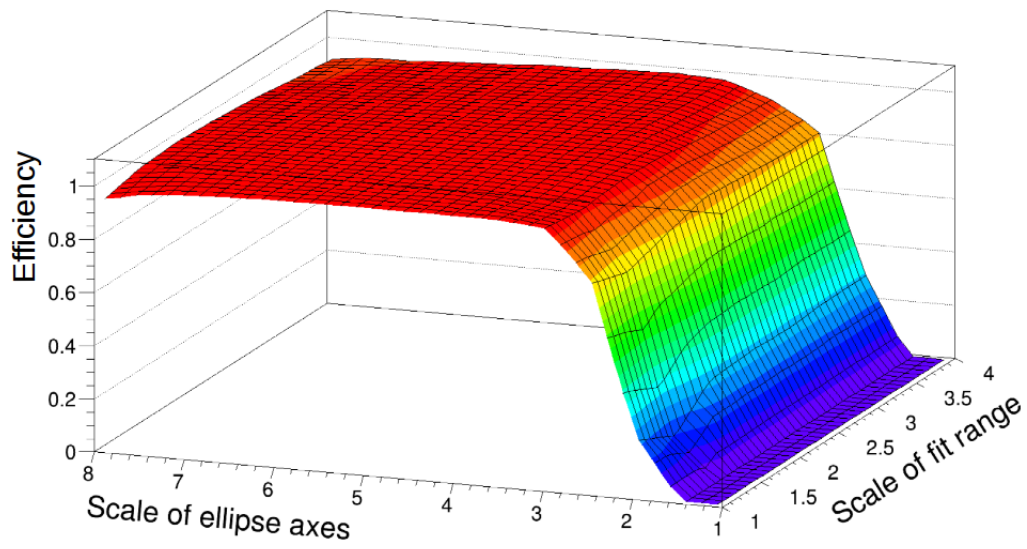


(a)

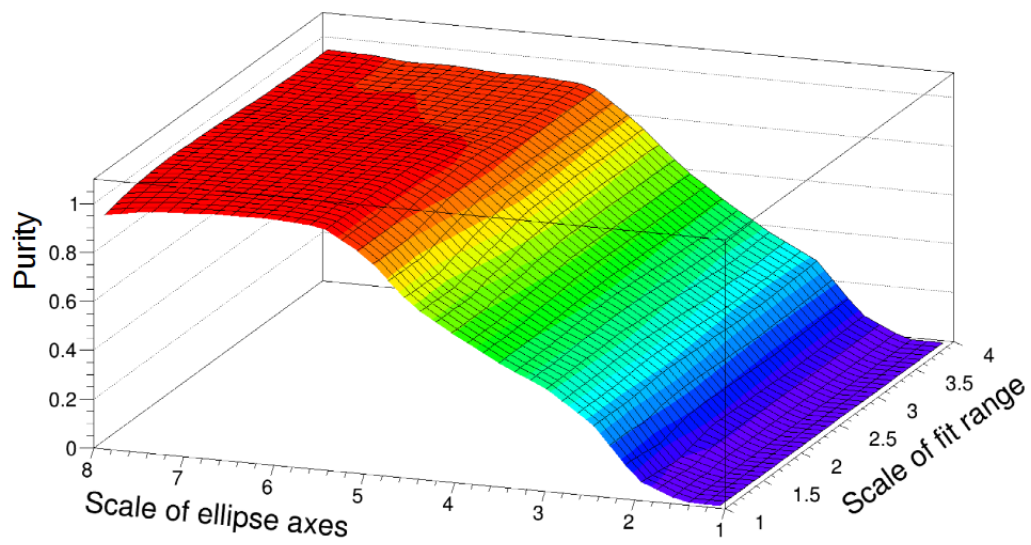


(b)

Figure 5.4: Result for the case that there was 2 mm distance between two tracks in the Y direction and the drift length was 500 mm (a) track efficiency and (b) track purity.

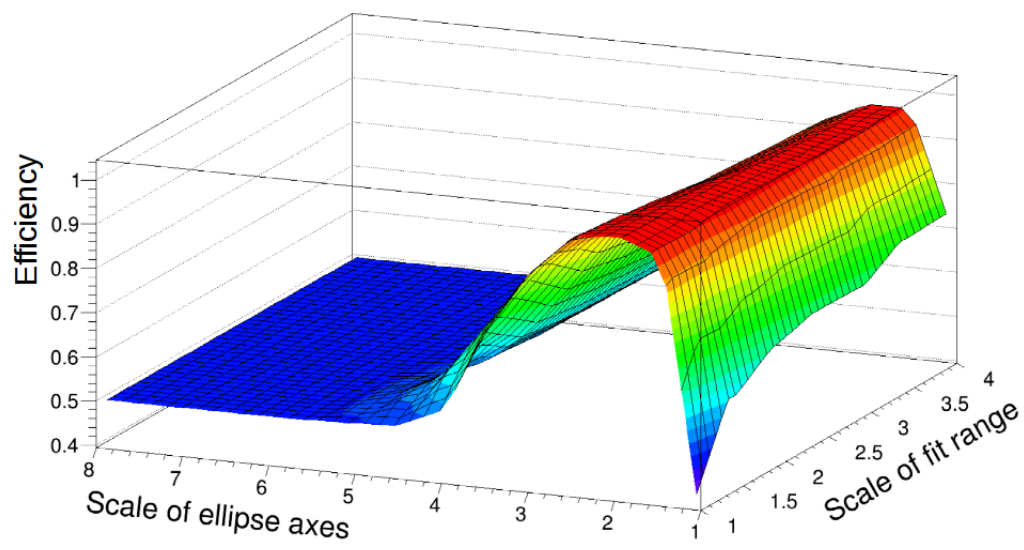


(a)

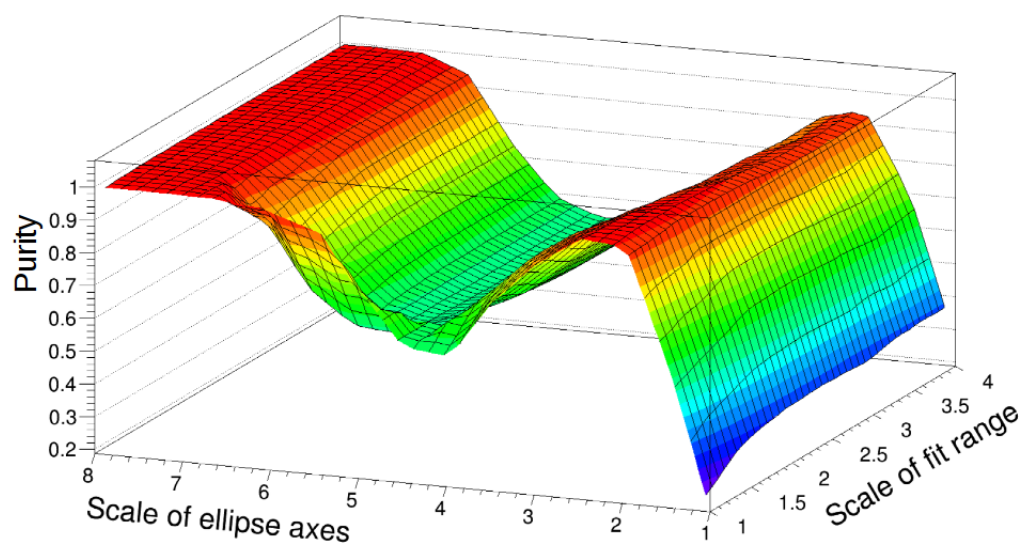


(b)

Figure 5.5: Result for the case that there was 5 mm distance between two tracks in the Y direction and the drift length was 30 mm (a) track efficiency and (b) track purity.

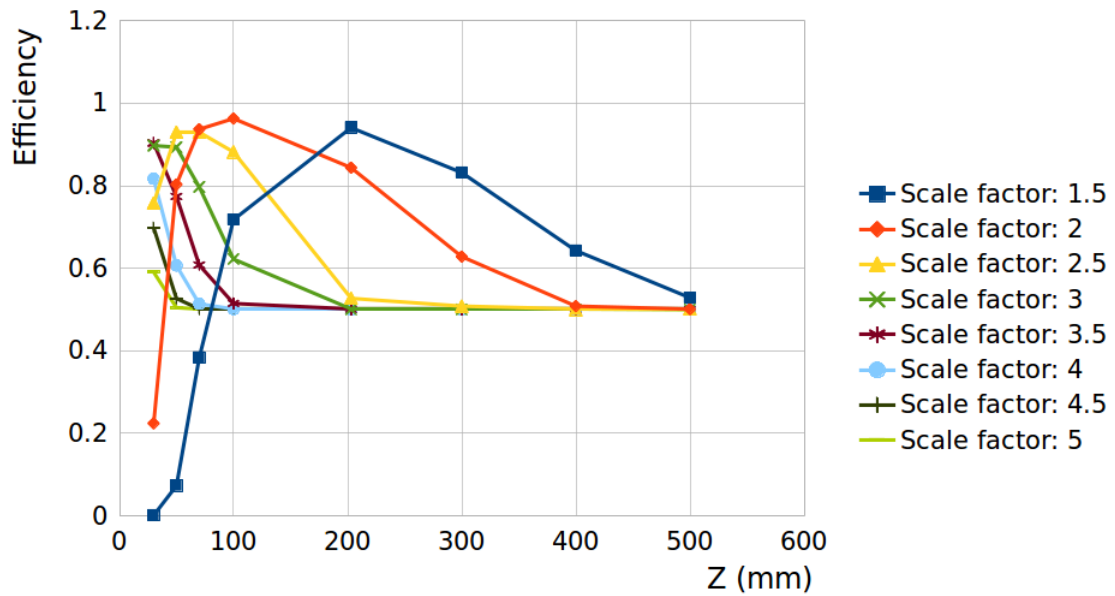


(a)

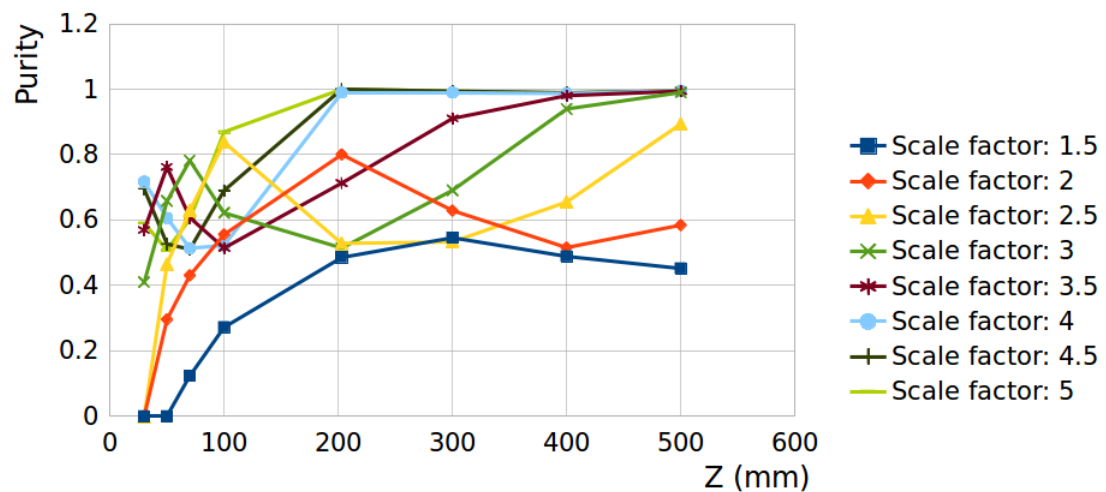


(b)

Figure 5.6: Result for the case that there was 5 mm distance between two tracks in the Y direction and the drift length was 500 mm (a) track efficiency and (b) track purity.

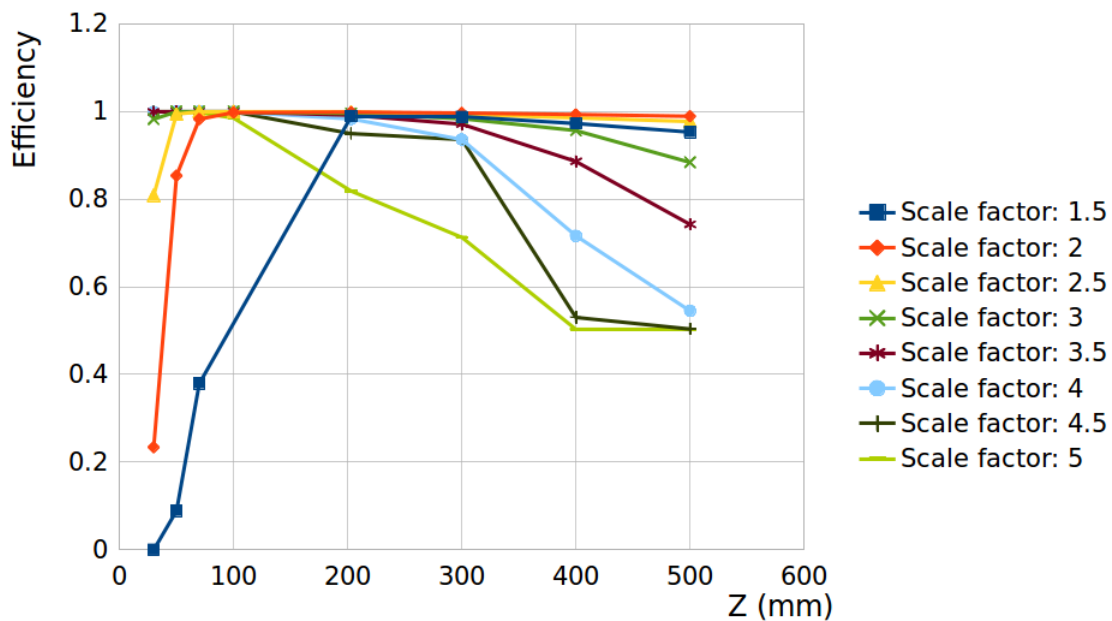


(a)

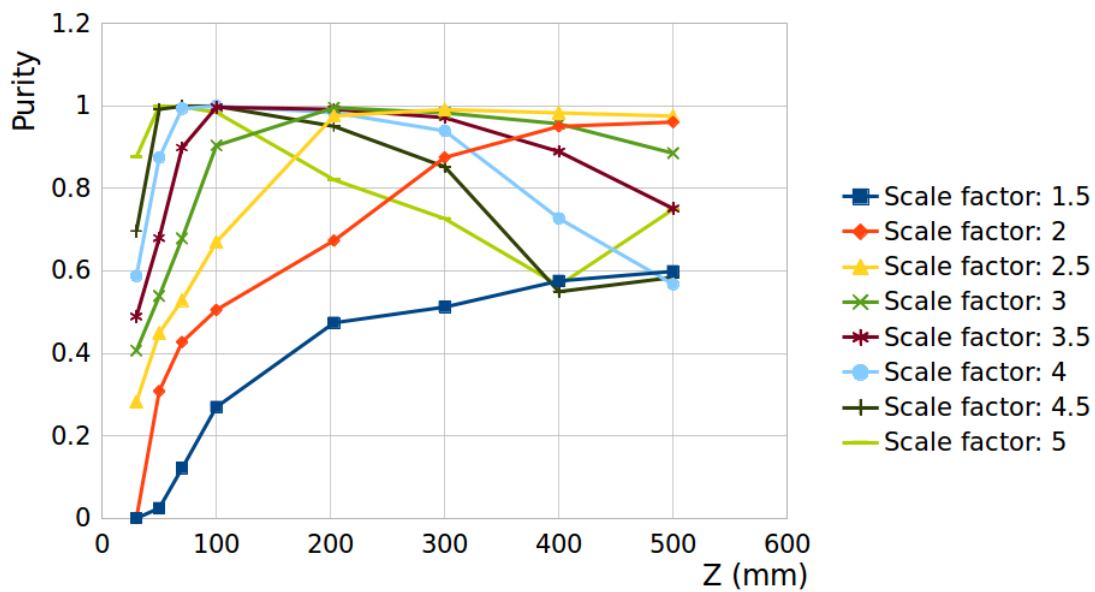


(b)

Figure 5.7: (a) Track efficiency and (b) track purity for the case that the scale factor of the fit range was one. These plots are for the all scale factor of the ellipse axes versus all drift lengths. The distance of two tracks was 2 mm distance in the Y direction. For simplicity, the scale factors of the ellipse axes up to 5 are shown here.



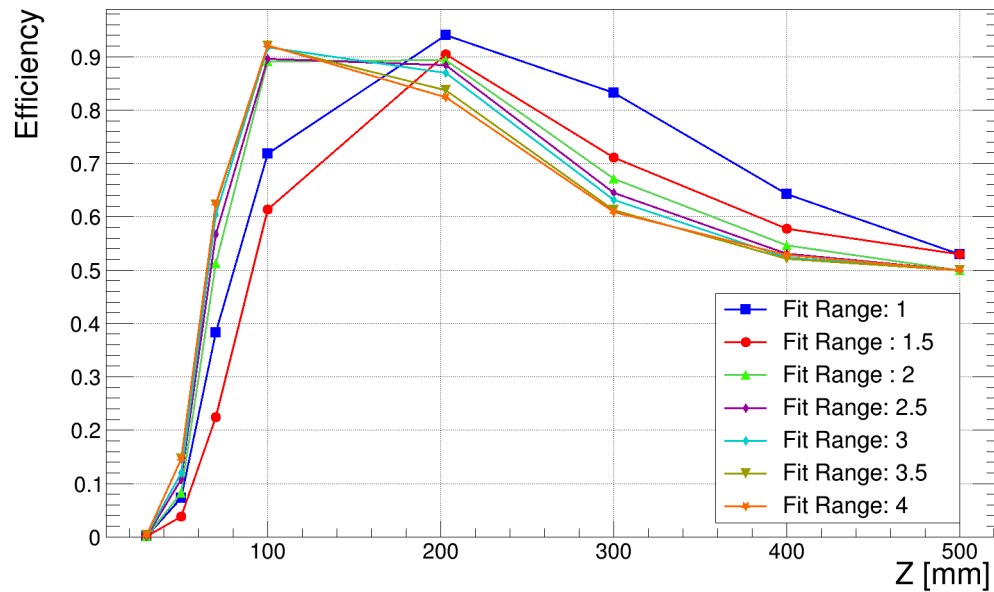
(a)



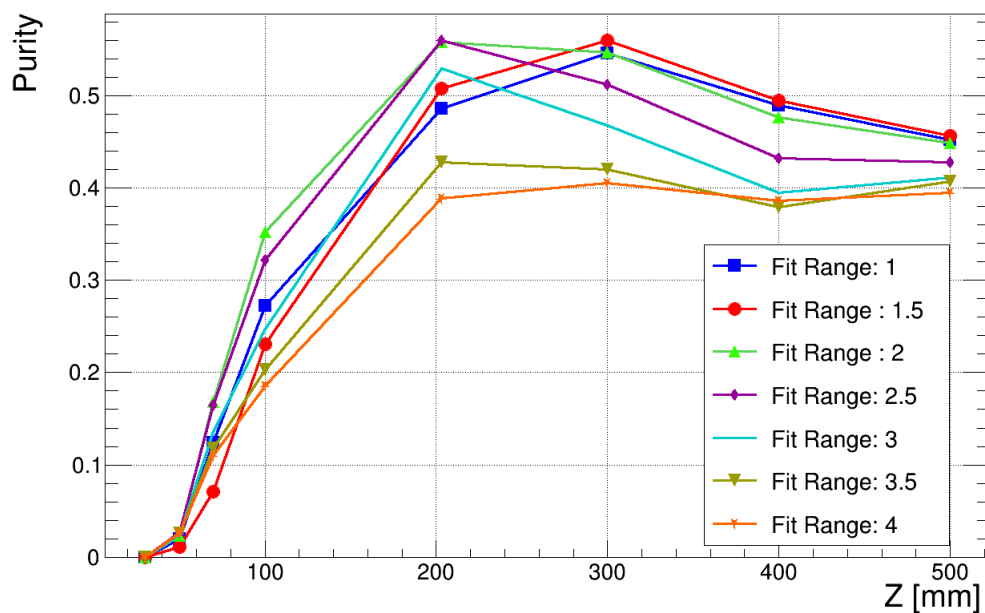
(b)

Figure 5.8: (a) Track efficiency and (b) track purity for the case that the scale factor of the fit range was one. These plots are for the all scale factor of the ellipse axes versus all drift lengths. The distance of two tracks was 5 mm distance in the Y direction. For simplicity, the scale factors of the ellipse axes up to 5 are shown here.

After studying all plots for all fit ranges, it was found that the scale factors 1.5, 2 and 2.5 for the ellipse axes have higher track efficiency compared with other scale factors. The track efficiency and the track purity plots for these three scale factors are presented in appendix B. Figures (5.9) and (5.10) show the plot for scale factor 1.5 for the ellipse axes versus all drift lengths for the case that the distance between two tracks was 2 mm and 5 mm, respectively.

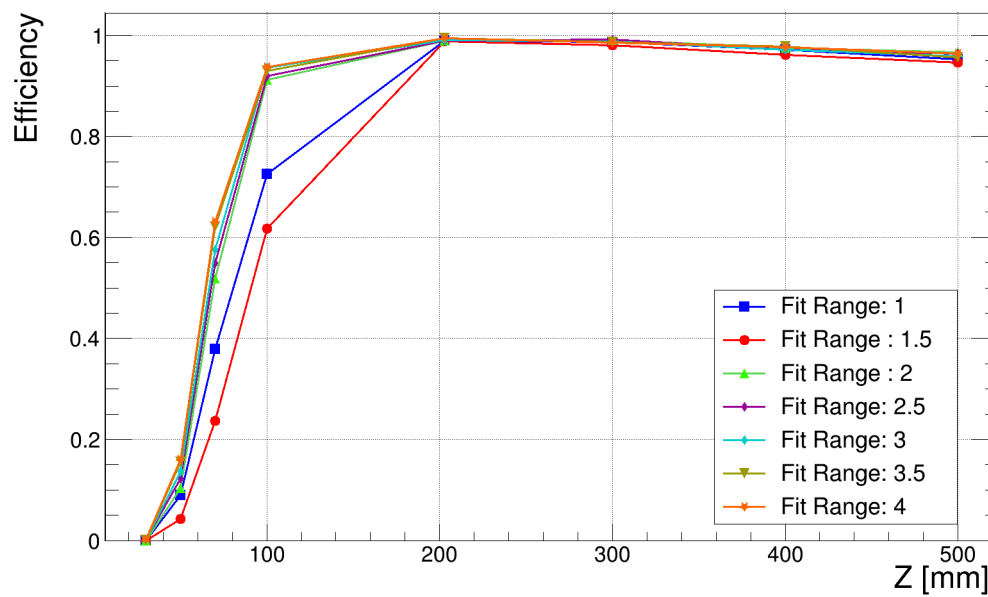


(a)

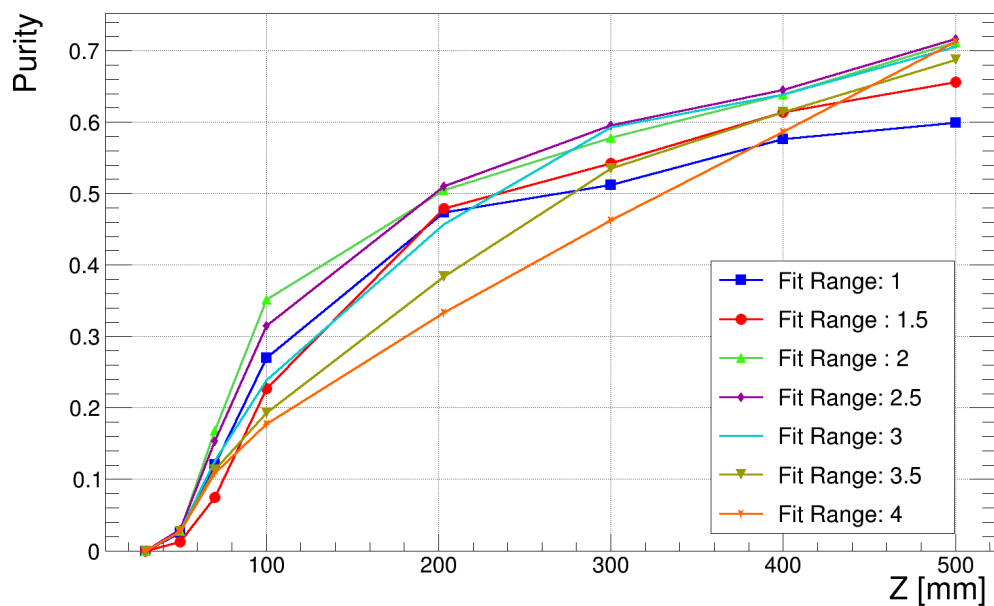


(b)

Figure 5.9: Result for the scale factor 1.5 for the ellipse against all drift lengths and for 2 mm distance between two tracks in the Y direction (a) track efficiency and (b) track purity.



(a)



(b)

Figure 5.10: Result for the scale factor 1.5 for the ellipse against all drift lengths and for 5 mm distance between two tracks in the Y direction (a) track efficiency and (b) track purity.

However, after implementing these factors for real data for the test beam, it was realized that they needed to be modified to have a better result for the test beam data. The quality of the performance of the algorithm for real data was controlled by eye (see chapter 3). Tables (5.4) and (5.5) illustrate the regions and the final scale factors for the fit range and the ellipse axes.

Scale factor of the ellipse	
Drift length [mm]	Value
$Z \leq 50$	3
$50 < Z \leq 100$	2.5
$Z > 100$	2

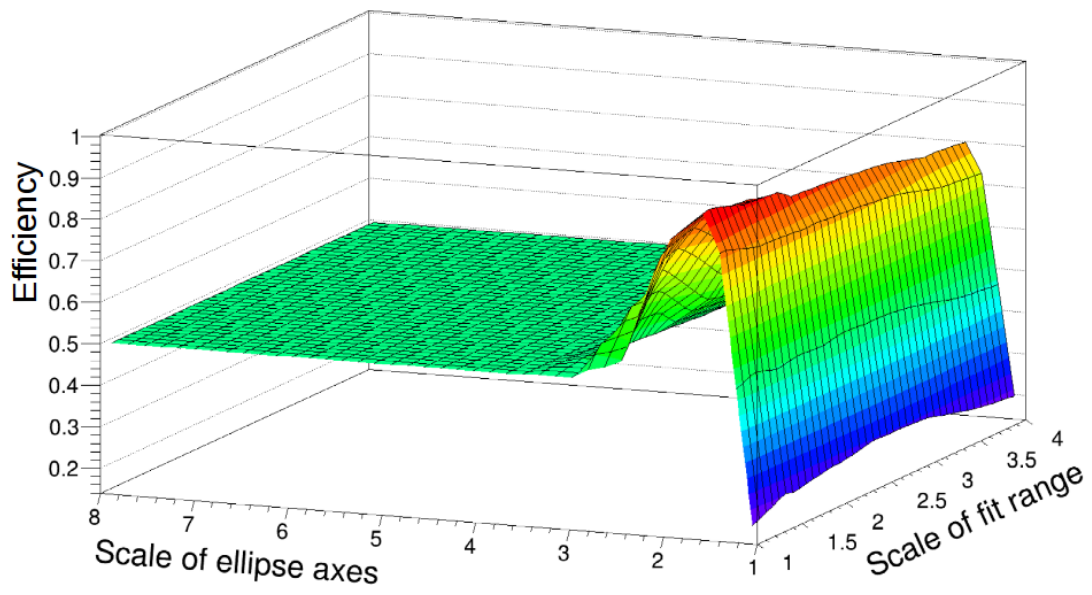
Table 5.4: The scale factor of the ellipse axes in the X-Y plane.

Scale factor of the fit range	
Drift length [mm]	Value
$Z < 50$	2.5
$50 \leq Z \leq 100$	2
$Z > 100$	1

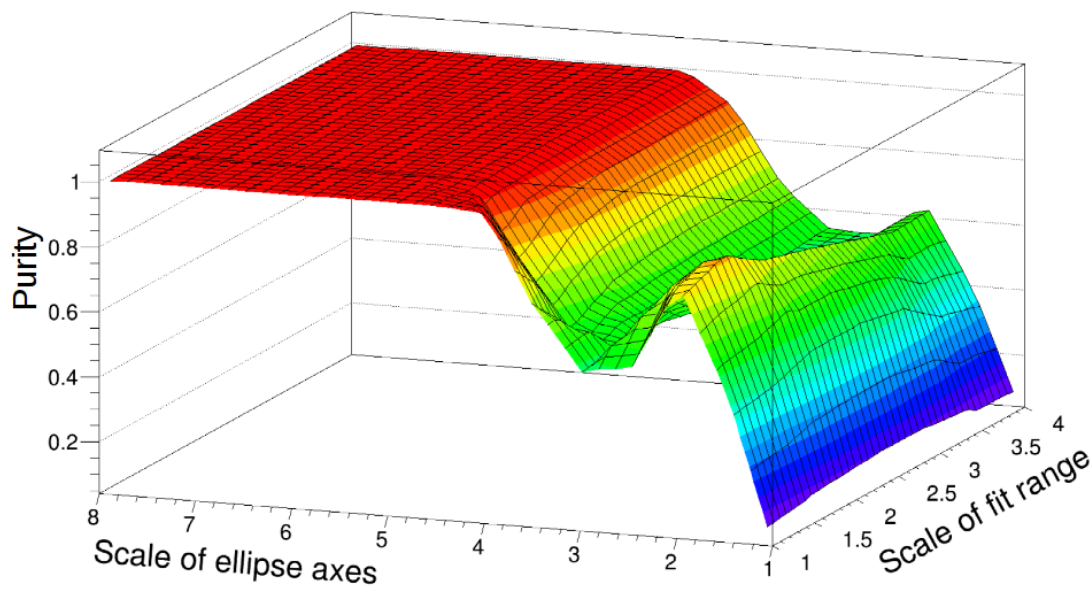
Table 5.5: The scale factor of the fit range in the X-Y plane.

One of the important result of this study is the track efficiency for the 203 mm drift length. Figure (5.11) shows the 3-dimensional the track efficiency and the track purity plots for all scale factors for the fit range and the axes of the ellipse for this drift length and with 2 mm distance between two track in the y-axis. As it can be seen, the algorithm implemented in this thesis is able to separate two tracks with more than 90% efficiency with the scale factor of the ellipse axes around 1.5. Nevertheless, the purity of this scale factor is not so high which means there are also fake tracks. As mentioned before, some of these fake tracks such as ghost tracks can be removed by applying a cut.

According to the ILC TPC characteristics, the double track resolution in the $r - \phi$ plane should be 2 mm or less. With extrapolation of the result gained in this simulation to the full drift length ILC TPC with a 3.5 T magnetic field, it shows this method is promising to fulfill the two track resolution required for ILC TPC. However, this simulation was done for the ideal case that there is no noise in the readout system.



(a)



(b)

Figure 5.11: (a) Track efficiency and (b) track purity for 203 mm drift length and 2 mm distance in the Y direction between two tracks.

5.3.2 Optimization in the S-Z plane

The optimization process was done for the S-Z plane with the same parameters as used in the X-Y plane (table (5.3)). The main difference in this optimization was that two tracks were generated with the same X and Y offset but with a different Z position. First, the distance between two tracks was 5 mm and then it was done with the 10 mm distance in the Z direction. Figure (5.12 - a) shows two tracks with 5 mm distance from each other in the Z direction. The drift length for one track was 30 mm and for another one was 35 mm. Because of the low drift length, the diffusion in the Z direction is low. Thus, two tracks are visible even by eye.

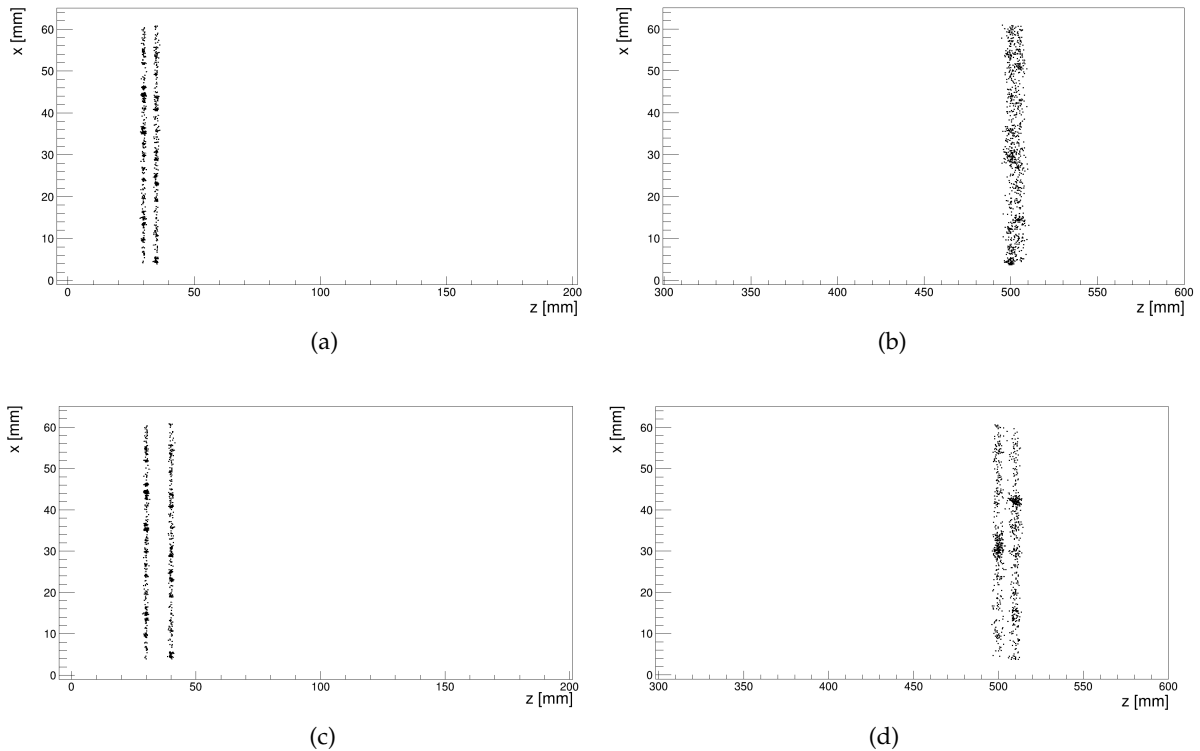


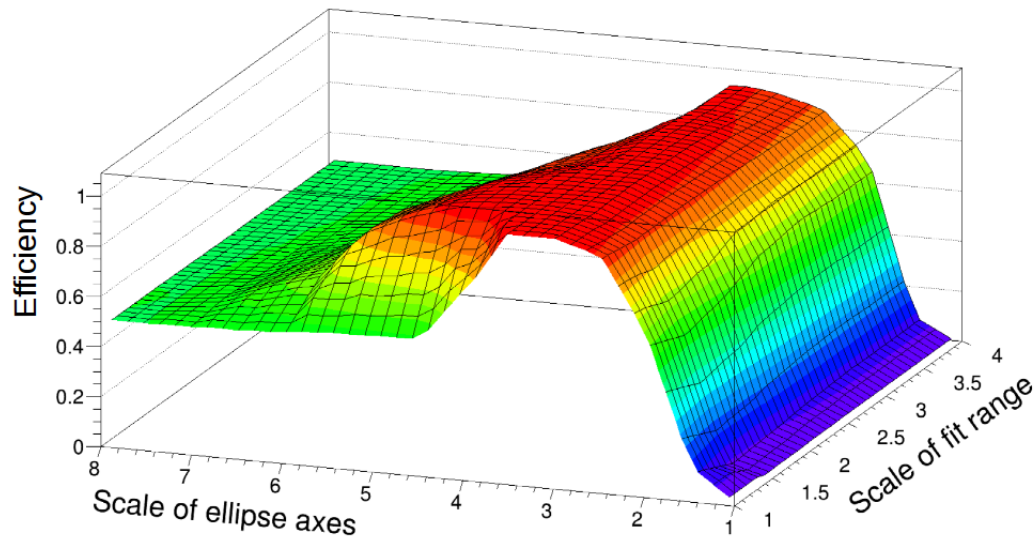
Figure 5.12: Simulation of two tracks (a) with 5 mm distance in the Z direction and 30 mm drift length, (b) with 5 mm distance and 500 mm drift length, (c) with 10 mm distance and 30 mm drift length and (d) with 10 mm distance and 500 mm drift length.

By contrast for the case with a long drift length (here 500 mm shown in figure (5.12 - b)), two tracks are not distinguishable by eye because of the large diffusion. For this case, the track efficiency reduces to about 50% due to that fact that the algorithm can find only one track for most events.

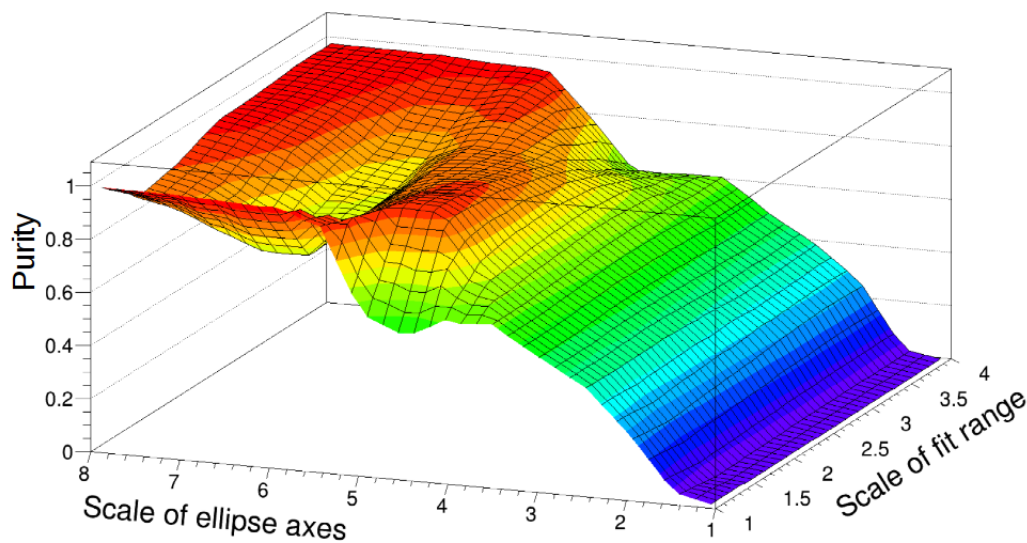
The second case was for two tracks with 10 mm distance from each other. Even for 500 mm drift length two tracks are separated clearly (figure (5.12 - d)). Hence, it is expected that the algorithm would be able to find two tracks. The procedure for finding the optimum scale factor for the fit range and the size of the ellipse axes was as the same as the procedure done for the X-Y plane.

For this optimization, again there are 3-dimensional plots for each drift length for track efficiency and track purity. Here, the x-axis shows the scale factor of the fit range, the same factor is used for σ_{ρ_Z} and σ_{θ} (see chapter 4). Figures (5.13) and (5.14) show the track efficiency and purity for the case that the distance between two tracks are 5 mm with 30 and 500 mm drift length, respectively.

In addition, figures (5.15) and (5.16) illustrate the result for two tracks with 10 mm distance from each other in the Z direction for the lowest and highest drift length.

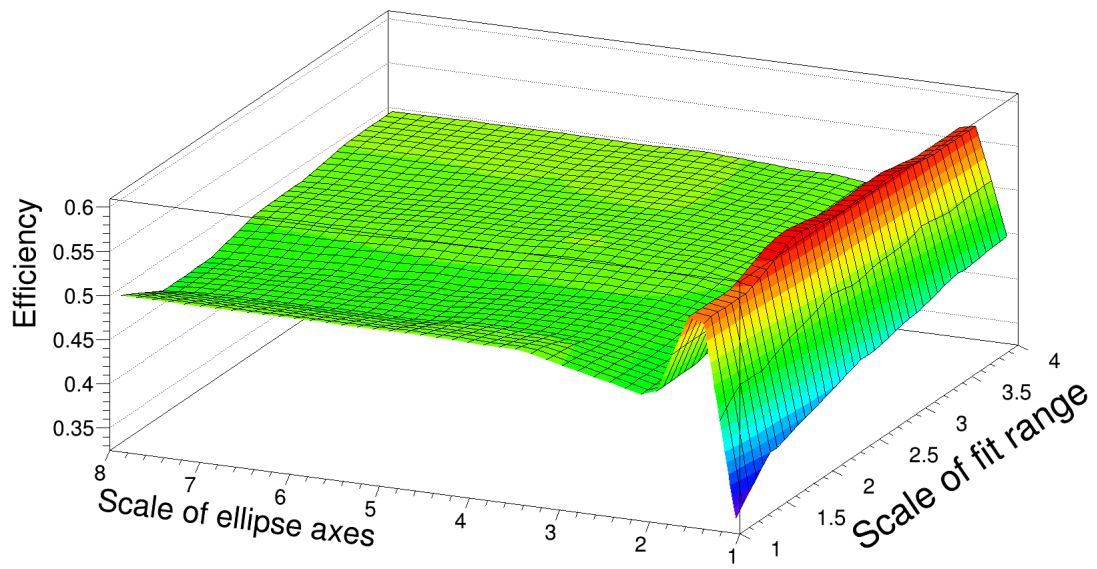


(a)

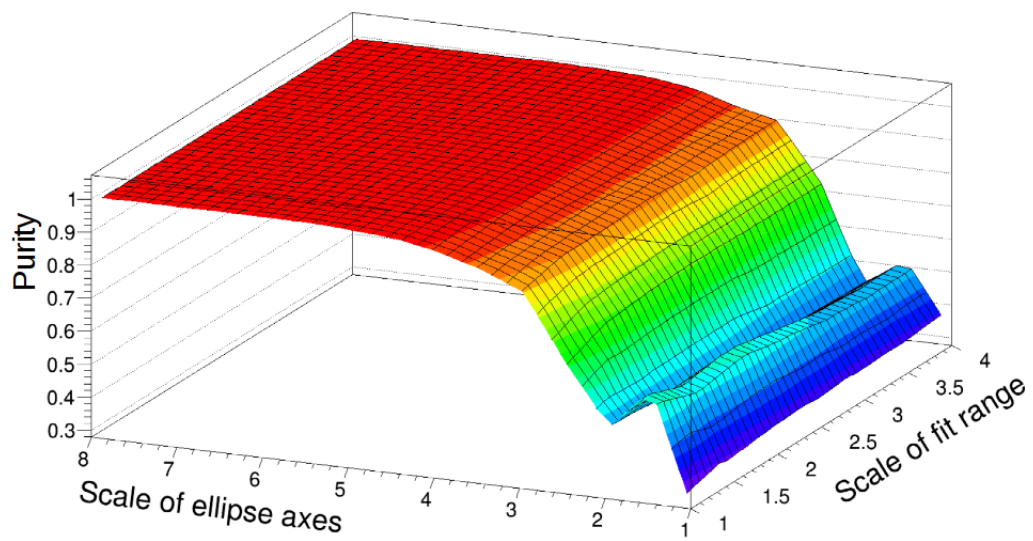


(b)

Figure 5.13: Result for the case that there was 5 mm distance between two tracks in the Z direction and the drift length was 30 mm (a) track efficiency and (b) track purity.

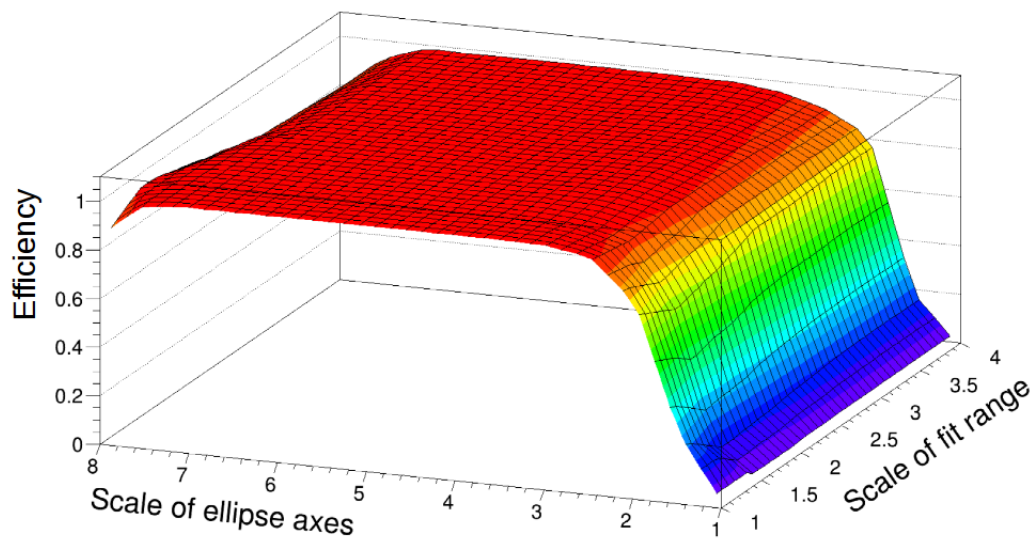


(a)

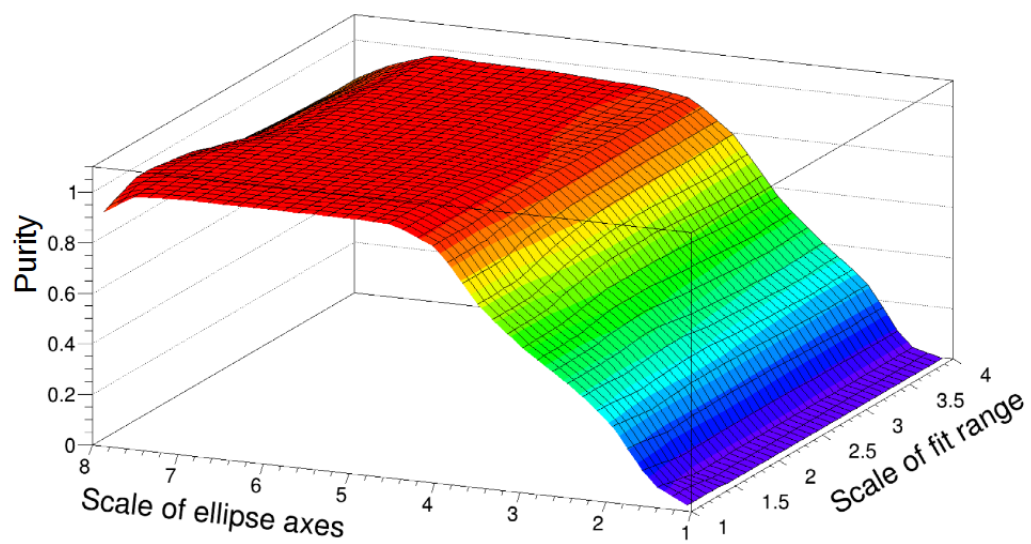


(b)

Figure 5.14: Result for the case that there was 5 mm distance between two tracks in the Z direction and the drift length was 500 mm (a) track efficiency and (b) track purity.

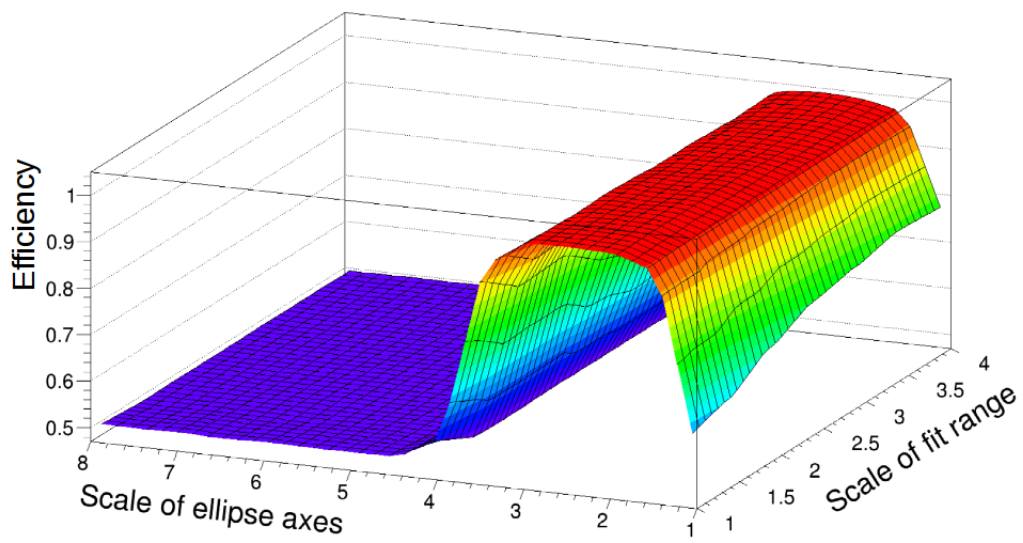


(a)

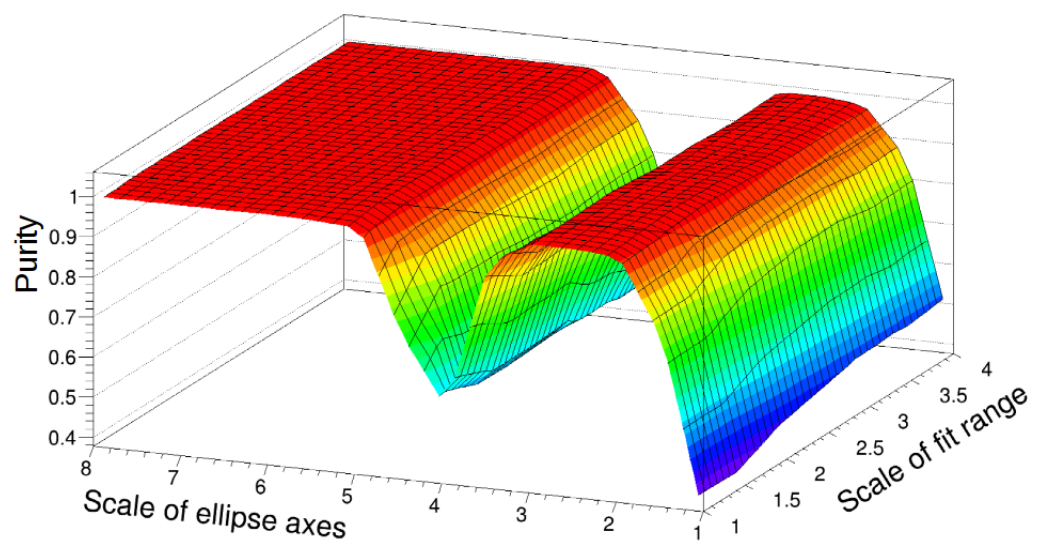


(b)

Figure 5.15: Result for the case that there was 10 mm distance between two tracks in the Z direction and the drift length was 30 mm (a) track efficiency and (b) track purity.



(a)



(b)

Figure 5.16: Result for the case that there was 10 mm distance between two tracks in the Z direction and the drift length was 500 mm (a) track efficiency and (b) track purity.

As similar to the X-Y plane, first the results of the track efficiency for each fit range, for all scale factors of the ellipse axes against all drift lengths were plotted. Figures (5.17) and (5.18) show the track efficiency and purity for fit range one and for all scale factor of ellipse axes versus drift length.

From all plots for all fit range, it was found that the scale factors 1.5, 2, 2.5, 3 and 3.5 (depending on the drift length) for the ellipse axes have higher track efficiency. Hence, for the S-Z plane it is needed to define five regions in order to cover all drift lengths of the LP TPC with high track efficiency.

Plots (5.19) and (5.20) illustrate track efficiency and purity for the case that the scale factor of the ellipse axes was 1.5. One for the first case (5 mm) and one for the second case (10 mm) versus drift length, respectively.

One can see for 500 mm drift length with this scale factor it is possible to reach about 60% track efficiency for the first case. The important point to implement these results for real data is for simulation there is no time walk effect (see chapter 2). Therefore it was necessary to modify these factors based on the real data. However, as mentioned before, the controlling of the track reconstruction performance for real data was done by eye because there is no reference to check it by current algorithm based on the hit information. Tables (5.6) and (5.7) illustrate the five areas and the optimum value for scale factor of fit range and the ellipse axes for the S-Z plane.

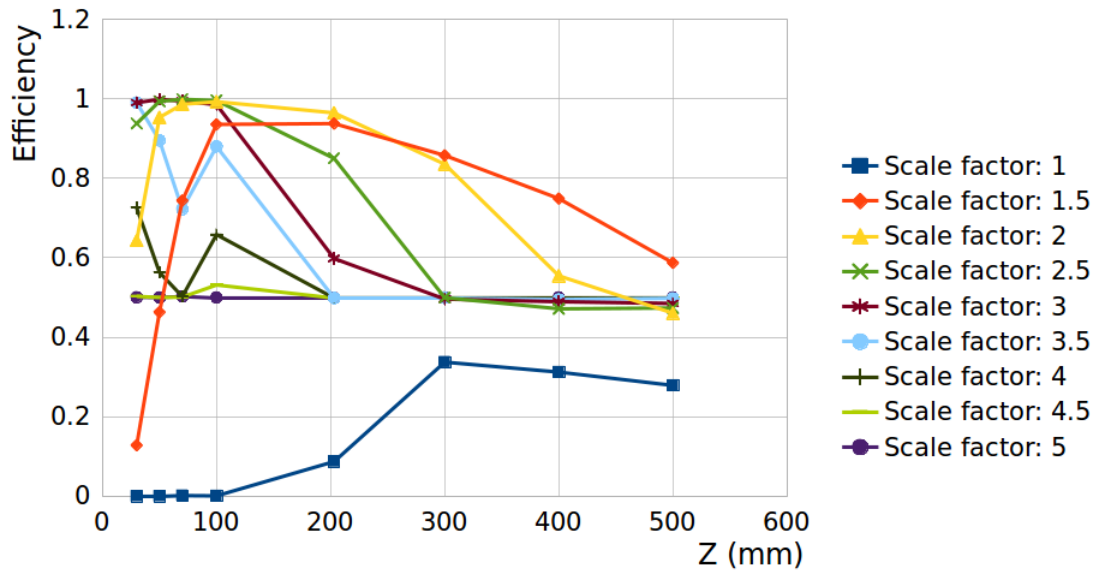
Scale factor of the ellipse	
Drift length [mm]	Value
$Z < 50$	6
$50 \leq Z < 70$	5.5
$70 < Z \leq 100$	5
$100 < Z < 300$	4.5
$Z \geq 300$	4

Table 5.6: The scale factor of the ellipse in the S-Z plane.

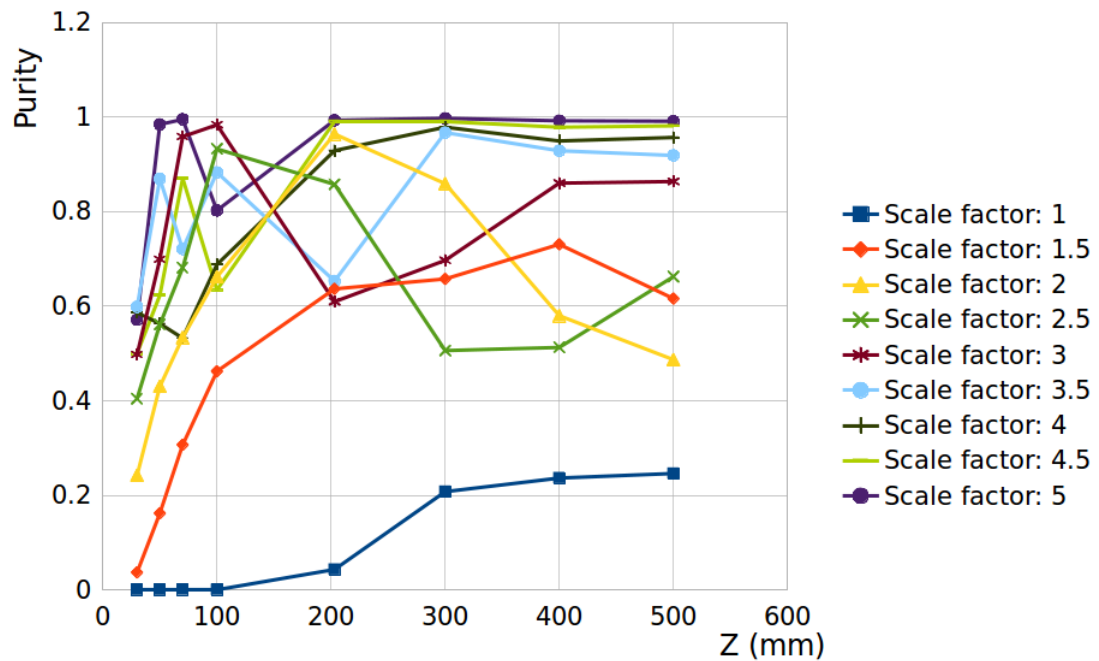
Scale factor of the fit range	
Drift length [mm]	Value
$Z < 50$	1.5
$50 \leq Z \leq 100$	1
$100 < Z < 300$	1.5
$300 \leq Z < 400$	2
$Z \geq 400$	3.5

Table 5.7: The scale factor of the fit range in the S-Z plane.

At the end, all these factors and regions in tables (5.4) and (5.5) for the X-Y plane and in tables (5.6) and (5.7) for the S-Z plane were utilized in **InGridBNDHoughTransformProcessor**. Thus, for each dataset, these parameters are selected by code based on the average of the Z position of all hits on an Octoboard. However, there is an option in this code for whom wants to tune these parameters manually.

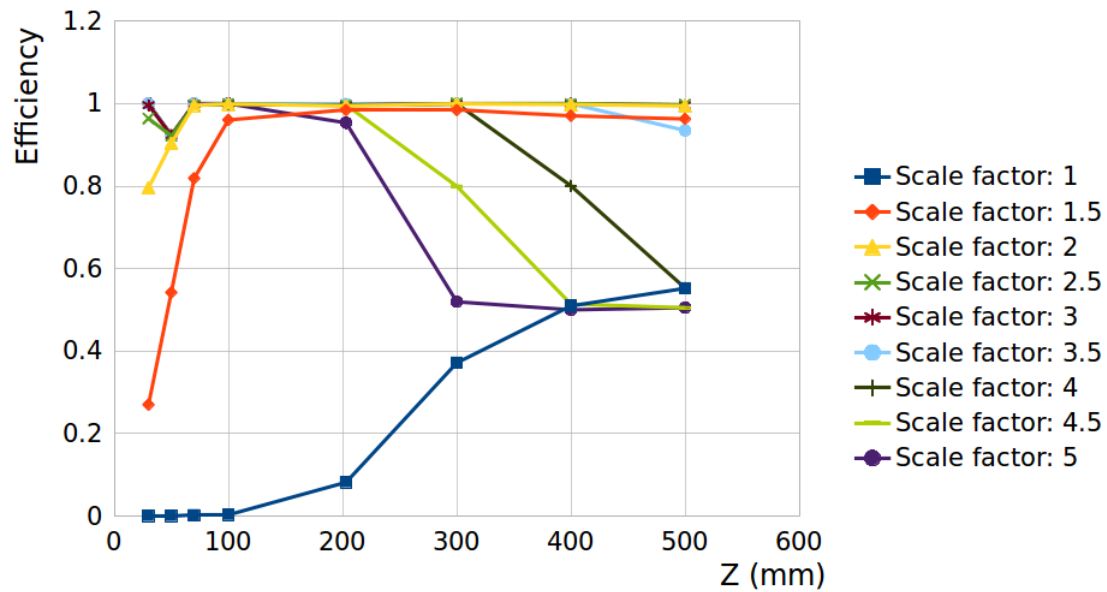


(a)

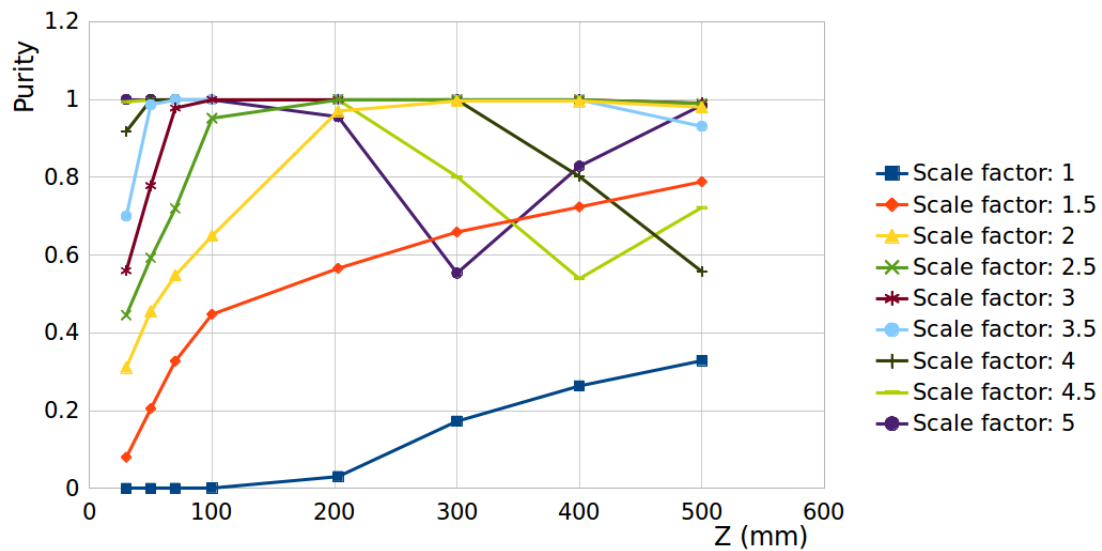


(b)

Figure 5.17: (a) Track efficiency and (b) track purity for the case that the scale factor of the fit range was one. These plots are for the all scale factor of the ellipse axes versus all drift lengths. The distance of two tracks was 5 mm distance in the Z direction. For simplicity, the scale factors of the ellipse axes up to 5 are shown here.

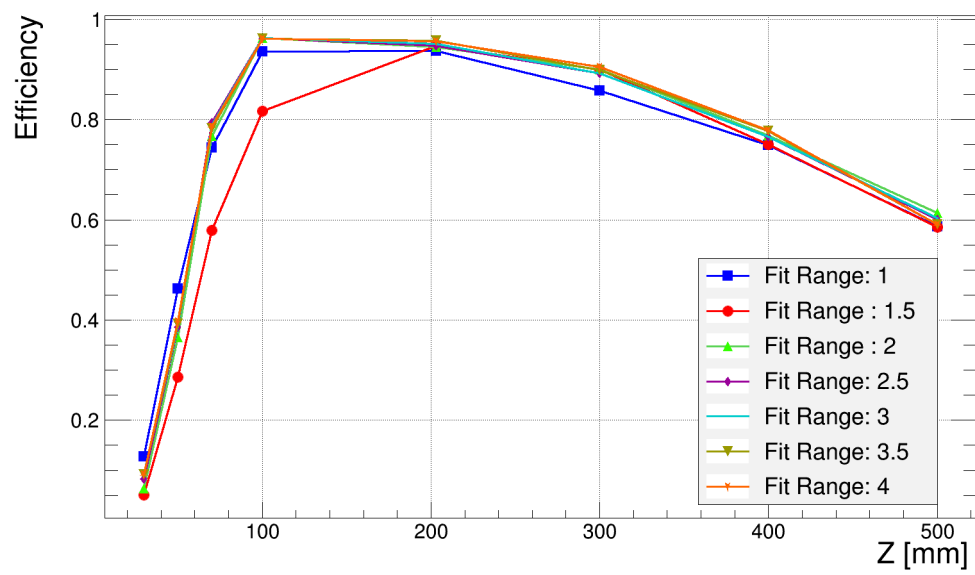


(a)

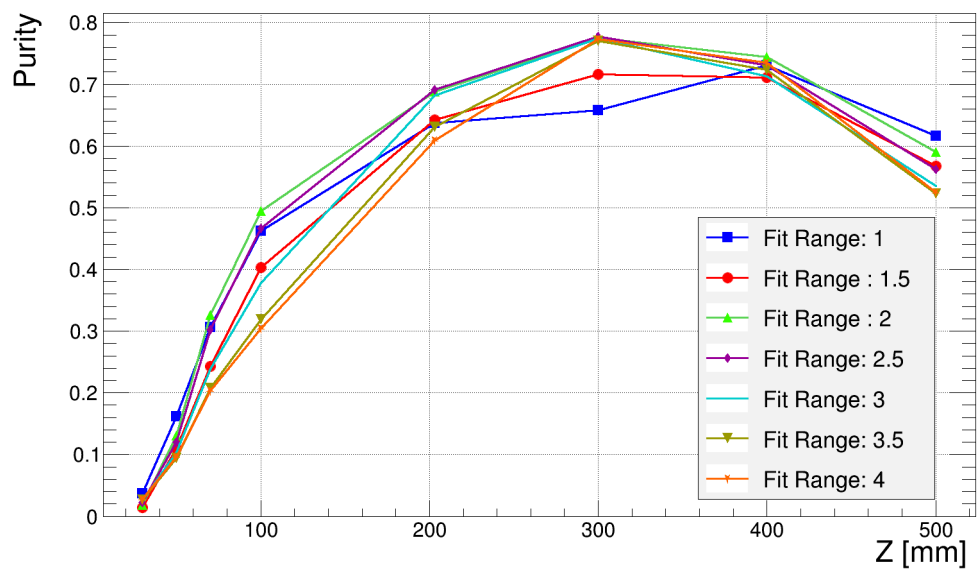


(b)

Figure 5.18: (a) Track efficiency and (b) track purity for the case that the scale factor of the fit range was one. These plots are for the all scale factor of the ellipse axes versus all drift lengths. The distance of two tracks was 10 mm distance in the Z direction. For simplicity, the scale factors of the ellipse axes up to 5 are shown here.

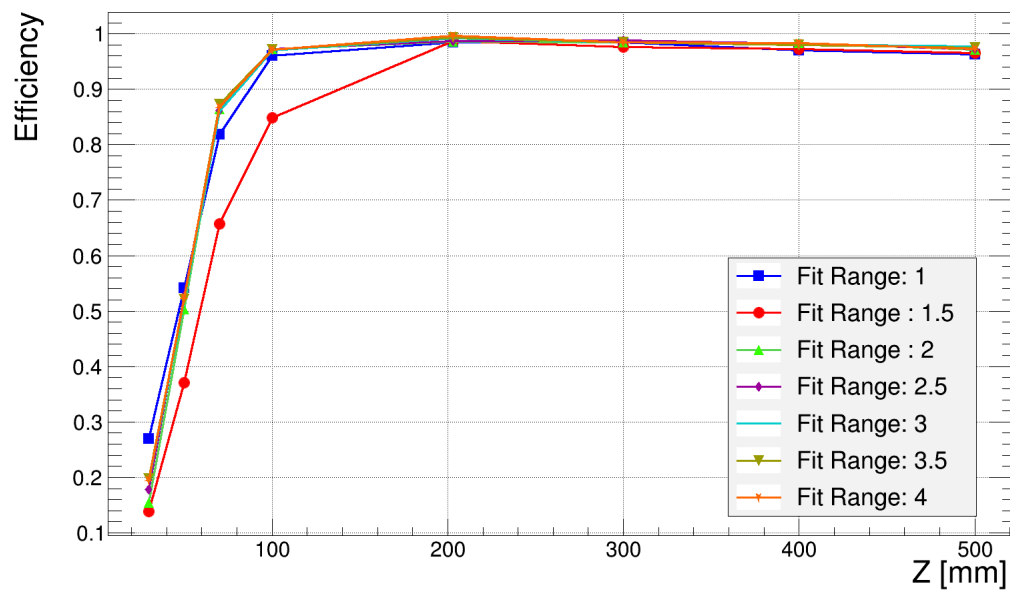


(a)

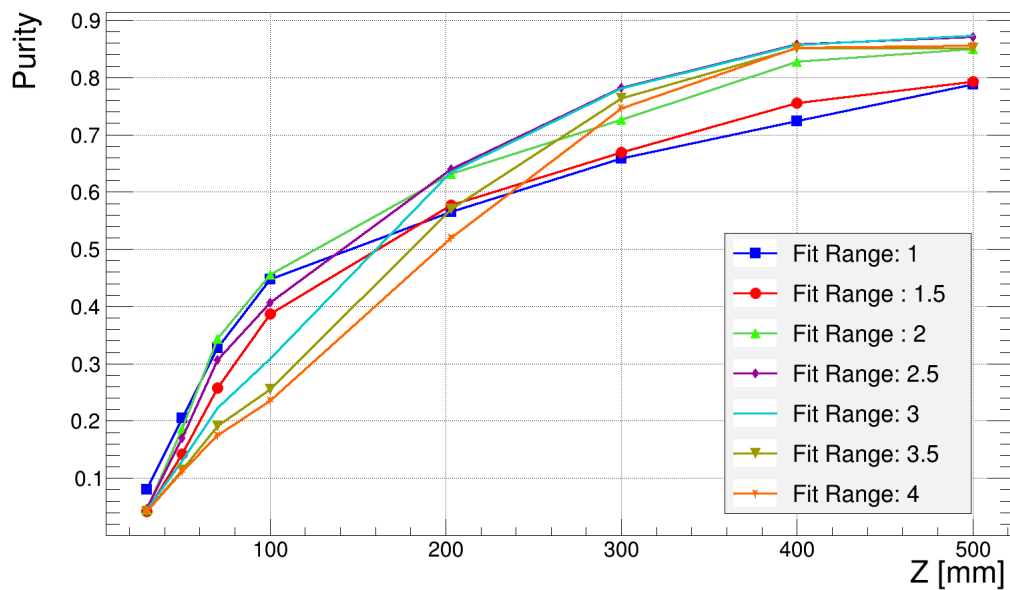


(b)

Figure 5.19: Result for the scale factor 1.5 for the ellipse against all drift lengths and for 5 mm distance between two tracks in the Z direction (a) track efficiency and (b) track purity.



(a)



(b)

Figure 5.20: Result for the scale factor 1.5 for the ellipse against all drift lengths and for 10 mm distance between two tracks in the Z direction (a) track efficiency and (b) track purity.

Chapter 6

Test beam experiment with 160 InGrid chips

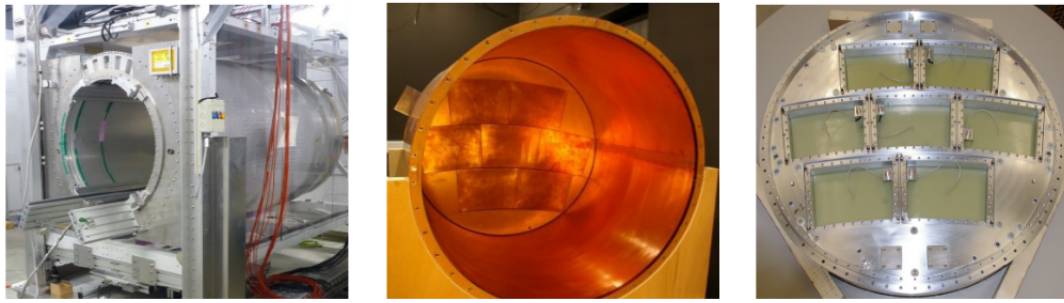
6.1 Test beam 2015

In March and April 2015, a test beam experiment was set up to demonstrate the Pixel-TPC at the LP TPC at DESY. For this experiment, 160 InGrid chips were utilized. In chapter 2 the InGrid was explained in details. In the following section, first the experiment setup and condition will be explained and then the result of the analysis for some package datasets will be presented. Some selected events of these package datasets are shown in appendix C.

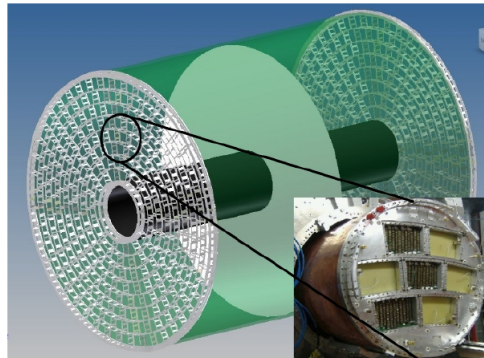
6.1.1 The large prototype TPC (LP TPC) at DESY

The LCTPC collaboration has operated the large prototype TPC (LP TPC) since the end of 2008 as a prototype for the ILD TPC [81]. It is installed in a 1 T magnet called PCMAG and placed at a test beam area T24 at the DESY II accelerator. Both the TPC and the magnet are mounted in a movable stage. The LP TPC field cage has a diameter of 75 cm and a length of 56 cm (figure (6.1 - a)). The wall material budget is $1.3\% X_0$. The end-plate of the LP TPC is a cut out of the final ILD TPC and it is able to host seven modules with the size of $22 \times 17\text{cm}^2$. In addition, The experiment can be remotely controlled beside the area.

DESY II has a circumference of about 292.8 m. It can provide a beam of electrons and positrons. Every single bunch in this accelerator includes about 3×10^{10} electrons or positrons with an energy from 450 MeV as injection energy up to 6 GeV [82]. Figure (6.2) shows a sketch of the generation of electrons for the test beam area. As it can be seen, first a Bremsstrahlung beam is generated by a $10 \mu\text{m}$ thin carbon fibre as a primary target in DESYII and then a secondary target, which is copper or aluminium, is used for electron-positron pair production from Bremsstrahlung beam. The particles with the desired energy can be selected to pass through a collimator by tuning a magnet.



(a)



(b)

Figure 6.1: (a) Infrastructure for the test beam, LP TPC and end-plate from DESY group. (b) Schematic of the ILD TPC and the end-plate of LP TPC [56]

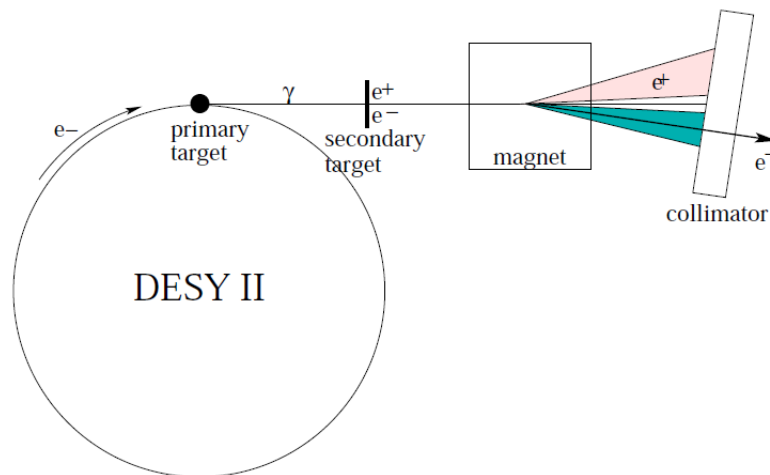


Figure 6.2: A sketch of the generation of electrons and positrons in DESY II and injection of electrons into the test beam area [82].

6.1.2 Module arrangement

For this experiment, three modules were arranged in a way that it was possible to measure the maximum length (around 50 cm) of tracks. The two outer modules had four Octoboards each, ordered in one column and the central module had twelve Octoboards. The orientation of the modules for most experiments was set up such that it was parallel to the beam axis and therefore the beam passes through most of the Octoboards. Figure (6.3) shows the CAD drawing of the LP end-plate with three InGrid modules [56].

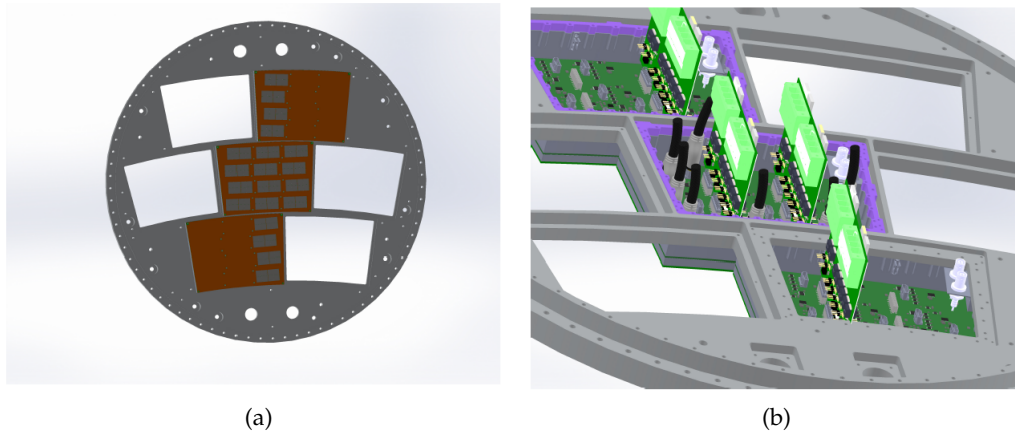


Figure 6.3: CAD drawing of the LP TPC end-plate (a) three modules from inside view (b) the same three modules from outside view showing the Intermediate board, low voltage boards and HDMI cables [56]

Figure (6.4) shows the status of the InGrid chips during data taking. Among the 160 InGrids, seven chips did not show any events because of an electronic problem (red), four chips were not connected (black) and nine of them were noisy (blue) at the beginning of the test beam. Later some other chips became noisy which was solved by changing the threshold.

6.1.3 Conditions and run parameters

The T2K gas (95 % Ar, 3 % CF₄ and 2 % iC₄H₁₀) was the gas mixture used in the experiment. It was flushed at a flow of 40 l/h. During data taking all environmental conditions including temperature, pressure, and contaminations of the gas mixture were monitored. This information is needed for the analysis.

For most runs, for all chips, TOA mode was used in order to measure the arrival time of charge. Except for one package dataset with 16.1 μ s, for all runs, the shutter was opened for 13.8 μ s with a sampling frequency of 40 MHz or 80 MHz. For analysis, 238 ns time is taken into account as a difference between the trigger signal and the shutter opening at the modules. Four scintillators were placed at the beam entrance to the test beam area. A coincident signal of all four scintillators was used as a trigger. More information about the technical setup of all chips are available in chapter 8 of [56].

For cooling system the water was used. There were twelve temperature sensors for monitoring the temperature on the three modules. The water distribution was in such a way that the central module received twice the amount of flux than the two outer modules.

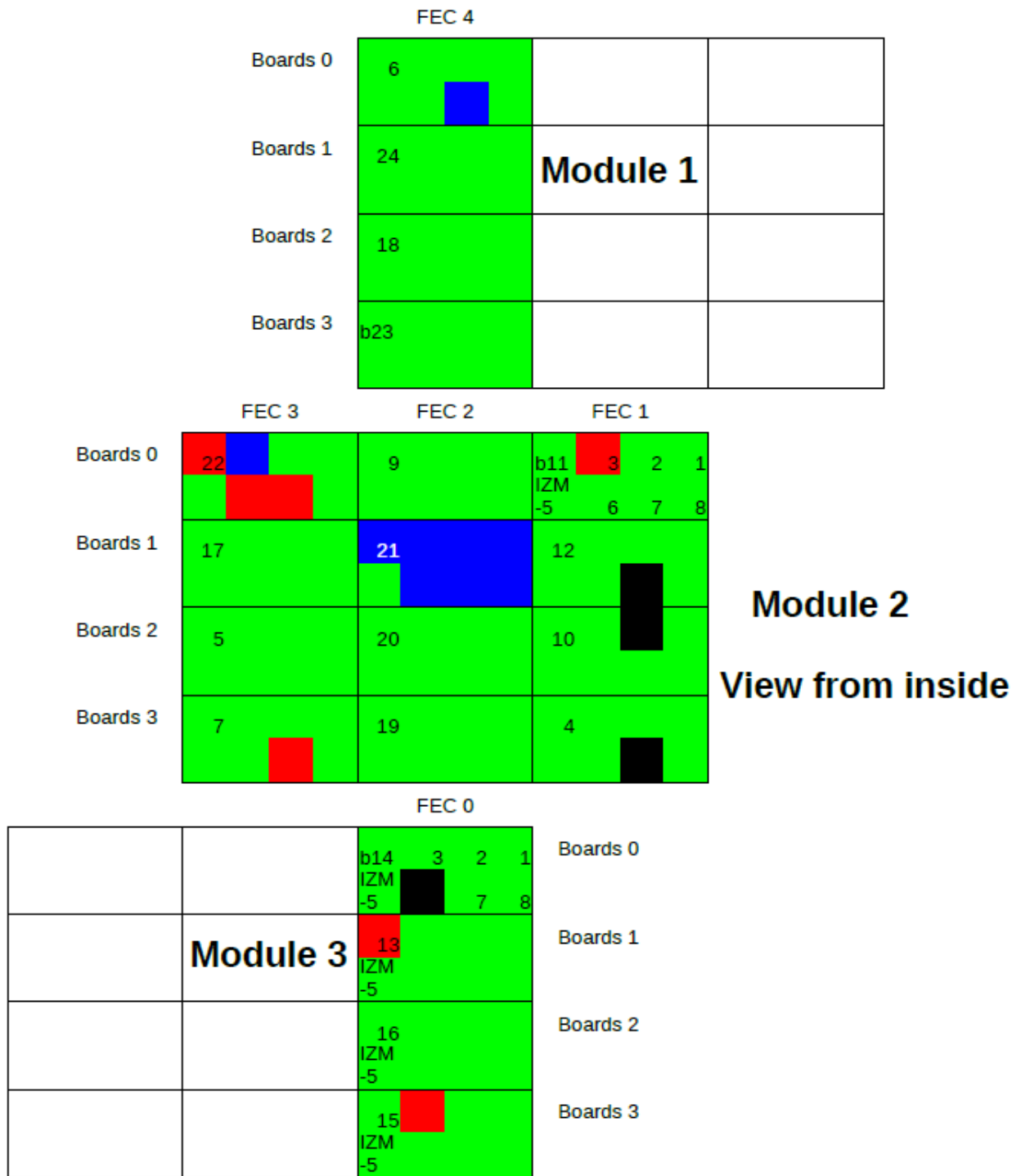


Figure 6.4: The status of Octoboards during data taking. The red chips did not show any events due to an electronic problem. The blue chips were noisy, and the black chips were not connected. All Octoboards are made of InGrid chips from the IZM-5 production [56].

In total 190 runs with different parameters were recorded. Each parameter was based on the physics program for this experiment. The series of runs for each of these parameters was called scan. They were numbered from 28 to 215. The parameters were based on the position of the LP TPC stage with respect to the beam, magnetic field, sample frequency, drift field strength and the running mode of InGrid pixel. All scans were categorized as follow:

Z-scan: the TPC were moved in the range of -130 mm to 330 mm along the z-axis. There was a limitation up to 465 mm as the longest distance of the beam to the end-plate because the beam hits the anode at almost -135 mm. However, the length of the TPC is 567.6 mm. In total there were six package datasets for Z-scan, illustrated in table (6.1).

Z-scan					
Run	Energy [GeV]	E [V/cm]	Sampling Frequency [MHz]	Shutter [μ s]	B [T]
51-59	5	230	40	13.8	0
60-72	5	130	40	13.8	0
76-89*	5.4	230	40	13.8	1
90-105	5.4	230	40	13.8	0
121-135*	5.2	130	40	16.1	1
178-190*	5	230	80	13.8	1

Table 6.1: Parameters of six package datasets for the Z-scan. The package datasets with the star have been used for analysis for this thesis.

From table (6.1), three package datasets are identified by a star. These are the runs that have been used for analysis for this thesis. The main reason to select these runs was they were done in a magnetic field. As previously mentioned, the main goal of this study was to find an algorithm to be able to find tracks with different curvature in a magnetic field, therefore study on these runs was in priority for this thesis. In addition, the magnetic field reduces the transverse spatial resolution, hence this case was also interesting to study.

θ -scan: the TPC was rotated around its vertical axis between -40° to 15° .

ϕ -scan: the TPC in the magnet was rotated around the z-axis between -90° to 9° , where 4° was a rotation such that the beam passed through all three modules.

H-scan: the TPC were lifted and lowered between 0 mm to 65 mm. The optimal height was 30 mm where the beam passed through all three modules.

P-scan*: the energy of the incoming particle was changed between 1 to 5 GeV. These package runs were done with a 1 T magnetic field and it was another case for study for this thesis. With different energy the curvature of tracks are different and therefore P-scan was the best case to check the performance of the algorithm for real data.

Voltage-scan: the high voltage for the InGrid was changed from 280 V to 350 V. For this scan, the Pixels were set to TOT mode in order to measure the gas gain.

Each run includes 10 000 frames (events) and took around 40 min. The size of the raw data for each run was about 4.8 GB which is dominated by the noisy chips. In addition, there were some runs which were taken during night for cosmic rays. Moreover, all data was taken in zero-suppressed mode.

6.1.4 Pipeline of data analysis

In order to do the physics analysis such as momentum resolution, and also to evaluate the performance of the InGrid chips, there are several preprocessing steps needed to clean, convert and prepare the test beam data. All these preprocessors are already available in the MarlinTPC framework. The final form of the data contains the reconstructed tracks. Figure (6.5) shows the pipeline of the preparation of the data for analysis.

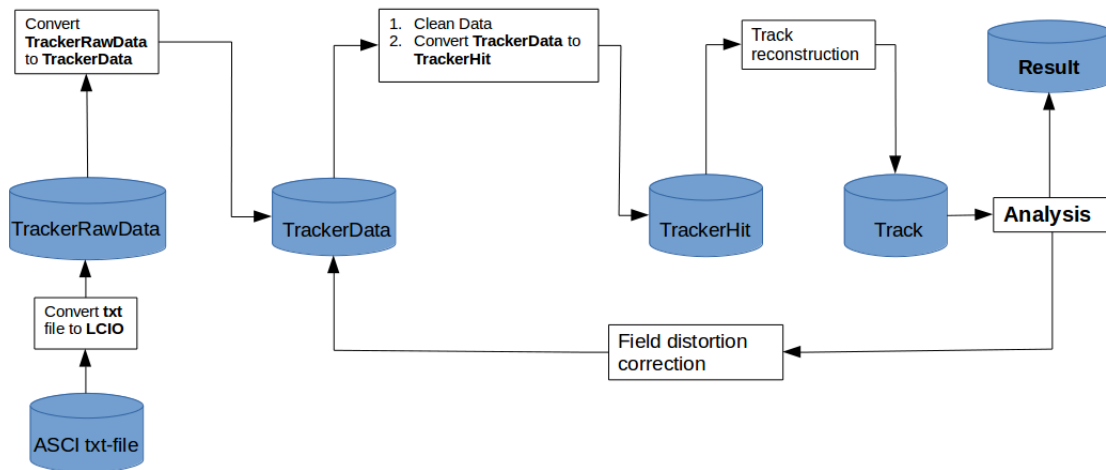


Figure 6.5: The pipeline of the physics analysis for the test beam data.

The first preprocessing step is to convert the ASCII txt-file, which includes the raw data taken during the test beam, to LCIO format required by the MarlinTPC framework. This conversion is done by **TimePixXYReaderProcessor** and it saves data as a data type called **TrackerRawData**[42]. During the test beam and at the end, some corrections were done to assign data to the correct chips [56].

For the analysis, MarlinTPC requires the mode and status map for all chips. The mode map is an LCIO file which saves the information about the mode of each pixel for each run. For those runs that were done in TOA mode, the **TimePix-ModeMapCreatorProcessor** generates a uniform mode map in this mode for all pixels.

The status of each pixel is stored by **TimePixMaskCreatorProcessor** in a LCIO file, which identifies the intact, dead or noisy pixels. For the first step, all pixels were set to intact. The status map is very important for the cleaning process. Because from time to time different defects happened e.g. chips became noisy or died, therefore each run requires its own status map.

There were three main sources for noise. The first reason was the setting of the threshold for 160 chips which could not be accurate. Another reason was some chips had several dead columns and the last reason was some chips were completely noisy. The last two issues were the dominant source of noise for all runs.

The cleaning procedure was done by implementing the occupancy map for each run. The occupancy map is a 2D histogram which shows how often the pixel was hit in the run. In this histogram, those pixels that have a high value of entries are assigned as noisy. Figure (6.6) shows an example for run 83. It can be seen in this figure that there are some pixels in red color which are noisy pixels. By applying a cut, the noisy and dead pixels were identified and rejected from other pixels.

For cleaning data and removing dead and noisy pixels, first the **TrackerRawData** is converted to **TrackerData** [42] by **TrackerRawDataToDataConverterProcessor** which is required by **TimePixOccupancyProcessor**. For running these processors, MarlinTPC needs to access to the mode and status map. As mentioned before, for the first step, all pixels are set to intact.

TimePixOccupancyProcessor is the processor which plots occupancy spectrum and also using cut to identify the noisy and dead pixels. Base on the cut, it generates a log file including all rejected pixels. In addition, the empty chips are also noted in the log file. This log file is used as an input file for **TimePixMaskCreatorProcessor** to generate a new status map but this time including information about dead, noisy and intact pixels.

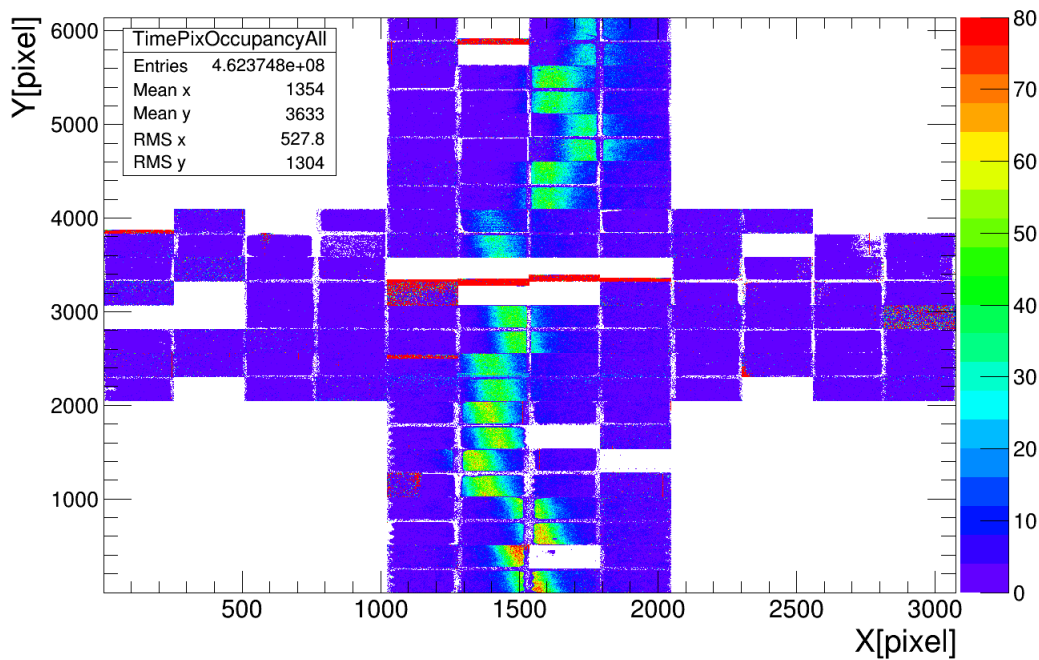


Figure 6.6: Occupancy plot for run 83 before implementing cut. The maximum number was set to 80 in order for the beam profile to be visible.

The second inspection of the data quality was done using the TOA spectrum of the cleaned data. In the previous step of cleaning, the pixels, activated more than a criterion (here 80) in the run, were rejected. However, still, there were some high count pixels. Some of them were dead pixels, which were activated rarely. The others were for a few chips in some single events which generated by a malfunction of the external effects or the readout system [56]. These high count pixels and events are selected and noted by the **PixelSpectrumProcessor** in a log file. It is done based on the TOA spectrum [56]. This log file and the previous one from occupancy process were implemented by **TimePixMaskCreatorProcessor** to generate a new status map. In addition, the processor called **TimePixThrowEventOrChipProcessor** uses the log file from **PixelSpectrumProcessor** to clean chips or events with high count pixels. At the end of these processors, the output is a **TrackerData** called **TimePix-CleanedThrowData** which is used for the next step.

Although these processors are used to clean data, still there is noise in the data. The main reason is the value of the selected cut in each processor. It was tried to

use the optimum number for them however it does not mean that all noise can be removed.

After cleaning processes, the next step is to convert data (TrackerData) to hits (TrackerHits) [42] by the **InGridSimpleClusterFinder** processor. TrackerHits is the kind of the data that every track finder algorithm needs. For this conversion, three important parameters have to be set in the processor. The first and second parameters are the shutter and sample frequency which are given in table (6.1) for each run package dataset. The third one is the drift velocity. For all analyses for this thesis, it was calculated using MAGBOLTZ [83] simulation version 11.2 based on the information recorded during data taking. Table (6.2) shows an example of the compositions of gas mixture used for MAGBOLTZ simulation for runs 124 to 135. The precision of these numbers was important for using this software.

Run	Gas Compositions					
	Water %	Oxygen %	Ar %	CF ₄ %	iC ₄ H ₁₀ %	Pressure (Torr)
124	0.00778640	0.00582377	94.98707033	2.99959169	1.99972780	763.1715
125	0.02976488	0.00589050	94.96612739	2.99893034	1.99928689	763.2207
126	0.02867107	0.00589600	94.96716128	2.99896299	1.99930866	763.0422
128	0.03869666	0.00587009	94.95766158	2.99866300	1.99910866	763.1769
129	0.03828834	0.00589172	94.95802894	2.99867460	1.99911640	762.3706
131	0.03454722	0.00585327	94.96161953	2.99878799	1.99919199	762.5733
132	0.03274926	0.00588379	94.96329861	2.99884101	1.99922734	762.3178
133	0.03131944	0.00592550	94.96461731	2.99888265	1.99925510	763.0146
134	0.02819871	0.00593465	94.96757330	2.99897600	1.99931733	763.2474
135	0.02589533	0.00592957	94.96976635	2.99904525	1.99936350	763.3329

Table 6.2: The compositions of gas mixture used for MAGBOLTZ simulation including the contamination recorded during data taking for runs 124-135.

The percentage of the contaminations were calculated based on the amount of Oxygen and water recorded during each run and the ratio of each gas for the T2K gas mixture. The perfect condition is assumed to be the case that we would have 100 % T2K gas mixture. By reducing the total amount of the contaminations from one hundred and using the ratio of other gases, the percentage of other gases were calculated. Table (6.3) shows the drift velocity for the same run in table (6.2). Moreover, this simulation calculates the transverse (D_T) and longitudinal (D_L) diffusion constant.

Drift Velocity	
Run	v_d [mm/ μ s]
124	55.34 \pm 0.02
125	52.21 \pm 0.02
126	52.37 \pm 0.02
128	51 \pm 0.02
129	51.1 \pm 0.02
131	51.58 \pm 0.02
132	51.84 \pm 0.02
133	52 \pm 0.02
134	52.41 \pm 0.02
135	52.71 \pm 0.02

Table 6.3: Drift velocity for runs 124-135 from MAGBOLTZ simulation.

The **InGridBNDHoughTransformProcessor** was the main algorithm for track finding. This algorithm and also later the GBL algorithm for the fitting process need to access to the covariance matrix of the each hit which was missed during conversion. For this reason, a simple code was written to add the covariance matrix to each hit after converting data to hit. This processor is called **InGridDataHitGBLProcessor** which was mainly written for the GBL fitter. The covariance matrix for each hit is defined according to the diffusion as:

$$\mathbf{C} = \begin{bmatrix} \sigma_T^2 & 0 & 0 \\ 0 & \sigma_T^2 & 0 \\ 0 & 0 & \sigma_L^2 \end{bmatrix} \quad (6.1.1)$$

Figure (6.7) shows the final chain for the track reconstruction. The final output are tracks found and fitted by the algorithms. The first analysis was done to correct field distortion and the $\mathbf{E} \times \mathbf{B}$ effect.

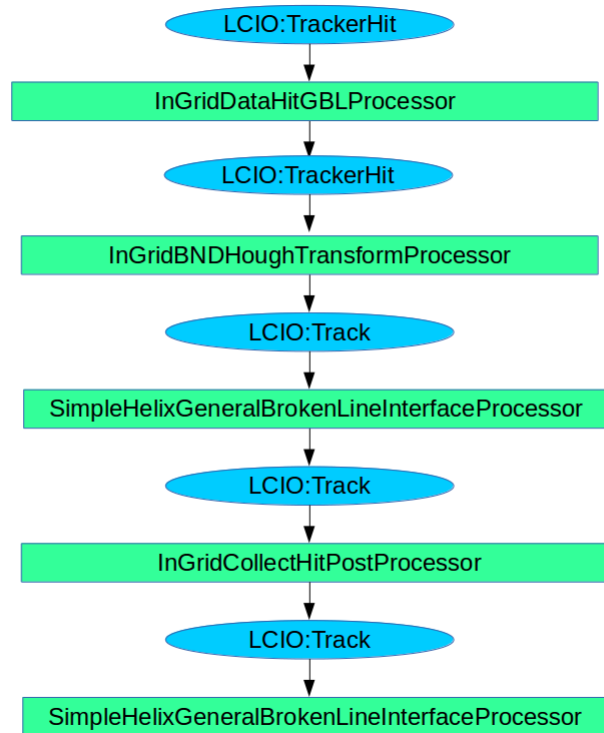


Figure 6.7: Chain of the track reconstruction for test beam data.

For correction of the hit position, first the **BiasedResidualsProcessor** [84] plots a 2D histogram of the residuals of hits in tracks. Figure (6.8) shows an example of xy-residual along the y-axis the effect of field distortion and the $\mathbf{E} \times \mathbf{B}$ for run 132. As it can be seen, there is S shape effect for each chip which causes the position of hits near the edge of the chip to shift.

For calculation of these shifts, the **MEANvsXCalculatorProcessor** was used two times; once for correcting the hit position in the X-Y plane and once for the Z direction. These corrections were done based on the distribution of the hits around their reconstructed track [84].

However, the correction of the hit's position in Z direction was not efficient due to the Time walk effect. The Output of the **MEANvsXCalculatorProcessor** is a text file named *MeansCorrectionXY* for the X and Y direction and *MeansCorrectionZ* including the correct position of each hit in the Z direction.

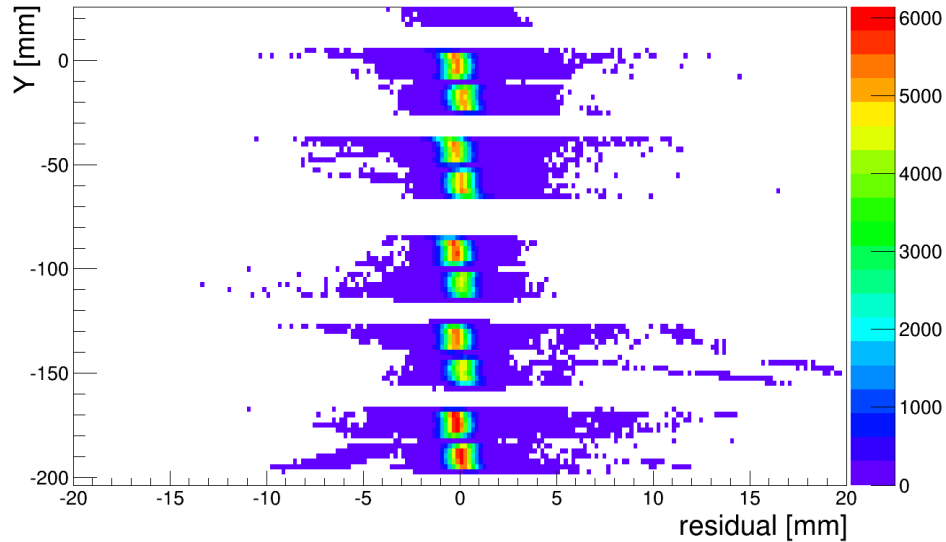


Figure 6.8: xy-residual along the y-axis with field distortion and $\mathbf{E} \times \mathbf{B}$ effect for run 132.

For correction, again it was needed to use the processor for converting data to hits. In addition to this processor, another processor called **MEANvsXCorrection-Processor** was implemented two times again. This processor reads the two text files and shifts the hit position to the correct position. After that the whole chain, shown in figure (6.7), as repeated based on the correct hit position and the output was used for other analysis. Figure (6.9) shows the xy-residual along the y-axis after correction for the same run.

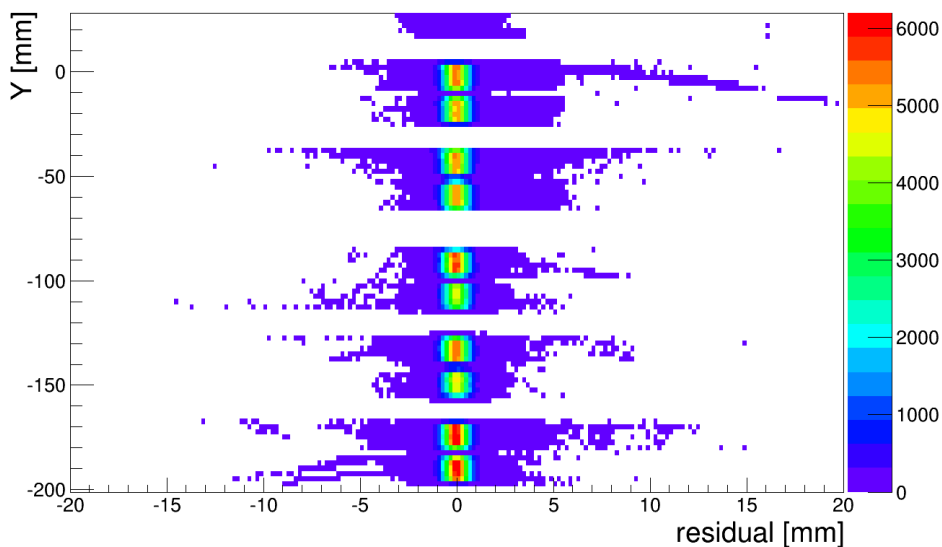


Figure 6.9: xy-residual along the y-axis after correction for run 132.

These correction also had a positive effect on the second run of the track reconstruction. Figure (6.10) shows how the χ^2/ndf for the merging process in the **InGridBNDHoughTransformProcessor** was changed after correction. These distributions belong to run 136. In addition, figure (6.11) shows the performance of the track reconstruction chain for before and after correction. Both of these figures show a significant improvement in result of the track reconstruction after correcting the hit position.

Furthermore, the data selection was done for each physics analysis. It means some events with the specific condition were selected for analysis. For each run, there were several events which either were empty or had more than one track. In order to have a better analysis, only events with one track and among of them only those that their track had at least more than 1200 hits were selected. In such a case, the length of the track was acceptable for the analysis.

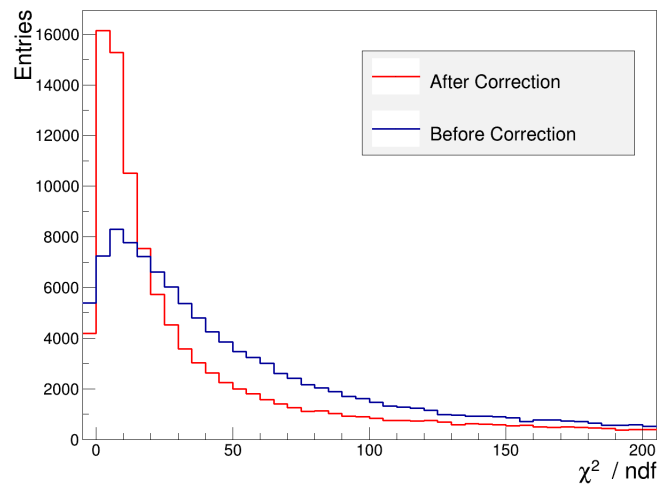
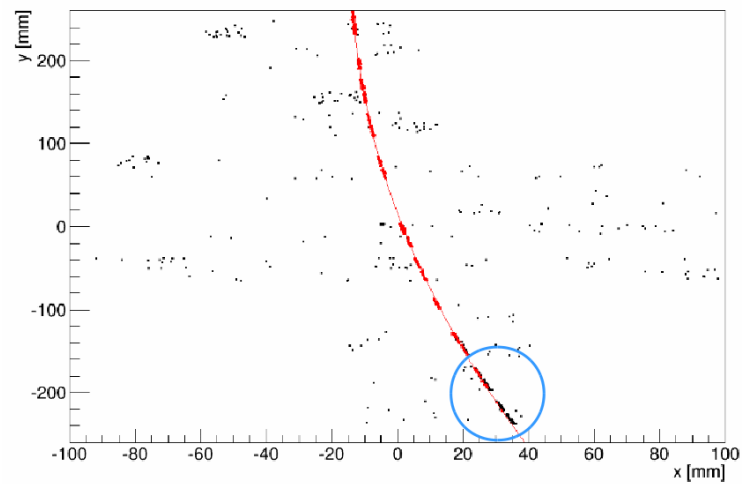


Figure 6.10: Distribution of χ^2/ndf for merging process in the **InGridBNDHoughTransformProcessor** before (blue line) and after correction (red line) for run 136.

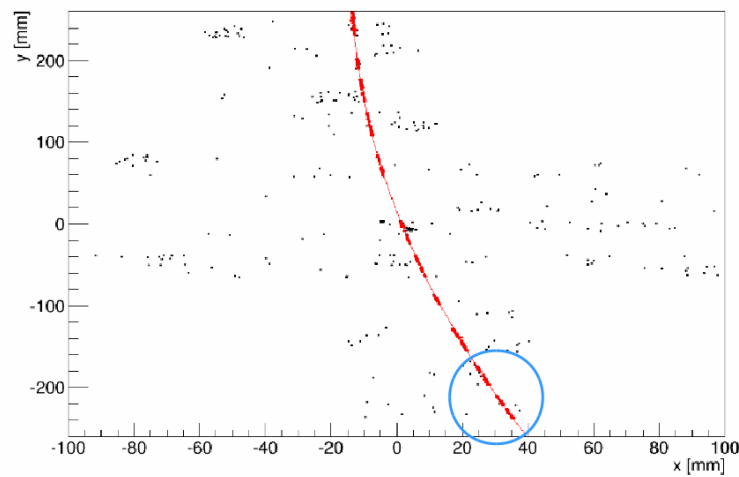
Figure (6.12-a) shows an example of the distribution of the number of hits on a track for before and after cutting for run 132. The main reason why the number of entries also was reduced after the cut (the green distribution) is the events with more than one tracks were also removed.

Another cutting utilized for analysis was D0 cut. After final reconstruction, there is a distribution of the D0 for all tracks for all events. First a Gaussian fitting was used around the maximum peak of the distribution. This fit returned a mean value (μ) and a standard deviation of the Gaussian fit (σ). Then the interval of $[\mu - \sigma, \dots, \mu + \sigma]$ as used for cutting. It means only events which their track had D0 between this interval were selected for analysis.

In this case, the tracks were selected which had nearly the same length and position in the TPC. Figure (6.12-b) shows the distribution of D0 before and after cutting for run 132.

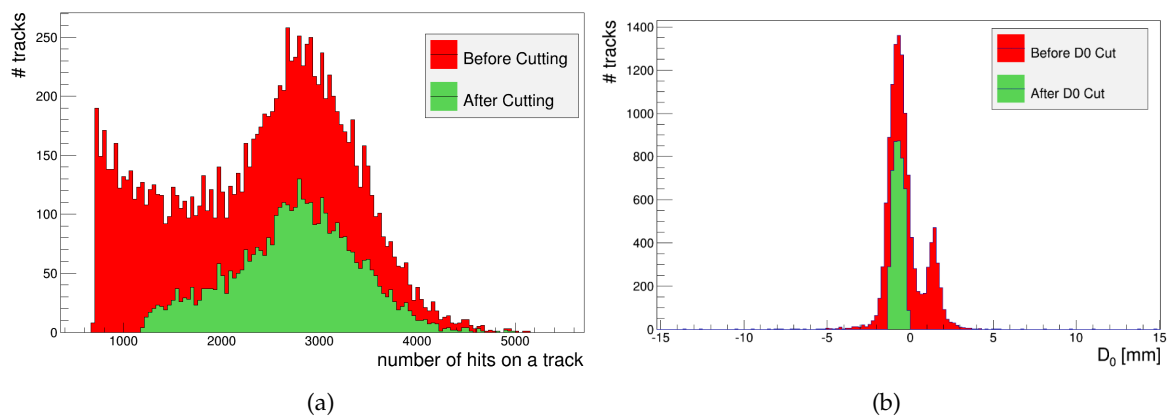


(a)



(b)

Figure 6.11: An example of a reconstructed track for before and after correction process. The black points are outliers and the red ones are inliers found by the algorithm. (a) Before correction, the two bottom Octoboards were missed (inside the blue cycle). (b) The same track after correction process and the second track reconstruction process.



(a)

(b)

Figure 6.12: (a) distribution of the number of hits on a track and (b) distribution of D_0 before and after cutting for run 132.

6.1.5 Data analysis

Momentum resolution

One of the studies done during the test beam experiment was P-scanning or momentum scanning. This package data had five runs. Each run had 10000 events with a nominal energy. The main goal of this study was to identify the momentum resolution. The theory of the momentum resolution calculation is explained in chapter 2. For all runs the magnetic field was 1.022 T which was measured by DESY group [85], drift field was 230 V/cm and the Z position at the stage of the LP TPC was -100 mm. Table (6.4) illustrates other parameters for each run used for this study.

P-scan		
Run	Nominal Energy [GeV]	Drift Velocity [mm/ μ s]
136	5	74.57 ± 0.01
137	4	74.68 ± 0.01
138	3	74.80 ± 0.01
139	2	74.88 ± 0.01
140	1	74.96 ± 0.01

Table 6.4: Parameters used for each run for momentum scanning.

As explained before, the drift velocity for each run was calculated by Magboltz simulation [83]. As regards for the momentum package dataset, the drift length for all runs was the same but the contamination of the gas mixture was not stable for all runs. Therefore the drift velocity was calculated by simulation for each run of this package dataset. On the other hand, according to [56] the difference between drift velocity from the measurement and simulation is small. Hence, it can be assumed that these drift velocities are nearly the same as in the real experiment. Figure (6.13) shows the spectrum of the transverse momentum versus the number of tracks for all runs.

It is clear from this figure that for the spectrum of the momentum there are non-Gaussian tails towards lower energy. The main reason is that the electron has to pass through the field cage wall and the magnet and consequently interacts with their material. One of the results of this interaction is pair production. For this reason for some events there is also a charged particle with a positive charge which passes through the sensitive area of the TPC and its momentum has effect on the momentum spectrum.

Another important point is the energy spread of the beam. One can use the nominal energy of the test beam if the energy spread is smaller than the detector resolution [86]. Table (6.5) shows the energy spread of the test beam area T24 at DESY. According to this table the energy spread is larger than the targeted momentum resolution.

Nominal Energy [GeV]	Energy Spread[%]
1	6.36
2	4.43
3	3.92
4	3.58
5	3.34

Table 6.5: Energy spread of the T24 test beam area at DESY [86].

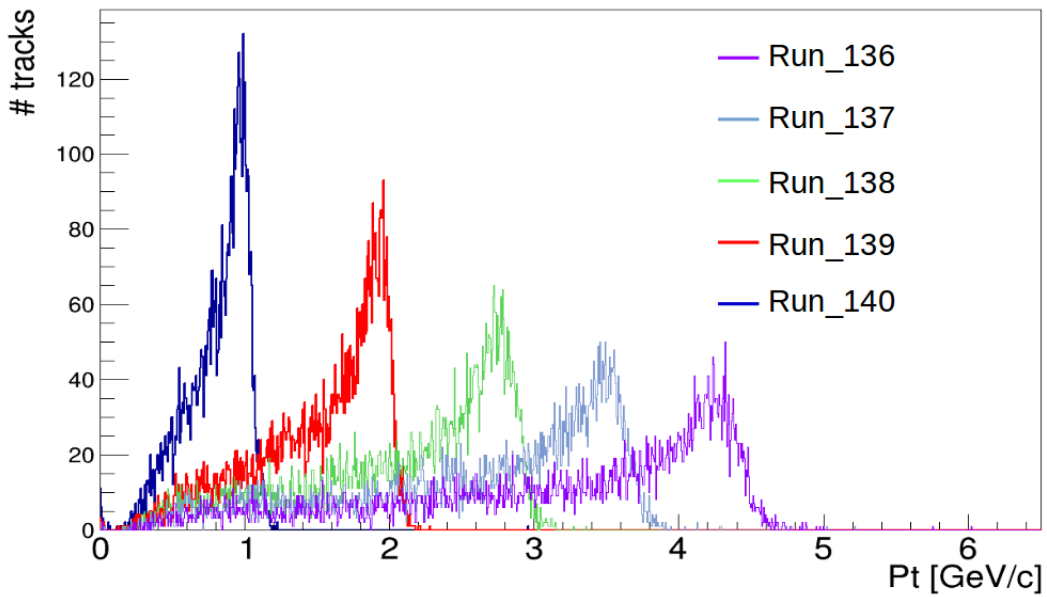


Figure 6.13: The spectrum of the momentum for all runs.

Finding the momentum and momentum resolution based on this distribution because of the long tail is difficult. The main reason is to select the correct cut for Gaussian fit on the plot. In order to solve this problem, a Crystal ball function is fitted to the distribution of inverse momentum $1/p_t$.

A Crystal ball function consists of a Gaussian core and a power-law tail which models the momentum resolution [86]

$$f(x, \alpha, n, \mu, \sigma) = N \cdot \begin{cases} \exp\left(-\frac{(x-\mu)^2}{2\sigma^2}\right) & \text{if } \frac{x-\mu}{\sigma} > -\alpha \\ A \cdot \left(B - \frac{(x-\mu)}{\sigma}\right)^n & , \text{ otherwise} \end{cases} \quad (6.1.2)$$

$$A = \left(\frac{n}{|\alpha|}\right)^n \cdot \exp\left(-\frac{|\alpha|^2}{2}\right)$$

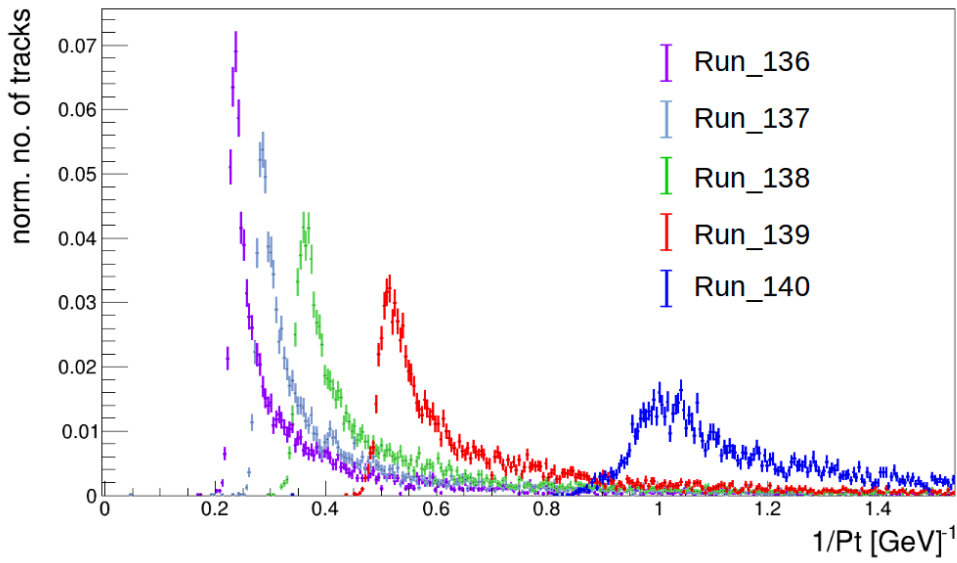
$$B = \frac{n}{|\alpha|} - |\alpha|$$

$$N = \frac{1}{\sigma(C + D)}$$

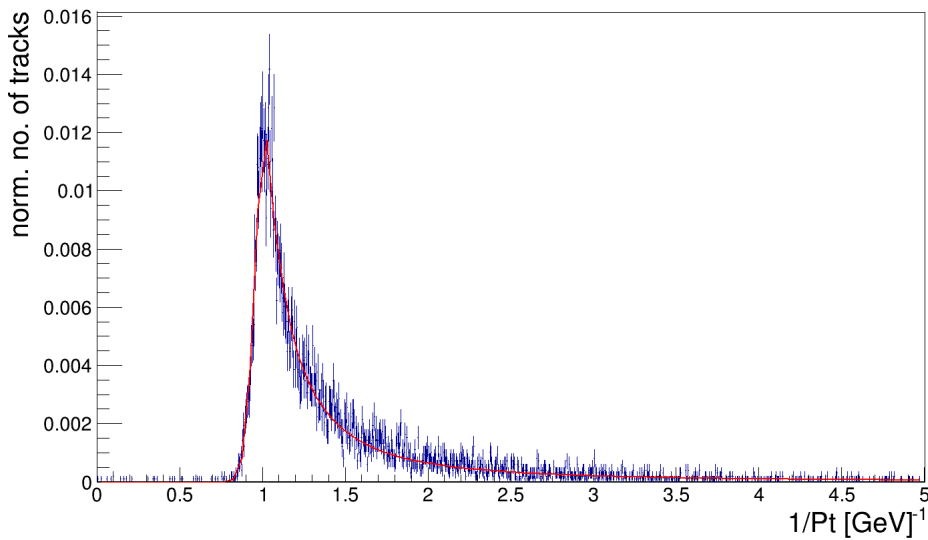
$$C = \frac{n}{|\alpha|} \cdot \frac{1}{n-1} \exp\left(-\frac{|\alpha|^2}{2}\right)$$

$$D = \sqrt{\frac{\pi}{2}} \left(1 + \operatorname{erf}\left(\frac{|\alpha|}{\sqrt{2}}\right)\right)$$

where μ and σ are the mean value and resolution respectively. N is a normalization factor, α is the transition point and n the power-law exponent. In addition, the erf is the error function [87]. Figure (6.14) shows the distribution of $1/p_t$ for all runs and an example of a Crystal ball function fit for Run 140.



(a)



(b)

Figure 6.14: (a) The spectrum of $1/p_t$ for all runs (b) the spectrum of inverse momentum for run 140 with a Crystal ball function fit.

First, the analysis of the momentum resolution was done for all tracks with different lengths and momenta which were found in the track reconstruction process (without any cut). Table (6.6) illustrates the results of the momentum and momentum resolution for all runs.

This analysis was repeated after applying a cut explained in the previous section. The table (6.7) illustrates the result of the momentum resolution after implementing the cut. The average of the reduced chi-square of the fit for all runs was about 1.01 which means the fits were acceptable.

As can be seen from the second column of the table (6.7), there is a deviation between what it was expected from experiment and what the measurement presented. One explanation for this issue is the magnetic field is not homogeneous in all areas [88].

Run	Momentum [GeV]	Momentum Resolution [GeV] ⁻¹	Number of Tracks
136	4.259 ± 0.009	0.009 ± 0.0004	12486
137	3.508 ± 0.007	0.011 ± 0.0004	11936
138	2.778 ± 0.0	0.014 ± 0.0006	11384
139	1.944 ± 0.004	0.019 ± 0.0008	10758
140	0.983 ± 0.002	0.061 ± 0.0016	9809

Table 6.6: Mometum and momentum resolution for all tracks found in the track reconstruction.

Run	Momentum [GeV]	Momentum Resolution [GeV] ⁻¹	Number of Tracks
136	4.275 ± 0.011	0.008 ± 0.0004	7087
137	3.524 ± 0.008	0.010 ± 0.0004	7237
138	2.785 ± 0.008	0.013 ± 0.0006	7433
139	1.951 ± 0.004	0.017 ± 0.0007	7119
140	0.986 ± 0.003	0.059 ± 0.0025	6108

Table 6.7: Mometum and momentum resolution for events after cutting.

Nevertheless, the main reason for this deviation is not fully clear and needs more investigation. This issue is also observed with other experiments done with other group. Figure (6.15) shows the deviation of the measurement (ΔP) for each run from the expectation value. According to this figure, except for 1 GeV, there is a linear trend with a slope between the amount of the deviation and the energy of the particle. However, in a homogeneous magnetic field, it is expected that this trend would be flat and parallel to the x-axis. For the rest of the analysis, the result of the measurement was used.

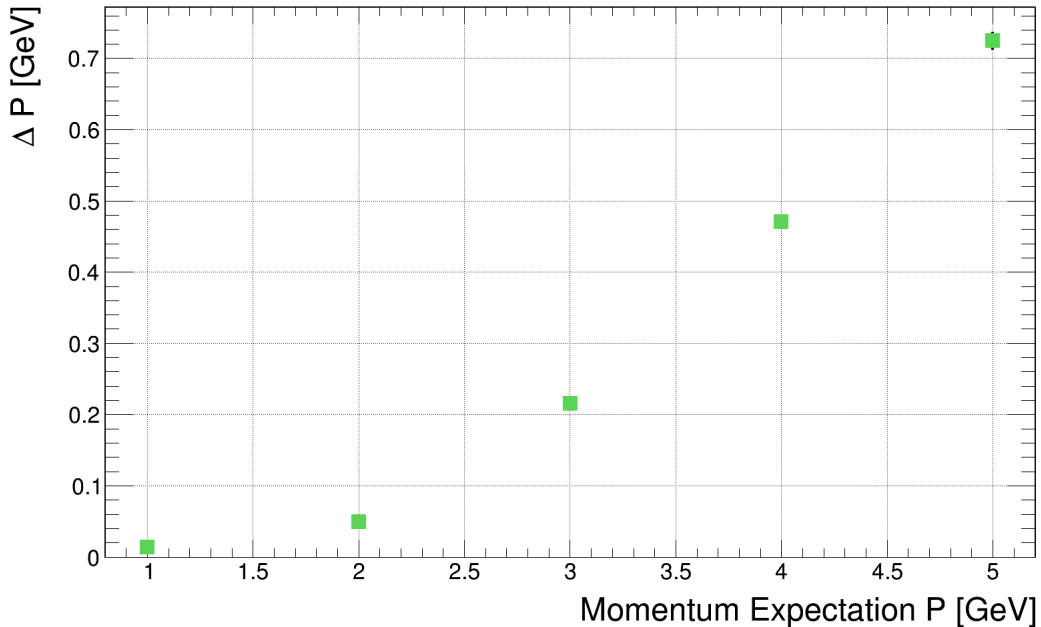


Figure 6.15: Difference between the expectation and measurement momentum.

These results of the momentum resolution can be compared with the results of the momentum resolution from Gluckstern equation based on the sagitta measurement and multiple scattering. In order to calculate the momentum resolution, equation (2.5.36) was implemented which has two terms. The first term is based on the sagitta measurement and as explained in chapter 2 it depends on the spatial resolution.

The transverse spatial resolution of each run was calculated by Magboltz simulation as the same as the drift velocity. Due to the fact that the intrinsic spatial resolution of a pixelated readout system is small ($15.9\mu\text{m}$), hence, it was assumed the spatial resolution is dominated by transverse diffusion. Moreover, in the first term, N is the number of hits and it was defined based on the mean value of the Gaussian fit on the distribution of the number of hits per track such as the plot shown in figure (6.12-a) for each run.

The second term of equation (2.5.36) is for multiple scattering. For this term, X_0 and L were assumed to be 110 m and 0.5 m, respectively. Furthermore, the magnetic field was 1.022 T and the momentum for this term was from the measurement (table 6.7). The following table shows the result of the momentum resolution.

Run	Term 1 (%)	Term 2 (%)	Momentum Resolution (%)	Measurement (%)
136	0.13	0.16	0.21	0.8
137	0.14	0.20	0.24	1.0
138	0.13	0.25	0.28	1.3
139	0.12	0.35	0.37	1.7
140	0.11	0.70	0.71	5.9

Table 6.8: Momentum resolution from Gluckstern equation (2.5.36) and measurement.

The first considerable point in the table (6.8) is the effect of the multiple scattering (Term 2) on momentum resolution for run 140 with 1 GeV and run 136 with 5 GeV. For the first case, the multiple scattering is the dominating part because of the lower energy of the particle. But for the second case, the effect of the two terms are almost close to each other.

Furthermore, comparing the third and fourth column of the table (6.8) shows there is a remarkable difference between the measurement and calculation. The main reason is the energy spread is so large (larger than the detector resolution). On the other hand, inhomogeneities in the magnetic field and the interaction of the incoming beam with the wall of the TPC and the magnet, as explained before make the measurement become worse. Therefore it is not possible to use the test beam data to measure the detector momentum resolution.

Transverse and longitudinal spatial resolution

Another interesting topic for analysis is to find the transverse and longitudinal spatial resolution for the tesbeam data. For this analysis, three package datasets were selected. All these three were done with a 1T magnetic field. The analysis of the case without a magnetic field was done before and the results are available in [56]. These three package datasets and the conditions of the experiment were mentioned in table (6.1) (identified by a star).

For all these three data packages, the intrinsic transverse spatial resolution is based on the pixel's size ($55\mu\text{m}/\sqrt{12} = 15.9\mu\text{m}$) which was mentioned in chapter 4. And the intrinsic longitudinal resolution is calculated according to equation (4.2.5) based on the sampling frequency and the drift velocity.

$$\sigma_{0z} = \nu_d \sigma_{0,t} = \frac{\nu_d}{f_c} \sqrt{\frac{1}{6}}$$

For analysis of the transverse spatial resolution, two methods were implemented. In the first method, for each drift length, there is a plot for the distribution of the X-Y residual of all N hits for tracks for all events. This distribution has a Gaussian shape. Then in the range of three RMS around the mean value of this distribution, a Gaussian function was fitted (figure (6.16 - a)). The sigma, identified by σ_N of this fit, was used as the width of the X-Y residual distribution. This method is identified by $3\sigma_N$ in all plots. A typical calculation of the single point resolution is [89] [90]

$$\sigma_{geo,xy} = \sqrt{\sigma_N \sigma_{N-1}} \quad (6.1.3)$$

where N is the number of hits for each track. However, in the case of InGrid, with 3000 hits as the average for each track, there is no significant difference between the result of σ_N and σ_{N-1} with one hit less. Thus, equation (6.1.3) becomes

$$\sigma_{geo,xy} \approx \sigma_N \quad (6.1.4)$$

The second method was based on the RMS distribution plot. In this method, the distribution of all RMS of the X-Y residual for each event was plotted and the mean value of this distribution is the width of the X-Y residual distribution (figure (6.16 - b)). This method always gives slightly better results than the first one.

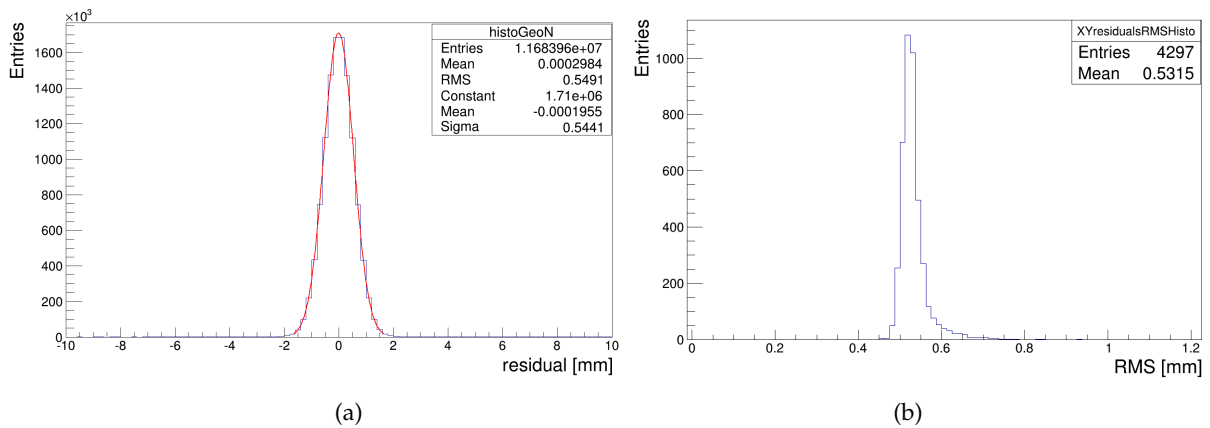


Figure 6.16: (a) The X-Y residual distribution for run 135 and (b) the RMS distribution for the same run.

For the longitudinal spacial resolution, only the $3\sigma_N$ was used. The important point for this case is because of the time walk effect for the Z residual distribution there is a tail and it is not symmetric. Therefore, the Gaussian fit was implemented only on the left side of this distribution. Again the sigma of the fit was considered as the width of the Z residual. Figure (6.17) shows an example of this distribution and fit for run 135.

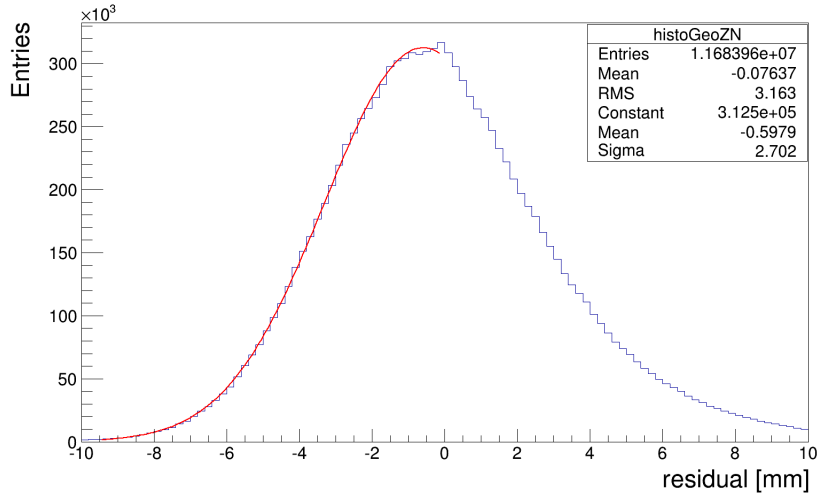


Figure 6.17: Z residual distribution for run 135.

Thereafter, these X-Y residual and Z residual were plotted against all drift lengths and after that equations (4.2.3) and (4.2.4) were used to fit the results of the RMS method in each plot in order to find the transverse and longitudinal diffusion constant, respectively. These two equation for the fitting are

$$\sigma_{xy} = \sqrt{\sigma_{0,xy}^2 + \sigma_T^2}$$

$$\sigma_z = \sqrt{\sigma_{0,z}^2 + \sigma_L^2}$$

The first analysis was done for runs 124 to 135. For some technical issues happened during the data taking for runs 127 and 130, these two runs were not completed. Hence, they were not used for analysis. For these data package, as mentioned in the table (6.1), the drift field was 130 V/cm, the magnetic field was 1T and the sampling frequency was 40 MHz.

Table (6.9) illustrates other parameters for these runs. The drift velocity mentioned in this table is the average of the drift velocity for all runs shown in the table (6.3). The transverse diffusion constant (D_T) and the longitudinal diffusion constant (D_L) were calculated by simulation as explained before. In addition, table (6.10) shows the Z position from reconstructed tracks for each run. The contaminations of the gas mixture for these runs was larger in comparison with the two other data packages. For this experiment, there was about 0.03% water as the average for all runs which was almost three times more than two other data packages with around 0.01%.

Run 124-135	
v_d [mm/ μ s]	52.26 ± 0.01
D_T [μ m/ \sqrt cm]	74.8 ± 2.3
D_L [μ m/ \sqrt cm]	332.6 ± 12.7
$\sigma_{0,xy}$ [μ m]	15.9
$\sigma_{0,z}$ [μ m]	533

Table 6.9: Parameters for runs 124 to 135. The drift velocity, the transverse and longitudinal diffusion constant are from simulation.

Run	Drift length[mm]
124	44 ± 4.25
125	66 ± 4.32
126	119 ± 4.44
128	171 ± 4.44
129	223 ± 4.66
131	274 ± 4.83
132	325 ± 4.94
133	374 ± 4.90
134	426 ± 4.90
135	482 ± 5.12

Table 6.10: The drift length of runs 124 to 135.

Figure (6.18) shows the result for both transverse and longitudinal resolution as a factor of the drift distance. In both plots, the simulation of a single electron diffusion was plotted according to equations (2.5.22), mentioned below, and it is the result for a perfect detector. Moreover, the transverse and longitudinal diffusion constant mentioned in the table (6.9).

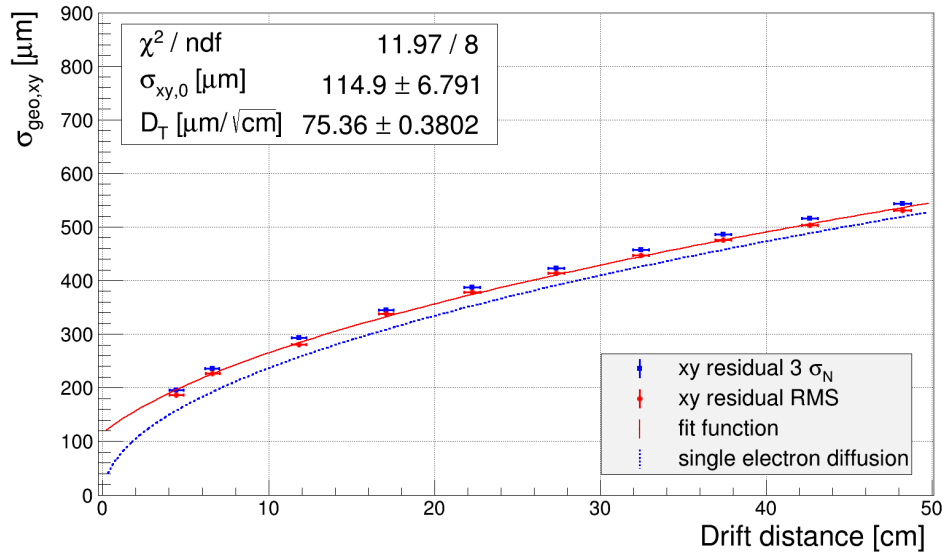
$$\sigma_T = D_T \sqrt{z_d} \quad \text{and} \quad \sigma_L = D_L \sqrt{z_d}$$

In chapter 8 of reference [56], it is mentioned that the correction of hit positions due to the field distortion has a significant improvement in the transverse spatial resolution. But for these runs, there is still a difference between the measurement and the simulation. It means the correction process was not able to correct distortion perfectly. This difference is larger for the lower drift lengths.

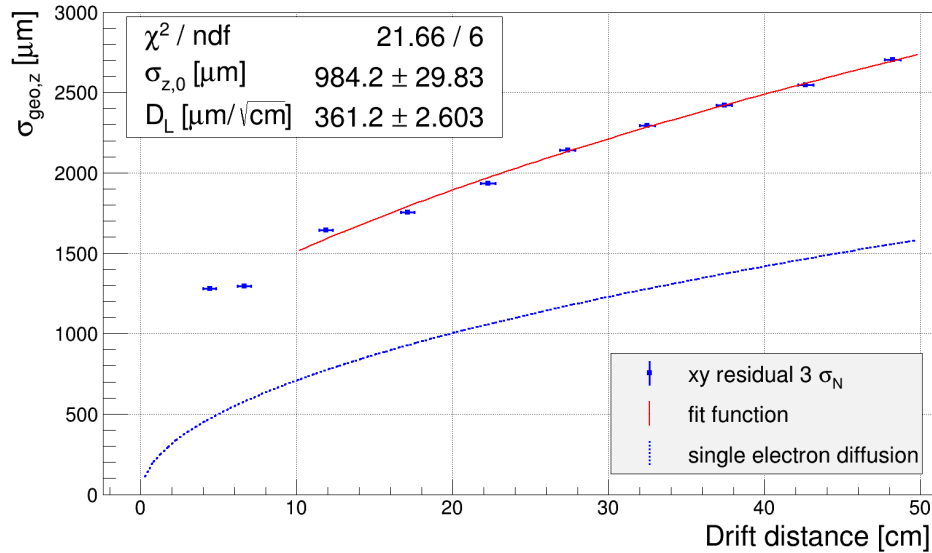
Comparing the result of the transverse diffusion constant from fit ($75.4 \pm 0.4 \mu\text{m}/\sqrt{\text{cm}}$ presented in figure (6.18)) with the simulation ($74.8 \pm 2.3 \mu\text{m}/\sqrt{\text{cm}}$) shows the measurement agrees with the simulation within uncertainties.

The intrinsic transverse spatial resolution ($\sigma_{0,xy}$) from the fit is $115 \pm 6.8 \mu\text{m}$ which is much larger than what the expected ($15.9 \mu\text{m}$). The main reason is even for the lower drift lengths (for instance for the run 124 with $44 \pm 4.25 \text{ mm}$ drift length), the resolution is dominated by the diffusion which is larger than the size of the pixel in the Timepix chip.

The plot for the longitudinal spatial resolution shows a remarkable difference between the simulation and the measurement. Although the correction of hit positions was used also for the Z direction, still the field distortion has a significant effect. In addition to the field distortion, the time walk effect also has a role for this difference. The result of the longitudinal diffusion constant of simulation was $332.6 \pm 12.7 \mu\text{m}/\sqrt{\text{cm}}$ and comparing this result with $361.2 \pm 2.6 \mu\text{m}/\sqrt{\text{cm}}$ from the fit on the measurement result shows a difference of about 2.2σ of the simulation. In contrast, the difference between the intrinsic longitudinal resolution from simulation ($533 \mu\text{m}$) and the fit ($984.2 \pm 29.8 \mu\text{m}$) is huge. In addition to the time walk effect, there could be other effect causing this difference.



(a)



(b)

Figure 6.18: (a) The transverse spatial resolution. The fit was done on the results of RMS. (b) the longitudinal spatial resolution for the runs 124 to 135. The first two points were not taken into account in the fit.

The second package dataset used for this analysis was for runs 76 to 88. Runs 79 and 80 were skipped due to the technical issue happened during the data taking. As mentioned in the table (6.1) the drift field was 230 V/cm and the sampling frequency was 40 MHz. Tables (6.11) and (6.12) illustrate the other parameters from simulation and drift length from the reconstructed tracks, respectively. The motivation of using these runs was to apply a different drift field from the previous data sets. According to the plot (2.9), the drift velocity and consequently the transverse diffusion constant change with rising the drift field.

Run 76-88	
v_d [mm/ μ s]	76.17 ± 0.01
D_T [μ m/ $\sqrt{\text{cm}}$]	93.5 ± 3.3
D_L [μ m/ $\sqrt{\text{cm}}$]	224.52 ± 4.02
$\sigma_{0,xy}$ [μ m]	15.9
$\sigma_{0,z}$ [μ m]	777.46

Table 6.11: Parameters for runs 76 to 88. The drift velocity, the transverse and longitudinal diffusion constant are from simulation.

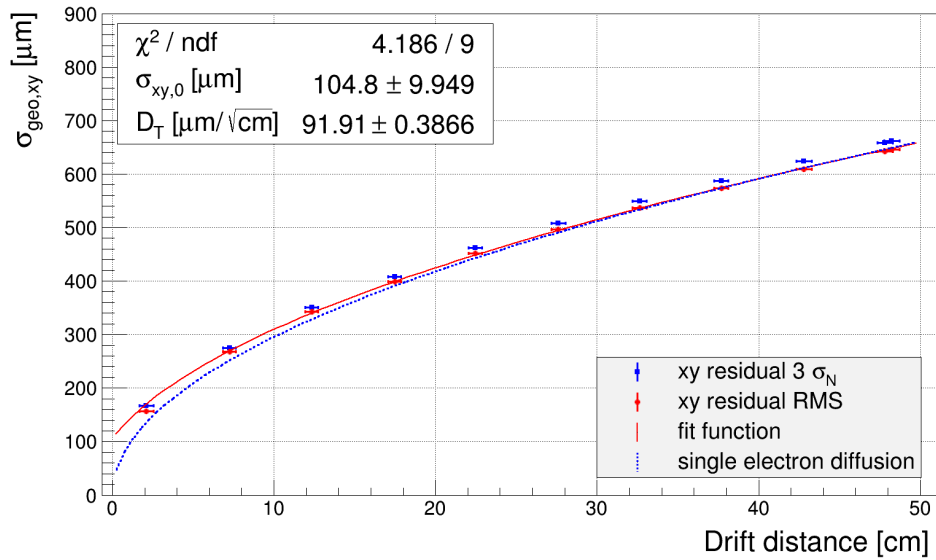
Run	Drift length[mm]
76	482 ± 4.75
77	478 ± 4.87
78	428 ± 4.71
81	377 ± 4.41
82	326 ± 4.4
83	276 ± 4.36
84	225 ± 4.2
85	175 ± 4.12
86	123 ± 4.08
87	72 ± 4
88	21 ± 4.21

Table 6.12: The drift length of runs 76 to 88.

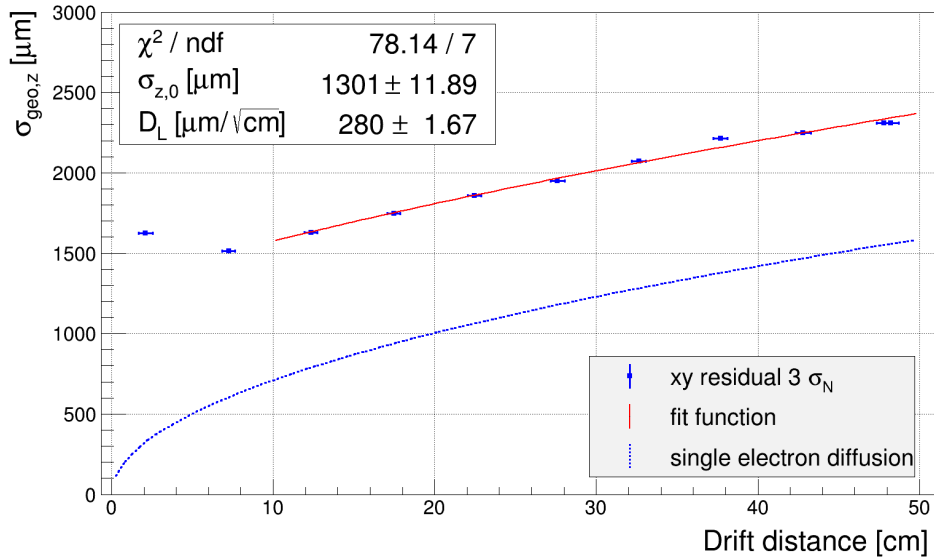
The figure (6.19-a) shows the transverse spatial resolution result. According to this plot the transverse diffusion constant obtained from the fit ($91.9 \pm 0.4 \mu\text{m}/\sqrt{\text{cm}}$) was very close to the result of simulation ($93.5 \pm 3.3 \mu\text{m}/\sqrt{\text{cm}}$). One of the significant issues that can be seen is the results for the longer drift lengths were very close to the simulation of the single electron diffusion. In contrast, for the lower drift lengths, e.g. for run 88 with 21 ± 4.21 mm, still there is a effect of distortion. Because of the lack of enough measurements near the anode plate, still the intrinsic transverse spatial resolution from the fit ($105 \pm 9.5 \mu\text{m}$) is so large.

For these runs, the longitudinal diffusion constant obtained from the fit with $280 \pm 1.67 \mu\text{m}/\sqrt{\text{cm}}$ was higher than the simulation result ($224.52 \pm 4.02 \mu\text{m}/\sqrt{\text{cm}}$). Moreover, figure (6.19-b) shows for the lower drift lengths the longitudinal spatial resolution increased. The reason for this rising could be because of the hodoscope effect or arriving some electrons before the shutter is open [56].

For this case also, the remarkable difference between the intrinsic longitudinal spatial resolution from the fit with $1301 \pm 11.89 \mu\text{m}$ and the simulation with $777.46 \mu\text{m}$ is visible. And certainly, not using the longitudinal spatial resolution of the lower drift lengths for the fit have an effect on this result.



(a)



(b)

Figure 6.19: (a) The transverse spatial resolution (b) the longitudinal spatial resolution for the runs 76 to 88. For the first plot, the fit was done on the results of RMS. For the second plot the first two points were not taken into account.

The last analysis was done for runs 178 to 190. For this package datasets, the sampling frequency was 80 MHz. Tables (6.13) and (6.14) show the parameters and the drift length of all runs. From the figure (6.20-a) for the transverse diffusion constant there is a agreement between the simulation ($92.2 \pm 3.04 \mu\text{m}/\sqrt{\text{cm}}$) and the measurement obtained from the fit ($92.4 \pm 0.3 \mu\text{m}/\sqrt{\text{cm}}$). For this case, the intrinsic transverse spatial resolution with $82.6 \pm 7.66 \mu\text{m}$ was better than the two previous results.

Run 178-190	
v_d [mm/ μ s]	75.6 ± 0.01
D_T [μ m/ $\sqrt{\text{cm}}$]	92.2 ± 3.04
D_L [μ m/ $\sqrt{\text{cm}}$]	225.9 ± 9.25
$\sigma_{0,xy}$ [μ m]	15.9
$\sigma_{0,z}$ [μ m]	385.78

Table 6.13: Parameters for runs 178 to 190. The drift velocity, the transverse and longitudinal diffusion constant are from simulation.

Run	Drift length[mm]
178	484 ± 4.8
179	480 ± 4.96
180	430 ± 4.84
181	379 ± 4.71
182	328 ± 4.73
183	277 ± 4.61
184	226 ± 4.63
185	174 ± 4.6
186	123 ± 4.46
187	72 ± 4.4
188	22.5 ± 3
189	18.5 ± 2.12
190	45.5 ± 4.37

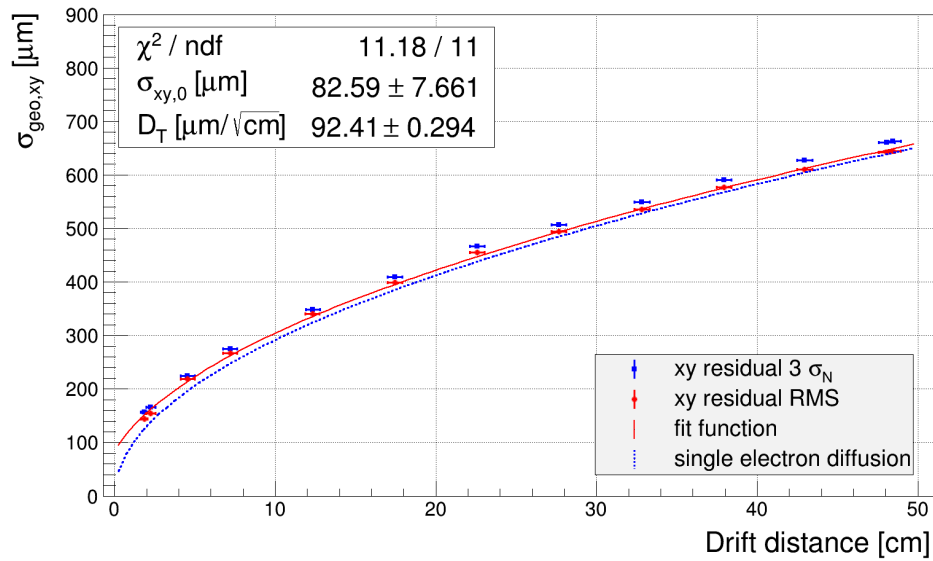
Table 6.14: The drift length of runs 178 to 190.

For the longitudinal spatial resolution, again one can see a significant difference between the longitudinal diffusion constant from the simulation with $226 \pm 9.25 \mu\text{m}/\sqrt{\text{cm}}$ and the result of the fit with $279 \pm 1.47 \mu\text{m}/\sqrt{\text{cm}}$. Theoretically, for this case, one can expect a better intrinsic longitudinal spatial resolution because of the faster sampling frequency.

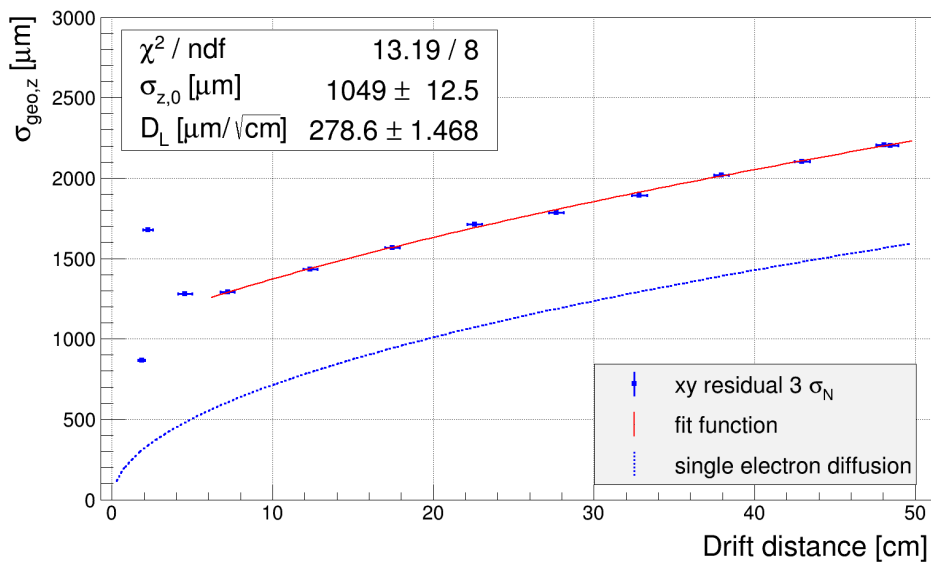
As a final conclusion of this section, the comparison between the first and second package datasets shows an increase in the transverse diffusion for higher drift fields in both simulation and experiment results. This increase is expected according to the plot (2.9). It can be seen from this plot that for a 1 T magnetic field (green line), for drift fields higher than 100 V/cm, both the transverse diffusion and drift velocity increase with rising the drift field.

Furthermore, it was illustrated in chapter 2 that a magnetic field does not have any effect on the longitudinal diffusion constant. This is what one can see from the second and third package datasets. The main reason that the first package dataset has a different longitudinal diffusion (larger than two others) is due to contaminations of the gas. It was mentioned earlier that for the runs for this package dataset, the contaminations were larger than two others.

It was mentioned that the idea to use the third data package was it had a different sampling frequency (80 MHz) and therefore the intrinsic longitudinal spatial resolution would be better than two others. Although the result ($1049 \pm 12.5 \mu\text{m}$) is better than the second package dataset ($1301 \pm 11.9 \mu\text{m}$), it is in the range of about 2.2σ of the first one ($984.2 \pm 29.83 \mu\text{m}$). The main reason is they had different drift velocity. It has to be mentioned for all these three package datasets, the first two or three measurements close to anode were ignored from fitting. For the lower drift



(a)



(b)

Figure 6.20: (a) The transverse spatial resolution (b) the longitudinal spatial resolution for the runs 178 to 190. For the first plot, the fit was done on the results of RMS. For the second plot the first three points were not taken into account.

length, probably due to the stronger effect of the hits with large time walk effect on the reconstructed z position of the tracks, the residual distribution is wider [56].

Moreover, as mentioned before, for all three package datasets, the result of the intrinsic transverse spatial resolution from the fit is higher than what is expected. The main reason is the lack of measurements very close to the anode. The closest drift distance of these three experiments is for run 189 with 18.5 ± 2.12 mm drift distance from the end-plate, belonging to the third package datasets. It can be seen that for this experiment, the intrinsic transverse spatial resolution is better than two others with $82.6 \pm 7.66 \mu\text{m}$.

Chapter 7

Summary

As a summary, it was discussed that current theories, mainly the Standard Model, are mostly able to explain what we observe in our universe and still there are many open questions. To explore new answers or explanations for many unknown phenomena more investigation is needed on the new technologies used for this purpose. It is obvious that with more precise tools, measurements will be more accurate which results in better analysis.

The International Linear Collider (ILC) is one of the best candidates for the future of the particle physics. This collider enables us to explore more on many subjects such as Higgs physics, top physics and also somehow expand and access towards physics beyond the Standard Model. It was also mentioned that because the ILC is an electron-positron collider, it has fewer backgrounds causing to have a clean environment for each event and therefore more accurate results of the analysis.

The ILC has two detectors which the International Large Detector (ILD) is one of them. It consists of different layers of sub-detectors. One of the substantial sub-detectors is a tracker detector. Higher precision to measure the momentum and energy losses of particles is a vital mission of this layer. This leads to better essential studies of many phenomena such as Higgs-strahlung. The Time Projection Chamber (TPC) as a gaseous tracker detector is foreseen for the ILD. This detector has many advantages of which the most important is to have many continuous hits along the trajectory of particles. This characteristic is significant for pattern recognition (track finding).

To improve this factor in the TPC, a pixelized readout system was assumed for that. In this case, the number of hits would remarkably increase. The InGrid chip which is a combination of a Micromegas technology and Timepix chip, is the main candidate for this purpose. This readout system is under investigation and some preliminary experiments show that it is a promising technique for the linear collider in the future. The result of this combination is to have many hits (much more than pad readout, i.e. the current readout system used in a TPC) along a track.

Despite the fact that generally having many hits would be useful for pattern recognition, for the experiments done in 2015 at LP TPC at DESY, in addition to noise in the system and diffusion causes more difficulties to do track finding. This experiment was done with 160 InGrid chips leading to having about 3000 hits per track. To develop an algorithm which can do track finding for this amount of hits was the main topic of this thesis. For this purpose a local method has been developed which means instead of using all hits as inputs to an algorithm simultaneously, in the first step, it was tried to find a segmentation of a track in small regions called tracklet and separate it from other tracklets in the same regions and then after finding all tracklets for all tracks, connect all relevant tracklets to each other to have the full tracks.

To find tracklets, Octoboards are used as a unit of segmentation of tracks. First, for each Octoboard, Hough transform implemented as the main algorithm for track finding. Hough transform is robust against the outliers (here noise) but in a TPC, it suffers from diffusion. For solving this issue, a bivariate normal distribution (BND) was utilized to improve the voting process and collect inliers (hits) directly in a Hough space. For initializing the BND, the width of tracks based on the diffusion and the Z position of hits were calculated in the Hough space. The advantage of this method is not only still one can have the robustness ability of the Hough transform, but also take the diffusion into account. This process was done in both the X-Y and the S-Z plane.

After fitting in order to collect inliers, the semi-major and semi-minor axes of the ellipse correspond to one σ of the fit was calculated and considered all hits that their lines in the Hough space pass through this ellipse are inliers. The fit range and the size of the ellipse are changeable in both planes which means the number of inliers can change according to these parameters. This method results to have three-dimensional inliers collection (or track finding).

The optimization was done for four parameters of this algorithm to avoid any tuning manually. These four parameters identify the fit range of the BND and the size of the ellipse used for collecting inliers in both planes.

After finding inliers the Karimäki and linear regression were used to find five parameters of tracklets. Thereafter the merging process was done for collecting all relevant tracklets based on the extrapolation of two tracklets parameters from two sequence Octoboards to the mid point between them and then calculating χ^2/ndf of their parameters in that point. In the end, the General Broken Lines (GBL) was utilized as the track fitting algorithm for calculating five parameters of tracks. In addition, a post-processing algorithm was developed for recollecting inliers in case of missing Octoboards in the merging process.

Following a successful performance of this algorithm for different simulations, it was utilized to analyze experimental data, mentioned before, particularly for runs done with a magnetic field. There were two main purposes to chose these runs. First of all to test the algorithm's performance for real data which their quality is much more worse than the simulation data. And the second purpose was with a magnetic field the trajectory of a particle is not straight anymore and it was the main goal of this thesis to develop an algorithm can do track finding for any track with different curvature.

Two physics concepts were considered for analysis: one the momentum resolution and one the transverse and longitudinal spatial resolution. The results of these two analyses are presented in chapter 6 but what was very important from these analyses is that the checking and controlling the performance of the algorithm showed that it was also successful for the real data even for events with more than one particle and also different charge. This controlling was done by eye (explained in chapter 3).

However, the main disadvantage of this method is that it is slow and there are two main reasons. One case is the quality of experimental data. Much noise and time walk effects are two main sources of the poor quality of the real data. Somehow they could be reduced by improving the performance of the hardware. On the other hand, a more accurate pre-processing to clean data is needed.

The second reason is that the Hough transform by itself is a slow algorithm. In addition to this issue, using the ROOT and filling histogram cause it to become slower. For optimization of the speed of the algorithm one solution is to avoid using the histogram in ROOT.

Using two-dimensional vector in C++ would be a better choice instead of the histogram in ROOT. Also for fitting the BND, ROOT was implemented to having a graphical output for visualization which can be avoided.

As a conclusion, in spite of the timing issue, this method has shown a successful performance for both simulation and experimental data which is a sign that it is promising even for the future experiments. It was able to separate tracks from each other even for the case that there were one or more intersection points of tracks in an event. Another advantage of this algorithm is that it works for any cases. Most algorithms developed before based on the Hough transform work for the case that tracks are parallel to the X-Y plane. Meanwhile, for this algorithm developed for this thesis, it is not the case and it can work for all tracks with different parameters.

For the future pixelized readout system, there are still many possible algorithms to use for the track finding. But based on the experiences for this thesis it is recommended to use ensemble methods, i.e. using two or more algorithms together like what has been done for this thesis, to have a better performance and some of these algorithms need a modification for this readout system with many hits along a track.

Appendix A

Covariance matrix for Karimäki fit

In chapter 4 in section 4.5.1, it was mentioned how Karimäki used a non-iterative method to solve the problem for a least squares circle fit [69]. In addition, his approach to calculate Ω , d_0 and ϕ_0 was explained. Moreover, it was illustrated that the covariance matrix of circle fitting (\mathbf{V}) is given by the inverse of a matrix computed at minimum χ^2 .

$$(\mathbf{V}^{-1})_{jk} = \sum_i \omega_i \frac{\partial \varepsilon_i}{\partial P_j} \frac{\partial \varepsilon_i}{\partial P_k}$$

where Ω , ϕ_0 and d_0 are denoted as P_1 , P_2 and P_3 , respectively. In this appendix the calculation of \mathbf{V}^{-1} is explained as follow [69]:

$$\begin{aligned} (\mathbf{V}^{-1})_{\rho\rho} &= \frac{1}{4}S_{r^4} - d(S_\delta - d[S_{\alpha\alpha} + \frac{1}{2}S_{r^2} - d(S_\alpha - \frac{1}{4}dS_\omega)]) \\ (\mathbf{V}^{-1})_{\rho\phi} &= -u[\frac{1}{2}(\cos(\phi)S_{xr^2} + \sin(\phi)S_{yr^2}) - d(S_\gamma - \frac{1}{2}dS_\beta)] \\ (\mathbf{V}^{-1})_{\phi\phi} &= u^2(\cos^2(\phi)S_{xx} + \sin(2\phi)S_{xy} + \sin^2(\phi)S_{yy}) \\ (\mathbf{V}^{-1})_{\rho d} &= \rho(-\frac{1}{2}S_\delta + dS_{\alpha\alpha}) + \frac{1}{2}uS_{r^2} - \frac{1}{2}d[(2u + \rho d)S_\alpha - udS_\omega] \\ (\mathbf{V}^{-1})_{\phi d} &= u(\rho S_\gamma - uS_\beta) \\ (\mathbf{V}^{-1})_{dd} &= \rho(\rho S_{\alpha\alpha} - 2uS_\alpha) + u^2S_\omega \end{aligned}$$

where

$$\begin{aligned} u &= 1 + \rho d \\ S_x &= \sum \omega_i x_i \\ S_y &= \sum \omega_i y_i \\ S_\alpha &= \sin(\phi)S_x - \cos(\phi)S_y \\ S_\beta &= \cos(\phi)S_x + \sin(\phi)S_y \\ S_\gamma &= (\sin^2(\phi) - \cos^2(\phi))S_{xy} + \sin(\phi)\cos(\phi)(S_{xx} - S_{yy}) \\ S_\delta &= \sin(\phi)S_{xr^2} - \cos(\phi)S_{yr^2} \\ S_{\alpha\alpha} &= \sin^2(\phi)S_{xx} - 2\sin(\phi)\cos(\phi)S_{xy} + \cos^2(\phi)S_{yy} \end{aligned}$$

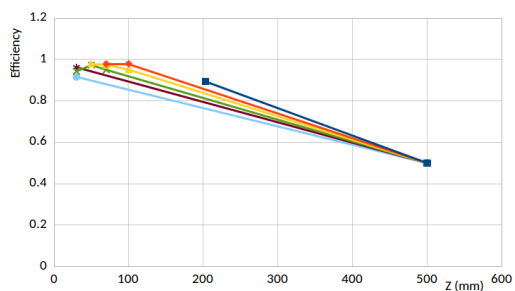
However, it has to be mentioned that the calculation of the inversion of the covariance matrix is complicated and makes the computing time to become slow.

Appendix B

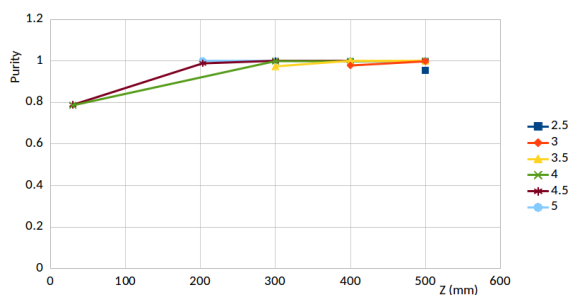
The plots for the optimization

In chapter 5 the optimization processes for the scale of the fit range and the scale of the ellipse axes were explained. It was mentioned that it was done for different scale factors for the fit ranges and different scale factors of the axes for both the X-Y plane and S-Z plane. Tables (5.5) and (5.7) illustrate the scale factor of fit range for different regions of the LP TPC used in the code, and figures (5.7), (5.8), (5.17) and (5.18) show the efficiency and the purity of scale factor one for the fit range for the X-Y and S-Z plane, respectively.

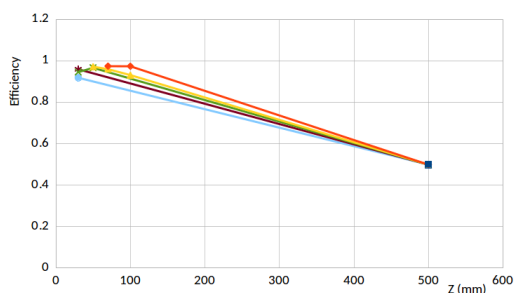
In this appendix, the other plots of the efficiency and the purity of the scale factor of the fit range mentioned in tables (5.5) and (5.7) are presented. For simplicity, the scale factors of the ellipse axes up to 5 are shown in all plots.



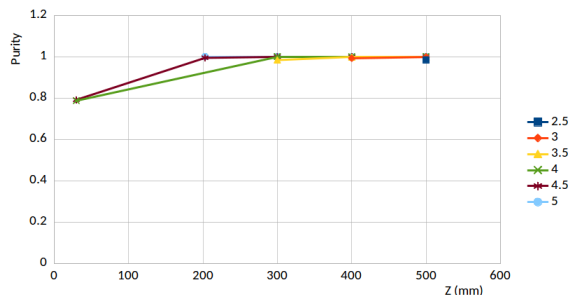
(a) scale factor of the fit range 2



(b) scale factor of the fit range 2

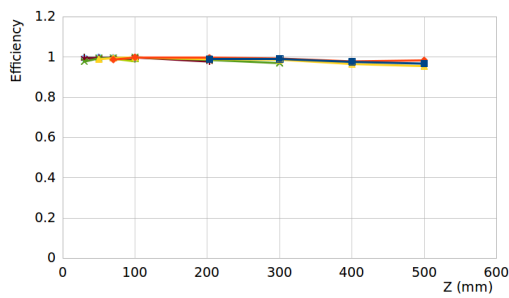


(c) scale factor of the fit range 2.5

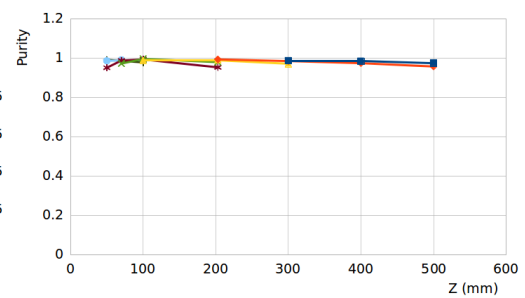


(d) scale factor of the fit range 2.5

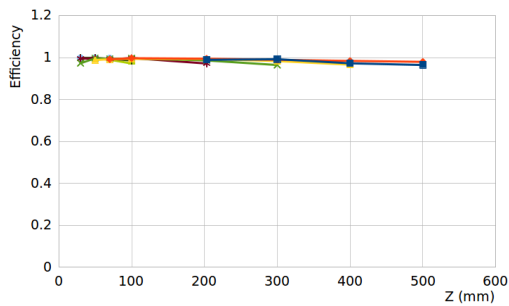
Figure B.1: (a) Track efficiency and (b) track purity for the case that the scale factor of the fit range was 2 and 2.5. These plots are for the all scale factor of the ellipse axes versus all drift lengths. The distance of two tracks was 2 mm distance in the Y direction.



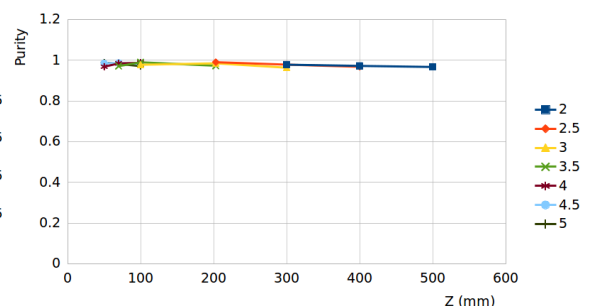
(a) scale factor of the fit range 2



(b) scale factor of the fit range 2

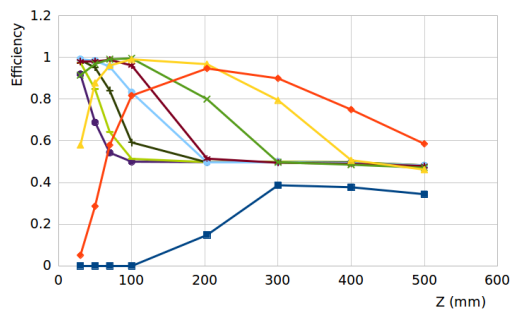


(c) scale factor of the fit range 2.5

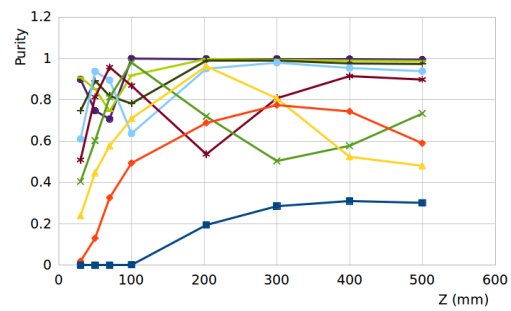


(d) scale factor of the fit range 2.5

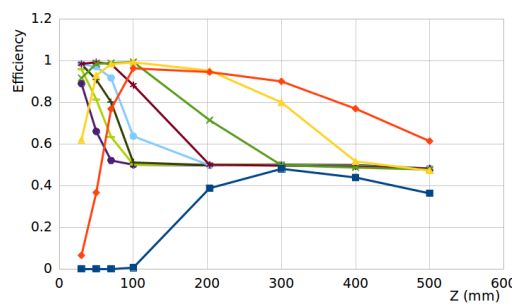
Figure B.2: (a) Track efficiency and (b) track purity for the case that the scale factor of the fit range was 2 and 2.5. These plots are for the all scale factor of the ellipse axes versus all drift lengths. The distance of two tracks was 5 mm distance in the Y direction.



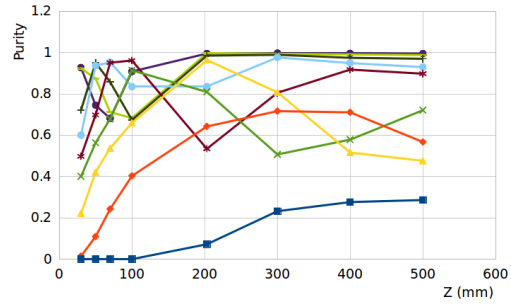
(a) scale factor of the fit range 1.5



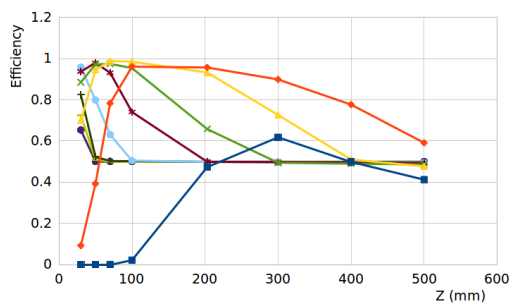
(b) scale factor of the fit range 1.5



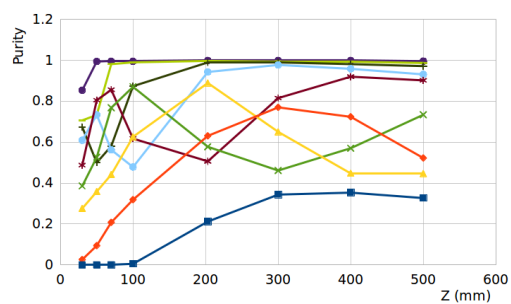
(c) scale factor of the fit range 2



(d) scale factor of the fit range 2

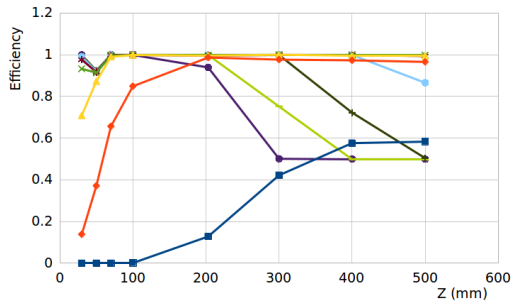


(e) scale factor of the fit range 3.5

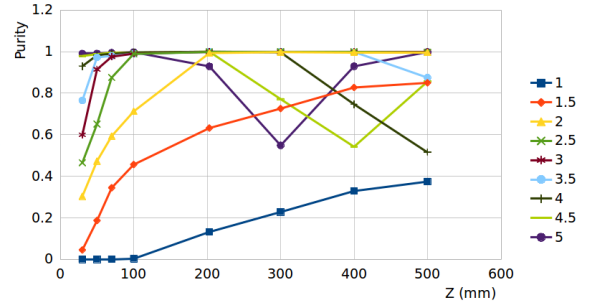


(f) scale factor of the fit range 3.5

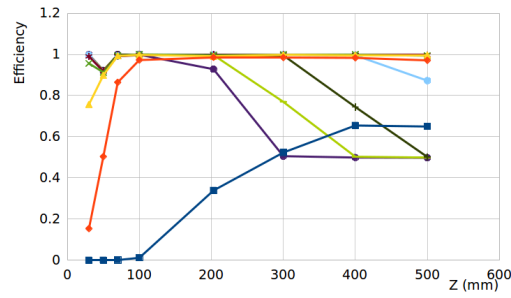
Figure B.3: (a) Track efficiency and (b) track purity for the case that the scale factor of the fit range was 1.5, 2 and 3.5. These plots are for the all scale factor of the ellipse axes versus all drift lengths. The distance of two tracks was 5 mm distance in the Z direction.



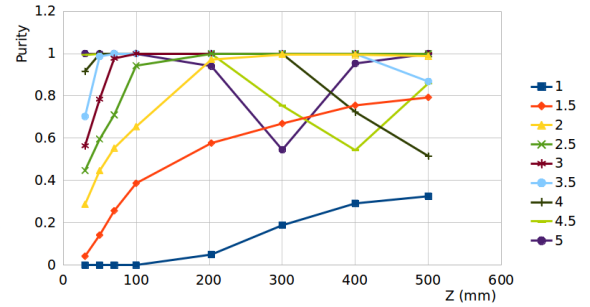
(a) scale factor of the fit ranger 1.5



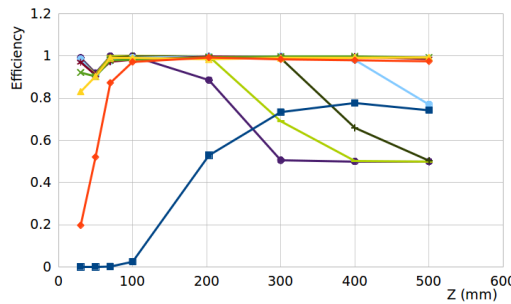
(b) scale factor of the fit range 1.5



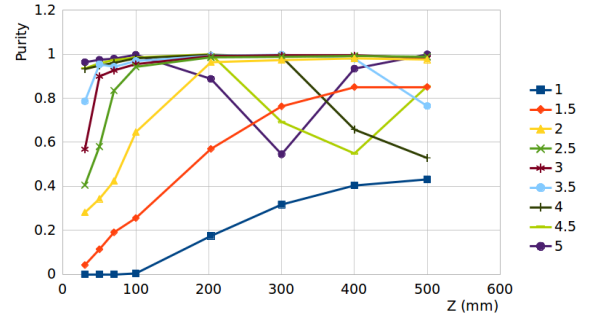
(c) scale factor of the fit range 2



(d) scale factor of the fit range 2



(e) scale factor of the fit range 3.5



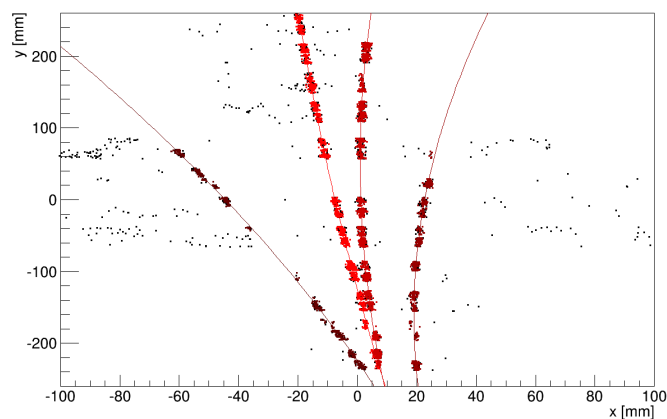
(f) scale factor of the fit range 3.5

Figure B.4: (a) Track efficiency and (b) track purity for the case that the scale factor of the fit range was 1.5, 2 and 3.5. These plots are for the all scale factor of the ellipse axes versus all drift lengths. The distance of two tracks was 10 mm distance in the Z direction.

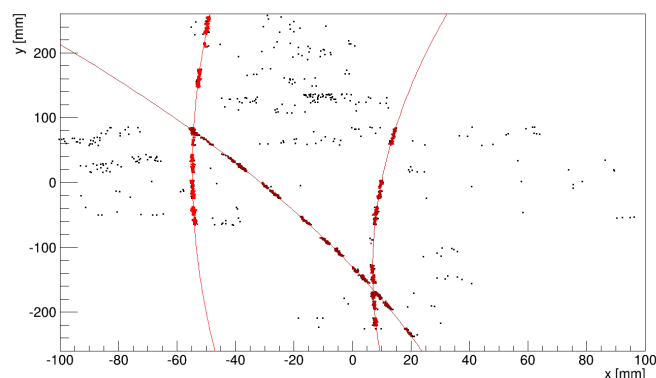
Appendix C

Examples of the track reconstruction

In this appendix, some example of the result of the track reconstruction for some of the runs used for analysis will be shown. All of them show the tracks in the X-Y plane. In all of them, the black points are outliers and colored points are inliers found by the `InGridBNDHoughTransformProcessor`. As mentioned in chapter 4 after the finding process, the General Broken Lines is used for the final fitting process. For some of these events, there are no found tracks. The reason is the number of their hits was less than a threshold chosen in the `InGridBNDHoughTransformProcessor`.



(a)



(b)

Figure C.1: (a) an event for run 76 with four particles and (b) an event for run 87 with three particles

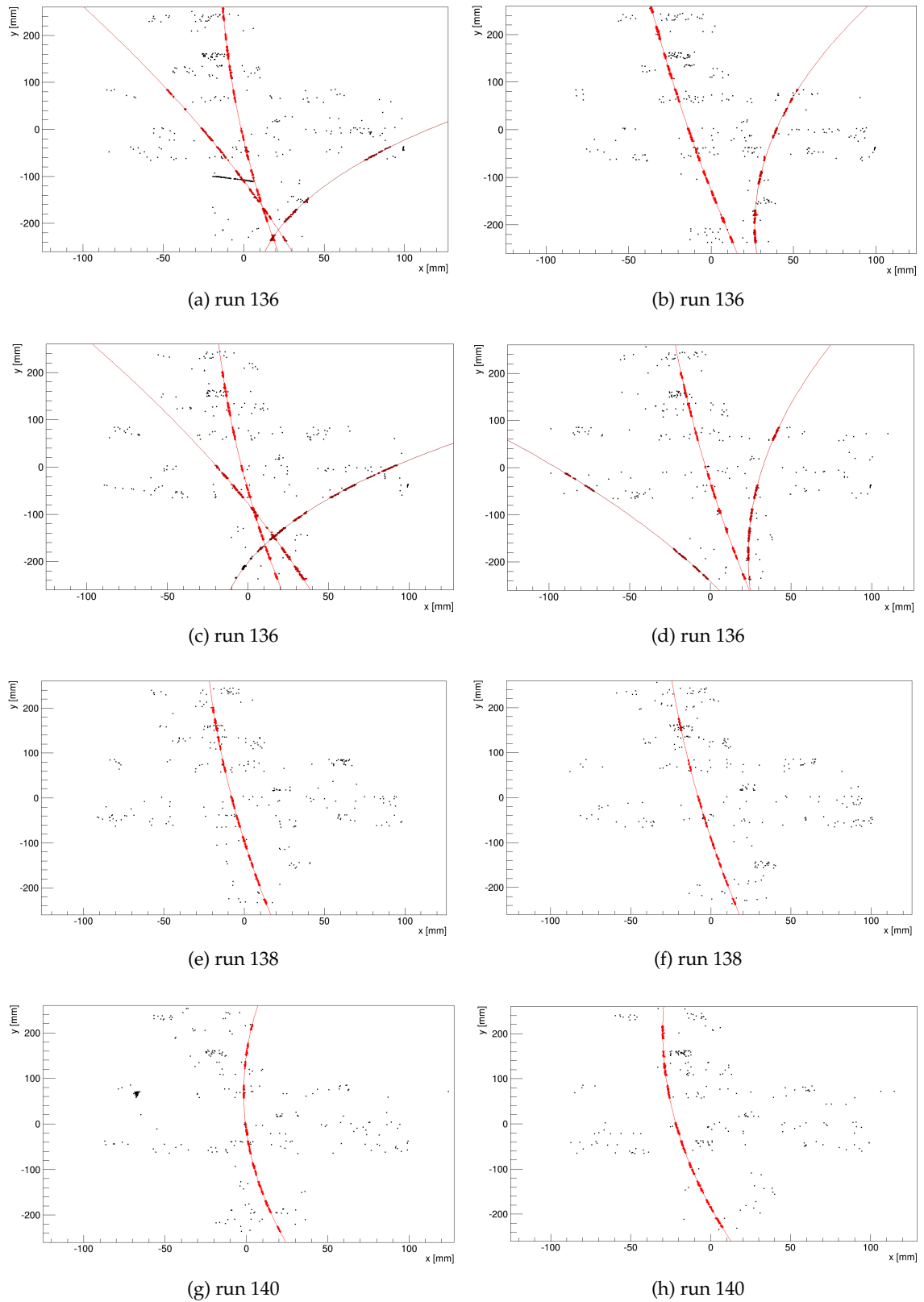


Figure C.2: Momentum resolution: runs 136 with 5 GeV, 138 with 3 GeV and 140 with 1 GeV nominal energy.

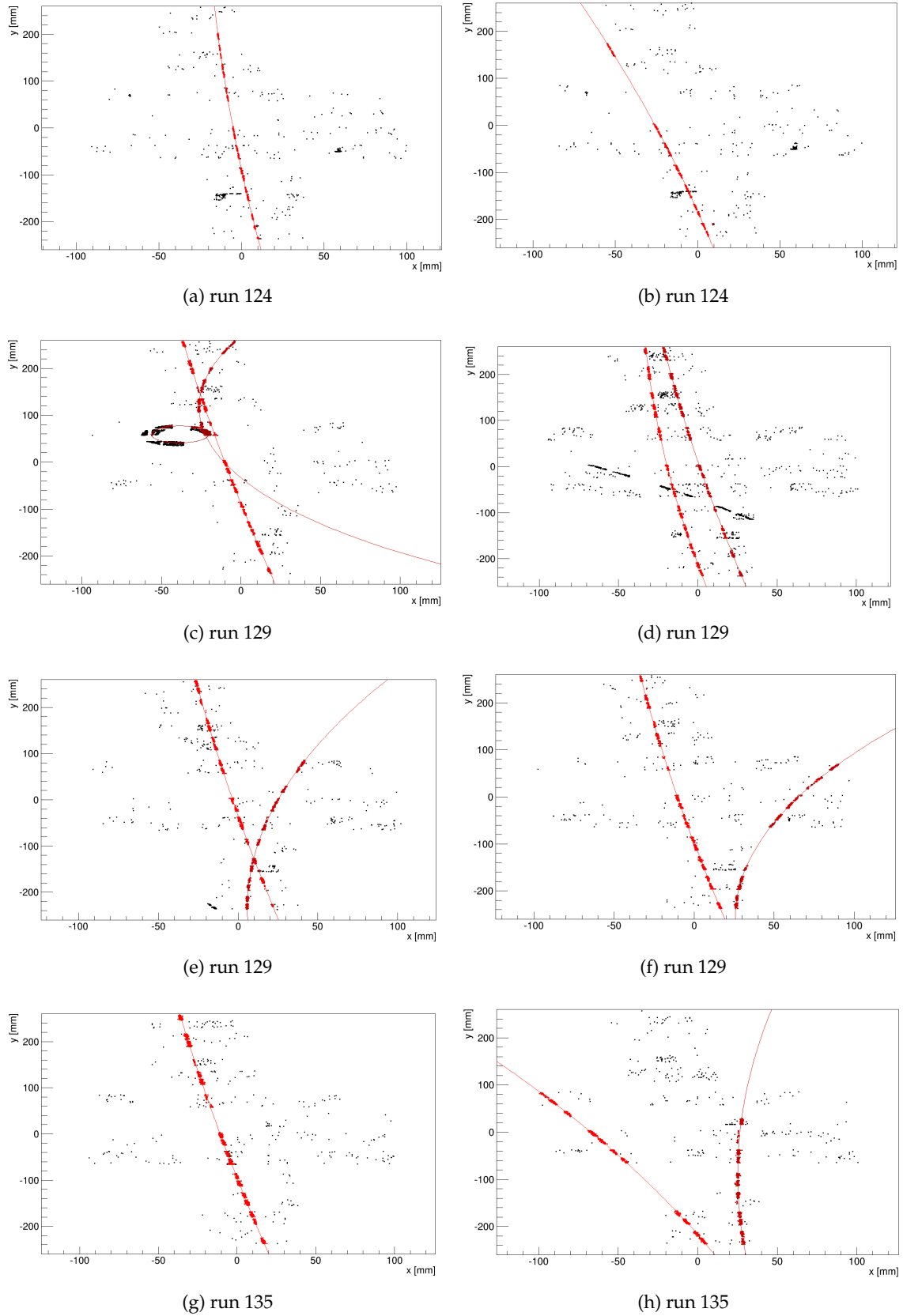


Figure C.3: Transverse and longitudinal spatial resolution: runs 124 with 44 ± 4 mm, 129 with 223 ± 5 mm and 135 with 482 ± 5 mm Z position for the first package dataset.

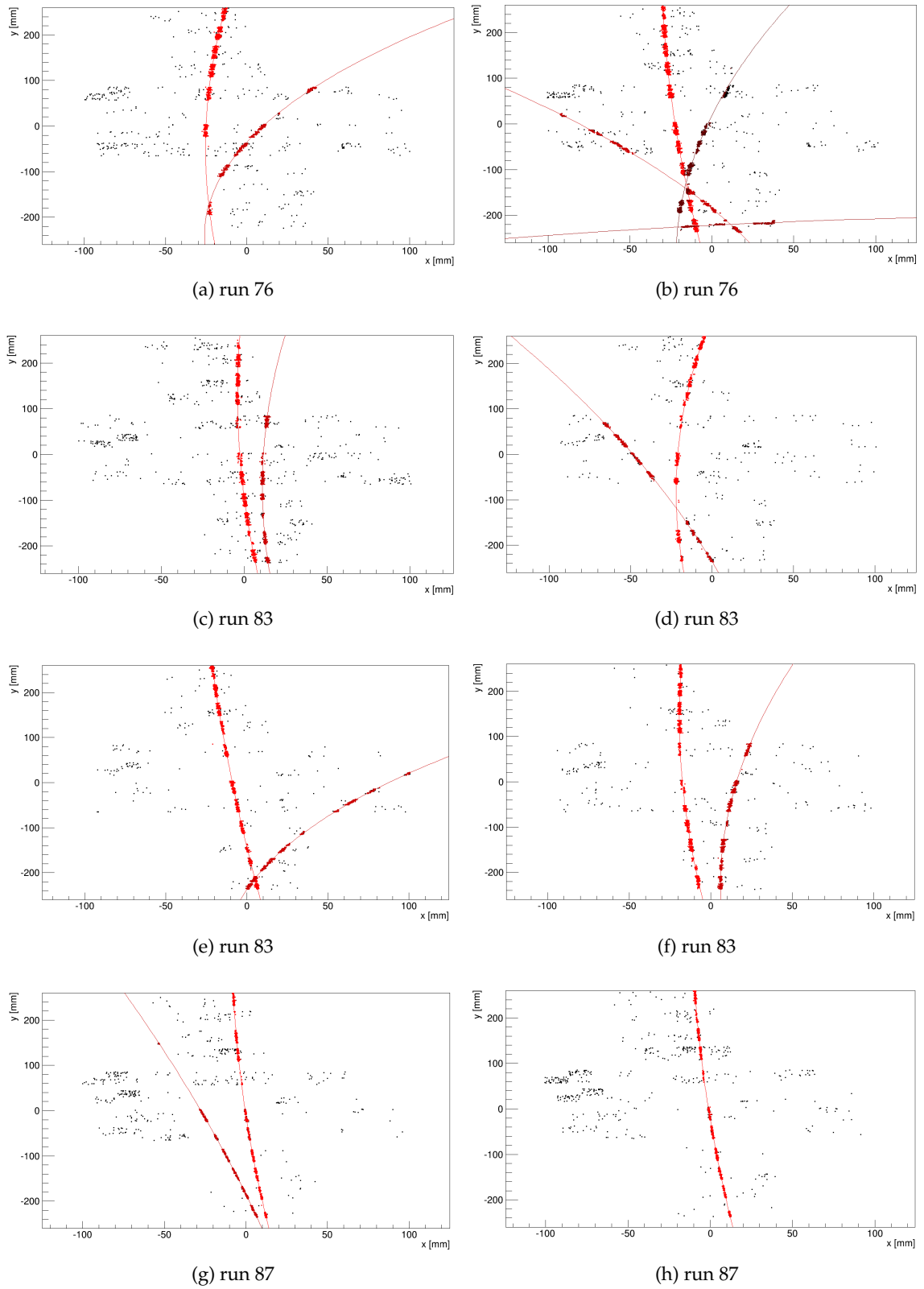


Figure C.4: Transverse and longitudinal spatial resolution: runs 76 with 482 ± 5 mm, 83 with 276 ± 4 mm and 87 with 72 ± 4 mm Z position for the second package dataset.

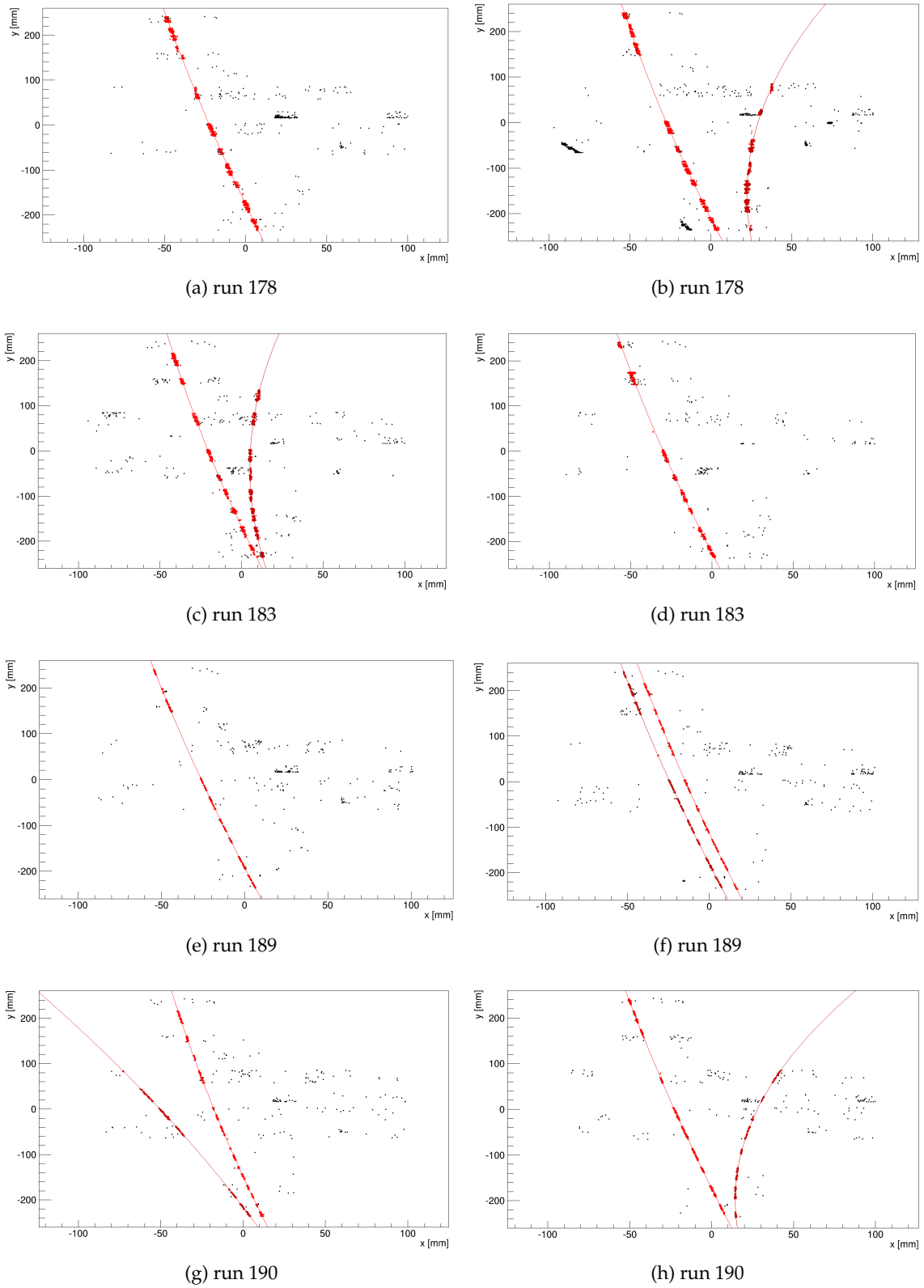


Figure C.5: Transverse and longitudinal spatial resolution: runs 178 with 485 ± 5 mm, 183 with 277 ± 5 mm, 189 with 18 ± 2 mm and 190 with 45 ± 4 mm Z position for the third package dataset.

Bibliography

- [1] David Griffiths. *Introduction to Elementary Particles*. Second edition. WILEY-VCH, Berlin, 2008.
- [2] Wikipedia. *Wikipedia, The Free Encyclopedia*. URL: https://en.wikipedia.org/wiki/File:Standard_Model_of_Elementary_Particles.svg.
- [3] G. Aad et al. "Observation of a new particle in the search for the Standard Model Higgs boson with the ATLAS detector at the LHC". In: *Physics Letters B* 716.1 (2012), pp. 1–29. DOI: [10.1016/j.physletb.2012.08.020](https://doi.org/10.1016/j.physletb.2012.08.020). URL: [arXiv:201207.7214](https://arxiv.org/abs/201207.7214) [hep-ex].
- [4] S. Chatrchyan et al. "Observation of a new boson at a mass of 125 GeV with the CMS experiment at the LHC". In: *Physics Letters B* 716.1 (2012), pp. 30–61. DOI: [10.1016/j.physletb.2012.08.021](https://doi.org/10.1016/j.physletb.2012.08.021). URL: [arXiv:201207.7235](https://arxiv.org/abs/201207.7235) [hep-ex].
- [5] P. A. R. Ade et al. "Planck 2015 results. XIII. Cosmological parameters". In: *Astronomy & Astrophysics, Worldwide astronomical and astrophysical research* 594.A13 (2016), p. 63. DOI: [10.1051/0004-6361/201525830](https://doi.org/10.1051/0004-6361/201525830). URL: [arXiv:201502.01589](https://arxiv.org/abs/201502.01589) [astro-ph.CO].
- [6] Ina Brock and Thomas Schörner-Sadenius, eds. *Physics at the Terascale*. Wiley-VCH, Berlin, 2011. URL: <http://www.wiley-vch.de/publish/dt/books/ISBN3-527-41001-5>.
- [7] S. Myers and E. Picasso. "The design, construction and comissioning of the CERN Large Electron-Positron collider". In: *Contemporary Physics* 31.6 (1990), pp. 387–403. DOI: [10.1080/00107519008213789](https://doi.org/10.1080/00107519008213789).
- [8] L. Evans and P. Bryant. "LHC Machine". In: *Journal of Instrumentation* 3 (2008). S08001. DOI: [10.1088/1748-0221/3/08/S08001](https://doi.org/10.1088/1748-0221/3/08/S08001).
- [9] N. Phinney et al. *International Linear Collider Reference Design Report Volume 3 - Accelerator*. 2007. URL: [arXiv:200712.2361](https://arxiv.org/abs/200712.2361).
- [10] Chris Adolphsen et al. *The International Linear Collider Technical Design Report - Volume 3 Part II: Accelerator Baseline Design*. CERN-ATS-2013-037, DESY 13-062, ILC-REPORT-2013-040, 2013.
- [11] T.Behnke et al. *The International Linear Collider Technical Design Report - Volume 1: Executive summary*. CERN-ATS-2013-037, DESY 13-062, ILC-REPORT-2013-040, 2013.
- [12] T. Behnke et al. *The International Linear Collider Technical Design Report - Volume 4: Detectors*. CERN-ATS-2013-037, DESY 13-062, ILC-REPORT-2013-040, 2013. URL: [arXiv:201306.6329](https://arxiv.org/abs/201306.6329) [physics.ins-det].
- [13] Isa Heinze. "Development of a Hough Transformation Track Finder for Time Projection Chambers". PhD thesis. der Universität Hamburg, 2013.
- [14] G. Weiglein et al. "Physics interplay of the LHC and the ILC". In: *Physics Reports* 426.2-6 (2006), pp. 47–358. DOI: [10.1016/j.physrep.2005.12.003](https://doi.org/10.1016/j.physrep.2005.12.003). URL: [arXiv:20hep-ph/0410364](https://arxiv.org/abs/20hep-ph/0410364) [hep-ph].

- [15] H. Baer et al. *The International Linear Collider Technical Design Report - Volume 2: Physics*. CERN-ATS-2013-037, DESY 13-062, ILC-REPORT-2013-040, 2013. URL: [arXiv:201306.6352](https://arxiv.org/abs/201306.6352) [hep-ph].
- [16] H. Li. "Higgs Recoil Mass and Higgs-Strahlung Cross-Section Study for the ILD LOI". In: *International Linear Collider Workshop 2010 (LCWS10 & ILC10)*. Beijing, China, March 26-30, 2010. URL: <https://inspirehep.net/record/861848/files/arXiv:1007.2999.pdf>.
- [17] Junping Tian and Keisuke Fuji. "Measurement of Higgs couplings and self-coupling at the ILC". In: *The European Physical Society Conference on High Energy Physics*. Stockholm, Sweden, 18-24 July, 2013. URL: [arXiv:201311.6528](https://arxiv.org/abs/201311.6528) [hep-ph].
- [18] F. Abe et al (CDF Collaboration). "Observation of Top Quark Production in $\bar{p}p$ Collisions with the Collider Detector at Fermilab". In: *Physical review letters* 74.14.2626 (1995). DOI: [10.1103/PhysRevLett.74.2626](https://doi.org/10.1103/PhysRevLett.74.2626). URL: [hep-ex/9503002].
- [19] S. Abachi et al (D0 Collaboration). "Observation of the Top Quark". In: *Physical review letters* 74.14.2632 (1995). DOI: [10.1103/PhysRevLett.74.2632](https://doi.org/10.1103/PhysRevLett.74.2632). URL: [hep-ex/9503003].
- [20] *Forschung mit Lepton Collidern (FLC) homepage*. Accessed: April 17, 2018. URL: www.desy.de/flc.
- [21] M.A. Thomson. "Particle flow calorimetry and the PandoraPFA algorithm". In: *Nuclear Instruments and Methods in Physics Research Section A: Accelerators, Spectrometers, Detectors and Associated Equipment* 611.1 (2009). issn: 0168-9002, pp. 25–40. DOI: [10.1016/j.nima.2009.09.009](https://doi.org/10.1016/j.nima.2009.09.009). URL: <http://www.sciencedirect.com/science/article/pii/S0168900209017264>.
- [22] D. Nygren. "The Time Projection Chamber: A New 4 pi Detector for Charged Particles". In: *eConf C740805 (1974)* 58. 1974.
- [23] Christoph Brezina. "A GEM based Time Projection Chamber with Pixel Readout". PhD thesis. Universität Bonn, 2013.
- [24] Claus Grupen. *Particle Detectors*. Cambridge University press, 1996.
- [25] B.Rossi. *High Energy Particles*. Prentice-Hall, 1952.
- [26] J. Beringer et al. PDG. PR D86, 010001. 2012. URL: <http://pdg.lbl.gov>.
- [27] H. Bichsel. "A method to improve tracking and particle identification in TPCs and silicon detectors". In: *Nuclear Instruments and Methods in Physics Research Section A: Accelerators, Spectrometers, Detectors and Associated Equipment* 562.1 (2006). issn: 0168-9002, pp. 154–197. DOI: [10.1016/j.nima.2006.03.009](https://doi.org/10.1016/j.nima.2006.03.009). URL: <http://www.sciencedirect.com/science/article/pii/S0168900206005353>.
- [28] W. Yu. "Particle identification of the ALICE TPC via dE/dx". In: *Nuclear Instruments and Methods in Physics Research Section A: Accelerators, Spectrometers, Detectors and Associated Equipment* 706 (2013). issn: 0168-9002, pp. 55–58. DOI: [10.1016/j.nima.2012.05.022](https://doi.org/10.1016/j.nima.2012.05.022). URL: <http://www.sciencedirect.com/science/article/pii/S0168900212005098>.
- [29] W. Blum and L. Rolandi. *Particle Detection with Drift Chambers*. Berlin: Springer, 1993.

- [30] A. Sharma. *Properties of some gas mixtures used in tracking detectors*. 1998. URL: <https://archana.web.cern.ch/archana/Publications/Tracking-det-gases.pdf>.
- [31] H. J. Hilke. "Time projection chambers". In: *Reports on Progress in Physics* 73.11 (2010). p. 116201. DOI: 10.1088/0034-4885/73/11/116201.
- [32] K. Ackermann et al. "A study with a small prototype TPC for the international linear collider experiment". In: *Nuclear Instruments and Methods in Physics Research Section A: Accelerators, Spectrometers, Detectors and Associated Equipment* 623.1 (2010), pp. 141–143. DOI: 10.1016/j.nima.2010.02.175. URL: [arXiv:200905.2655v2](https://arxiv.org/abs/200905.2655v2) [physics.ins-det].
- [33] F. Sauli. "GEM: A new concept for electron amplification in gas detectors". In: *Nuclear Instruments and Methods in Physics Research Section A: Accelerators, Spectrometers, Detectors and Associated Equipment* 386.2–3 (1997). issn: 0168-9002, pp. 531–534. DOI: 10.1016/S0168-9002(96)01172-2. URL: <http://www.sciencedirect.com/science/article/pii/S0168900296011722>.
- [34] Y. Giomataris et al. "MICROMEGAS: a high-granularity position-sensitive gaseous detector for high particle-flux environments". In: *Nuclear Instruments and Methods in Physics Research Section A: Accelerators, Spectrometers, Detectors and Associated Equipment* 376.1 (1996), pp. 29–35. DOI: 10.1016/0168-9002(96)00175-1. URL: <http://www.sciencedirect.com/science/article/pii/0168900296001751>.
- [35] S. Blatt et al. "Charge transfer of GEM structures in high magnetic fields". In: *Nucl. Phys. Proc. Suppl.* 150 (2006), pp. 155–158. DOI: 10.1016/j.nuclphysbps.2004.07.005.
- [36] Webpage of the CERN GDD group. URL: <http://gdd.web.cern.ch/GDD/>.
- [37] J. Alcaraz. "Helicoidal Tracks". In: *L3 Internal Note 1666* (1995). URL: http://www.lcsim.org/sites/lcsim/lcsim-tracking/apidocs/org/lcsim/util/swim/doc-files/L3_helix.pdf.
- [38] John Hauptman. *Particle Physics Experiments at High Energy Colliders*. Wiley, 2010.
- [39] C. Grupen and I. Buvat. *Handbook of Particle Detection and Imaging*. Vol. 2. Springer, 2012.
- [40] R. Gluckstern. "Uncertainties in track momentum and direction, due to multiple scattering and measurement errors". In: *Nuclear Instruments and Methods* 24, issn: 0029-554X (1963).
- [41] *ILCSoft Homepage*. Accessed: April 17, 2018. URL: <http://ilcsoft.desy.de/>.
- [42] F. Gaede et al. "LCIO-A persistency framework for linear collider simulation studies". In: *LC Note LC-TOOL-2003-053* (2003). URL: [arXiv:physics/0306114v1](https://arxiv.org/abs/physics/0306114v1).
- [43] *LCIO Homepage*. Accessed: April 17, 2018. URL: <http://lcio.desy.de>.
- [44] Thomas Krämer. "Track parameters in LCIO". In: *LC-DET-2006-004* (2006).
- [45] *GEAR Homepage*. Accessed: April 17, 2018. URL: http://ilcsoft.desy.de/portal/software_packages/gear/.
- [46] *Marlin Homepage*. Accessed: April 17, 2018. URL: http://ilcsoft.desy.de/portal/software_packages/marlin.

- [47] F. Gaede. “Marlin and LCCD: Software tools for the ILC”. In: *Nucl.Instrum.Meth. A559* (2006), pp. 177–180. DOI: [10.1016/j.nima.2005.11.138](https://doi.org/10.1016/j.nima.2005.11.138).
- [48] J. Abernathy et al. “MarlinTPC: A Marlin based common TPC software framework for the LCTPC collaboration”. In: *LC Note LC-TOOL-2007-001* (2007).
- [49] *MarlinTPC Homepage*. Accessed: April 17, 2018. URL: http://ilcsoft.desy.de/portal/software_packages/marlintpc/.
- [50] X. Llopart. *Timepix manual v1.0*. 2006.
- [51] X. Llopart et al. “Timepix, a 65k programmable pixel readout chip for arrival time, energy and/or photon counting measurements”. In: *Nuclear Instruments and Methods in Physics Research Section A: Accelerators, Spectrometers, Detectors and Associated Equipment 581.1* (2007), pp. 485–494. DOI: [10.1016/j.nima.2007.08.079](https://doi.org/10.1016/j.nima.2007.08.079).
- [52] M. Campbell et al. “The detection of single electrons by means of a Micromegas-covered Medipix2 pixel CMOS readout circuit”. In: *Nuclear Instruments and Methods in Physics Research, Section A: Accelerators, Spectrometers, Detectors and Associated Equipment 540.2-3* (2005), pp. 295–304. DOI: [10.1016/j.nima.2004.11.036](https://doi.org/10.1016/j.nima.2004.11.036).
- [53] R. Ulman. “Calibration of the Timepix pixel chip for the readout of gaseous particle detectors”. MA thesis. Mathematisch-Naturwissenschaftlichen Fakultät der Rheinischen-Friedrich-Wilhelms-Universität Bonn, 2011. URL: http://pi.physik.uni-bonn.de/pi_plone/lhcilc/documents/t00000012.pdf?c=t&id=12.
- [54] M. Lupberger. “Avalanche statistics and single electron counting with a Timepix-InGrid detector”. MA thesis. Freiburg Germany: Albert-Ludwigs Universität Freiburg, 2010. URL: http://terascale.physik.unifreiburg.de/Publikationen/abschlussarbeiten/diplommasterarbeiten/diplomarbeit_lupberger.pdf.
- [55] V. M. Blanco Carballo. “Radiation imaging detectors made by wafer post-processing of CMOS chips”. PhD thesis. University of Twente, 2009. DOI: [10.3990/1.9789036528559](https://doi.org/10.3990/1.9789036528559).
- [56] Michael Lupberger. “The Pixel-TPC: A feasibility study”. PhD thesis. Universität Bonn, 2015.
- [57] R. Frühwirth and A. Strandlie. “Pattern recognition and estimation methods for track and vertex reconstruction”. In: *Proceedings of the 13th International Workshop on Advanced Computing and Analysis Techniques in Physics Research, ACAT2010, PoS(ACAT2010)003*. (2010).
- [58] R. Frühwirth et al. *Data Analysis Techniques for High-Energy Physics*. second edition. United Kingdom: Cambridge: Cambridge University Press, 2000.
- [59] C.M. Bishop. *Pattern Recognition and Machine Learning*. New York, USA, Springer, 2006.
- [60] Sebastian Raschka. *Python Machine Learning*. Birmingham, UK: Packt Publishing, 2015.
- [61] K. Fujii (ACFA Sim-J Group). *Extended Kalman Filter*. June 2013. URL: <http://www-jlc.kek.jp/subg/offl/kaltest/>.

- [62] R. Frühwirth. "Application of Kalman filtering to track and vertex fitting". In: *Nuclear Instruments and Methods in Physics Research Section A: Accelerators, Spectrometers, Detectors and Associated Equipment* 262.2-3 (1987). North-Holland, Amsterdam, pp. 444–450. DOI: [10.1016/0168-9002\(87\)90887-4](https://doi.org/10.1016/0168-9002(87)90887-4).
- [63] P. V. C. Hough. "Machine Analysis of Bubble Chamber Pictures". In: *the International Conference on High Energy Acceleration and Instrumentation*. CERN. Geneva, 1959, pp. 554–556.
- [64] Claus Kleinwort. "General Broken Lines as advanced track fitting method". In: *Nuclear Instruments and Methods in Physics Research Section A: Accelerators, Spectrometers, Detectors and Associated Equipment* 673 (2012), pp. 107–110. DOI: [10.1016/j.nima.2012.01.024](https://doi.org/10.1016/j.nima.2012.01.024).
- [65] C. Kleinwort and Ch. Rosemann. "Definition for the usage of the General Broken Lines for a TPC". In: *LC-TOOL-2014-002, DESY* (2014).
- [66] R. Mankel. "Pattern Recognition and Event Reconstruction in Particle Physics Experiments". In: *Reports on Progress in Physics* 67.4 (2004). DOI: [10.1088/0034-4885/67/4/R03](https://doi.org/10.1088/0034-4885/67/4/R03). URL: [arXiv:physics/0402039v1](https://arxiv.org/abs/physics/0402039v1).
- [67] Claus Kleinwort. *Private communication*.
- [68] Claus Kleinwort. "Track fitting and alignment for a TPC with General Broken Lines". In: *LC-TOOL-2014-008, DESY* (2014).
- [69] V. Karimäki. "Effective circle fitting for particle trajectories". In: *Nuclear Instruments and Methods in Physics Research Section A: Accelerators, Spectrometers, Detectors and Associated Equipment* 305.1 (1991), pp. 187–191. DOI: [10.1016/0168-9002\(91\)90533-V](https://doi.org/10.1016/0168-9002(91)90533-V).
- [70] Richard O.Duda and Peter E.Hart. "Use of the Hough Transformation To Detect Lines and Curves in Pictures". In: *ACM Digital Library* 15.1 (1972), pp. 11–15. DOI: [10.1145/361237.361242](https://doi.org/10.1145/361237.361242).
- [71] Leandro A.F.Fernandes and Manuel M.Oliveira. "Real-time line detection through an improved Hough transform voting scheme". In: *Pattern Recognition* 41.1 (2008), pp. 299–314. DOI: [10.1016/j.patcog.2007.04.003](https://doi.org/10.1016/j.patcog.2007.04.003).
- [72] Glen Cowan. *Statistical Data Analysis*. New York: Oxford University Press Inc., 1998.
- [73] Rene Brun and Fons Rademakers. "Root-an object oriented data analysis framework". In: *Nuclear Instruments and Methods in Physics Research Section A: Accelerators, Spectrometers, Detectors and Associated Equipment* 389.1-2 (1997), pp. 81–86. DOI: [10.1016/S0168-9002\(97\)00048-X](https://doi.org/10.1016/S0168-9002(97)00048-X).
- [74] *Alias for bivariate normal distribution*. Accessed: April 17, 2018. URL: <https://sft.its.cern.ch/jira/browse/ROOT-8022>.
- [75] Kai Oliver Arras. "An Introduction To Error Propagation: Derivation, Meaning and Examples of Equation $C_Y = F_X C_X F_X^T$ ". In: *Technical Report No EPFL-ASL-TR-98-01 R3 of the Autonomous Systems Lab, Institute of Robotic Systems, Swiss Federal Institute of Technology Lausanne (EPFL)* (1998). DOI: [10.3929/ethz-a-010113668](https://doi.org/10.3929/ethz-a-010113668).
- [76] Mark C.Hendricks. *Rotated ellipses and their intersections with lines*. Mar. 2012. URL: <http://quickcalcbasic.com/ellipse%20line%20intersection.pdf>.
- [77] Norman Richard Draper and Harry Smith. *Applied Regression Analysis*. Canada: Wiley and Sons, Inc, 1981.

- [78] A. Münnich. "Simulation Studies for a High Resolution Time Projection Chamber at the International Linear Collider". PhD thesis. RWTH Aachen, 2007.
- [79] I. B. Smirnov. "Modeling of ionization produced by fast charged particles in gases". In: *Nuclear Instruments and Methods in Physics Research Section A: Accelerators, Spectrometers, Detectors and Associated Equipment* A554.1-3 (2005), pp. 474–493. DOI: [10.1016/j.nima.2005.08.064](https://doi.org/10.1016/j.nima.2005.08.064).
- [80] M. Killenberg. "Software and Parameters for Detailed TPC Studies in the CLIC CDR". In: *CERN. Switzerland. LCD-Note-2011-025* (2012).
- [81] P. Schade and J. Kaminski. "A large TPC prototype for a linear collider detector". In: *Nuclear Instruments and Methods in Physics Research Section A: Accelerators, Spectrometers, Detectors and Associated Equipment* 628.1 (2011). issn: 0168-9002, pp. 128–132. DOI: [10.1016/j.nima.2010.06.300](https://doi.org/10.1016/j.nima.2010.06.300). URL: <http://www.sciencedirect.com/science/article/pii/S0168900210014907>.
- [82] E. G. Ties Behnke et al. "Test Beams at DESY". In: *EUDET-Memo-2007-011* (2007). URL: <http://www.eudet.org/e26/e28/e182/e283/eudet-memo-2007-11.pdf>.
- [83] S. Biagi. *MAGBOLTZ, program to compute gas transport parameters*. VERSION 11.2. 2016. URL: <http://magboltz.web.cern.ch/magboltz/>.
- [84] Martin Rogowski. "Implementation of a track finding algorithm for an InGrid based detector". MA thesis. Bonn: University of Bonn, 2014.
- [85] R. Diener. *PCMAG/LPTPC status*. 2015. URL: <https://agenda.linearcollider.org/event/6815/contribution/1/material/slides/0.pdf>.
- [86] Felix Müller. "Development of a Triple GEM Readout Module for a Time Projection Chamber & Measurement Accuracies of Hadronic Higgs Branching Fractions in $\nu\nu H$ at a 350 GeV ILC". PhD thesis. Hamburg: Universität Hamburg, 2016.
- [87] Jia-Hua Cheng et al. "Determination of the total absorption peak in an electromagnetic calorimeter". In: *Nuclear Instruments and Methods in Physics Research Section A: Accelerators, Spectrometers, Detectors and Associated Equipment* 827 (2016), pp. 165–170. DOI: [10.1016/j.nima.2016.05.010](https://doi.org/10.1016/j.nima.2016.05.010). URL: [arXiv:1603.04433](https://arxiv.org/abs/1603.04433).
- [88] Jochen Kaminski. *Private communication*.
- [89] R. K. Carnegie et al. "Resolution studies of cosmic-ray tracks in a TPC with GEM readout". In: *Nuclear Instruments and Methods in Physics Research A* 538 (2005), pp. 372–383. DOI: [10.1016/j.nima.2004.08.132](https://doi.org/10.1016/j.nima.2004.08.132). URL: [physics/0402054](https://arxiv.org/abs/physics/0402054).
- [90] R. Yonamine et al. "Spatial resolutions of GEM TPC. A novel theoretical formula and its comparison to latest beam test data". In: *Journal of Instrumentation* 9.3 (2014). C03002. URL: <http://stacks.iop.org/1748-0221/9/i=03/a=C03002>.